STARS

University of Central Florida
STARS

Electronic Theses and Dissertations, 2004-2019

2005

Design And Assessment Of Compact Optical Systems Towards Special Effects Imaging

Vesselin Chaoulov
University of Central Florida

Part of the Electromagnetics and Photonics Commons, and the Optics Commons
Find similar works at: https://stars.library.ucf.edu/etd
University of Central Florida Libraries http://library.ucf.edu

This Doctoral Dissertation (Open Access) is brought to you for free and open access by STARS. It has been accepted for inclusion in Electronic Theses and Dissertations, 2004-2019 by an authorized administrator of STARS. For more information, please contact STARS@ucf.edu.

STARS Citation
Chaoulov, Vesselin, "Design And Assessment Of Compact Optical Systems Towards Special Effects Imaging" (2005). *Electronic Theses and Dissertations, 2004-2019*. 295.
https://stars.library.ucf.edu/etd/295

DESIGN AND ASSESSMENT OF COMPACT OPTICAL SYSTEMS TOWARDS SPECIAL EFFECTS IMAGING

by

VESSELIN IOSSIFOV SHAOULOV
B.S. Sofia University, 1994
M.S. Sofia University, 1996
M.S. University of Central Florida, 2003

A dissertation submitted in partial fulfillment of the requirements
for the degree of Doctor of Philosophy
in the College of Optics and Photonics
at the University of Central Florida
Orlando, Florida

Spring Term
2005

Major Professor: Jannick P. Rolland

© 2004 Vesselin I. Shaoulov

ABSTRACT

A main challenge in the field of special effects is to create special effects in real time in a way that the user can preview the effect before taking the actual picture or movie sequence. There are many techniques currently used to create computer-simulated special effects, however current techniques in computer graphics do not provide the option for the creation of real-time texture synthesis. Thus, while computer graphics is a powerful tool in the field of special effects, it is neither portable nor does it provide work in real-time capabilities. Real-time special effects may, however, be created optically. Such approach will provide not only real-time image processing at the speed of light but also a preview option allowing the user or the artist to preview the effect on various parts of the object in order to optimize the outcome.

The work presented in this dissertation was inspired by the idea of optically created special effects, such as painterly effects, encoded in images captured by photographic or motion picture cameras. As part of the presented work, compact relay optics was assessed, developed, and a working prototype was built. It was concluded that even though compact relay optics can be achieved, further push for compactness and cost-effectiveness was impossible in the paradigm of bulk macro-optics systems. Thus, a paradigm for imaging with multi-aperture micro-optics was proposed and demonstrated for the first time, which constitutes one of the key contributions of this work. This new paradigm was further extended to the most general case of magnifying multi-aperture micro-optical systems. Such

paradigm allows an extreme reduction in size of the imaging optics by a factor of about 10 and a reduction in weight by a factor of about 500.

Furthermore, an experimental quantification of the feasibility of optically created special effects was completed, and consequently raytracing software was developed, which was later commercialized by SmARTLens^{TM}. While the art forms created via raytracing were powerful, they did not predict all effects acquired experimentally. Thus, finally, as key contribution of this work, the principles of scalar diffraction theory were applied to optical imaging of extended objects under quasi-monochromatic incoherent illumination in order to provide a path to more accurately model the proposed optical imaging process for special effects obtained in the hardware. The existing theoretical framework was generalized to non-paraxial in- and out-of-focus imaging and results were obtained to verify the generalized framework. In the generalized non-paraxial framework, even the most complex linear systems, without any assumptions for shift invariance, can be modeled and analyzed.

To my mother, who was always my greatest supporter.

To the memory of my father, who taught me that even the longest journey must begin with a single step. For everything he taught me, I will always remain grateful.

To the memory of all my grandparents and my aunt, who taught me to reach for my dreams.

ACKNOWLEDGEMENTS

First and foremost, I want to thank my advisor, Jannick Rolland, for working so hard guiding me through my research, setting the highest standards, and helping me become a better scientist.

I want to express my gratitude to my committee members, James Harvey, S.T. Wu and Guy Schiavone for their generous assistance, comments, suggestions, and great input in developing this work.

I would like to thank Glenn Boreman from the College of Optics/CREOL for his continuing mentoring, support, and encouragement during the years of my graduate program.

I would like to express my gratitude to Dencho Ivanov from New Jersey Institute of Technology for first turning me to science and encouraging me to pursue it further.

To my faculty mentors in Bulgaria, Liyudmil Vatskitchev, Liliyana Ivanova from the Sofia University “St. Kliment Ohridsky” and Sashka Alexandrova from the Bulgarian Academy of Sciences, I want to thank for inspiring me to begin my path as a scientist and guiding me throughout my first steps.

I cannot fully express my gratitude to my family for everything they taught me and all their support over the years and most of all, for helping me become a better person.

To my closest friends in Bulgaria, the United States and elsewhere, I want to thank all of you for your continuing support in all my endeavors and sometimes much needed advice. You all are wonderful and I hope our friendship will last forever.

For their generous assistance in this research, I would like to acknowledge the following people and organizations.

I would like to thank BRO Corporation for the educational license of ASAP™ to the College of Optics and Photonics/CREOL&FPCE, as well as Mari Cote, Carey Portnoy and Steve Miller for their assistance during the process of optimization of the ASAP™ codes used in the quantification of the multi-aperture micro-optical systems presented in Chapter 3. Furthermore, I would like to thank Optical Research Associates for the educational license of CodeV, which helped us conceive the bulk relay optics, as well as Kevin Thompson and Bill Cassarly for suggesting investigating microlenslet arrays as a potential solution for relay imaging and for providing stimulating discussions about noise associated with raytracing, respectively. Finally, I would like to thank Catherine Meyer for creating unique Photoshop textures we then transformed into optical phase plates and art form pictures. The earlier part of this research on raytracing and the experimental work on microlenslet imaging to gain insight into feasibility was supported by the State of Florida I4-corridor initiative and SmARTlens™ Corporation. Other components of the research were supported by the US Army Simulation, Training, and Instrumentation Command (STRICOM). I would like to

especially thank my friend Ricardo Martins for the stimulating discussions and his innovative ideas related to imaging with micro-optics.

I would like to thank Steve Hylen for his brilliant vision and talents with photography and for his stimulating discussions and assistance with the experimental part of the research, presented in Chapter 4. Also, I would like to thank Joe Burkenburg from the former Rochester Photonics Corporation (RPC) for his assistance and support with the optical phase plates fabrication during the project, which was a stretch from their main line of work. Their trust and support are truly valuable to me. I would like to thank my friend Nikolay Shishkov for his assistance with the C++ coding of the ASAP plug-in demonstrated in Chapter 4. Finally, I would like to thank Mari Cote and Michael Stevenson from the Breault Research Organization (BRO) for their help with the ASAP code for imaging and the modelling of the optical phase plate in Rhinoceros, respectively, and Steve Sagan from the ORA for his assistance with the design of the bulk optics compact relay lens.

Finally, I would like to thank Demetrios Christodoulides, Boris Zeldovich from the College of Optics and Photonics/CREOL&FPCE, Eric Clarkson for his guidance on some subtle aspects of the mathematics associated with statistical optics, Ravi Satya for his invaluable hours of programming of the Beowulf Cluster together with his bright mind, and my friend Dr. Polyakov from the California Institute of Technology/Caltech for stimulating discussions about research reported in Chapter 5.

TABLE OF CONTENTS

ABSTRACT ..... **iv**

ACKNOWLEDGEMENTS ..... **vii**

TABLE OF CONTENTS ..... **x**

LIST OF TABLES ..... **xii**

LIST OF FIGURES ..... **xiiiii**

CHAPTER 1: INTRODUCTION **1**

1.1 Computer-Simulated Special Effects 1

1.2 Optics and Art 3

1.3 Modelling of the Imaging Process 6

1.4 Motivation 8

1.5 Research Summary 9

1.6 Dissertation Outline 9

CHAPTER 2: RELATED WORK **11**

2.1 Relay Lenses 11

2.2 Relay Lenses for Special Effects 12

2.3 Modelling of the Imaging Process 13

CHAPTER 3: DESIGN AND ASSESSMENT OF COMPACT RELAY LENSES **15**

3.1 Conceptual Design of an Imaging System for Optically Created Special Effects 15

3.2 Design of Compact Macro-Optics Relay Lenses 17

3.3 Imaging with Microlenslet Arrays 22

3.3.1 Paraxial Layout of 1:1 Imaging with a Pair of Microlenses 23

3.3.2 Optical Layout of 1:1 Imaging with a Stack of Two Microlenslet Arrays 25

3.3.3 Modeling the Imaging Properties of the System with Simple Light Sources 29

3.3.3.1 Establishing a minimum number of rays 31

3.3.3.2 Quantification of Lensletization 35

3.3.4 Modelling of the Imaging Properties of the System for Greyscale Images 38

3.3.5 Systems compactness 41

3.3.6 Paraxial Layout of 1:M Imaging with a Stack of Two Dissimilar Microlenslet Arrays. 42

3.3.7 Modelling the Imaging Properties of the Generalized Magnifying System with Greyscale Light Sources 48

3.4 Discussion and Future Work 52

CHAPTER 4: EXPERIMENTAL METHODS AND RAYTRACING AS AN IMAGING PROCESS.....55

4.1 Experimental Assessment of Optically Creating Special Effects 55

4.1.1 Experimental Setup.....55

4.1.2 Relay Lens Prototype.....60

4.1.3 Fabrication of the Optical Phase Plates.....68

4.2 Software Modelling of the Imaging Process within the Raytracing Paradigm 72

4.2.1 Raytracing in the Theoretical Framework of the Vectorial Law of Refraction 72

4.2.2. Modelling of the Imaging Process by Utilizing a Custom Developed Raytracing Software 74

4.2.3. Exploration of Raytracing through Texture Phase Plates using Commercially Available Software 78

4.3. Discussion and Future Work.....82

CHAPTER 5: PHYSICAL OPTICS MODELLING OF THE IMAGING PROCESS THROUGH OPTICAL PHASE PLATES 83

5.1 Introduction 83

5.2 Review of the Theoretical Framework for Quasi-Monochromatic Incoherent Illumination 87

5.3 Application of the Paraxial Framework to Plane-to-Plane and Plane-to-Curve Imaging Configurations..91

5.4 Generalized Non-Paraxial Theoretical Framework Based on the Rayleigh-Sommerfeld Scalar Diffraction Theory.....94

5.5 Results 100

5.6 Discussion and future work 108

CHAPTER 6: CONCLUSIONS AND FUTURE WORK 109

6.1 Summary of Contribution 109

6.2 Future Work.....111

LIST OF REFERENCES.....113

LIST OF TABLES

Table 3.1 Optical specification of a relay lens: Design of a Relay Lens to Interface a 50mm Nikon Objective 18

Table 3.2 Peak-to-valley error in the difference between the normalized autocorrelation of the object and the resulting image. 36

Table 3.3 Overall compactness of the microlenslet arrays. 42

Table 4.1. Measurements of three Nikon photographic lenses 62

Table 4.2. Measurements of field curvature for standard 50mm Nikon objective. 64

Table 4.3. Specification for the design of a compact relay lens to create optical special effects by utilizing optical phase plates. 66

LIST OF FIGURES

Figure 3.1 Optical layout of an imaging system, where an optical phase plate is inserted close to the final image location. 15

Figure 3.2 Optical layout of an imaging system, where an optical phase plate is inserted in an intermediate image plane where it is modified and is further relayed to the final image plane. 16

Figure 3.3 Optical layout of a compact relay 1:1 system. 19

Figure 3.4 Optical design assessment (a) ray fan plots; (b) Modulation transfer functions. . 21

Figure 3.5 Paraxial layouts of 1:1 imaging with a single pair of microlenses. 24

Figure 3.6 Ray sketching illustrating the presence of ghost images for a stack of two microlenslet arrays without any baffles. 25

Figure 3.7 Microlenslet arrays 1:1 imaging 2f-sytem with appropriate baffle to minimize ghost images. 27

Figure 3.8 Illustration of the irradiance profiles of an extended object imaged through (a) a 2f-system microlenslet arrays relay lens; (b) A 5f-system. 29

Figure 3.9 ASAP^{TM} layout of the 2f-system microlenslet array based relay system with two 11 by 11 arrays of microlenses and the appropriate baffle. The object to be imaged is not represented in the figure, however from right to left, the baffle, the two microlenslet arrays made of plano-convex square lenses, and the detector upon which an image will be formed given an object in front of the baffle, are shown. 30

Figure 3.10 SNR for the 5f-system as a function of the number of rays emitted from the object, using Eq. (3.7). In this plot N equal 8281 pixels, and η equal 34%. 32

Figure 3.11 Imaging and irradiance distribution of an ellipse: (a) original image (b) image through the 2f-system (c) image through the 3f- system (d) image through the 4f-system (e) image through the 5f-system (f) image through 6f-system (g) image through the 7f-system. For the irradiance distributions the grey level value vs. the number of pixels in the object is plotted. The autocorrelation functions of the image are plotted in arbitrary units. 37

Figure 3.12 Imaging and irradiance distribution of a grayscale bitmap object: (a) original image; (b) image through "2f" system; (c) image through "3f" system; (d) image through "4f" system; (e) image through "5f" system; (f) image through "6f" system; and (g) image through "7f" system. 40

Figure 3.13 Simulation of imaging of an RGB image through a stack of two microlenslet arrays to qualitatively assess the impact of chromatic aberrations on image formation. 40

Figure 3.14 Normalized PSF plots for 0%, 70%, 95% and 100% vignetted sub-fields of view for a pair of plano-convex lenses. 41

Figure 3.15 Paraxial optical layout of a generalized magnifying system with an overall magnification of $M > 1$. 43

Figure 3.16 Optical layouts of 1:M imaging with a stack of two arrays of microlenses. 43

Figure 3.17 ASAP™ layout of 1:2 microlenslet arrays based magnifying system with two 11 by 11 arrays of microlenses and the appropriate baffle. From right to left, the baffle, the two dissimilar microlenslet arrays made of square plano-convex lenses, and the detector upon which an image will be formed given an object in front of the baffle, are shown. 49

Figure 3.18 Accuracy of the raytrace in percents as a function of the number of rays emitted from the object. 50

Figure 3.19 Imaging of grayscale object through 1:2 microlenslet array based magnifying system: (a) object and (b) magnified image. 51

Figure 4.1 Layout of the bench optical system used to assess imaging through optical phase plates. 56

Figure 4.2 Bench optical setup in the testing of imaging though optical phase plates. 57

Figure 4.3 Images obtained on the bench setup with: (a) 5mm defocus of the optical phase plate with respect to the intermediate image plane; (b) same as in (a) with some additional defocus introduced by the front objective; (c) closeup view of the scene with the same amount of defocus as in (b); (d) another closeup view of the scene with the same amount of defocus as in (b)..... 59

Figure 4.4 Nodal slide method used to measure the BFL of the lens under test. (Courtesy of J. Harvey and A. Krywonos)..... 62

Figure 4.5 Measurement of the field curvature of a standard Nikon 50mm Nikon lens and a quadratic fit of the data, representing the field curvature. 65

Figure 4.6 Compact relay lens prototype. 67

Figure 4.7 Images of special effects obtained with the prototype relay lens shown in Fig. 4.6 and proprietary phase plates. (Courtesy of Steve Hylen)..... 68

Figure 4.8 Dry laser etching instrument utilized in the fabrication of optical phase plates. .. 70

Figure 4.9 Four optical phase plates fabricated through the dry laser etching process. 70

Figure 4.10 Interferometric measurements of the optical phase plates. 71

Figure 4.11 Reflection and refraction of light at the surface between two media. 73

Figure 4.12 Simulation of optically created special effects using raytracing combined with an optical phase plate-based filter operation. 78

Figure 4.13 Optical texture plate created as a surface using a custom developed software module..... 80

Figure 4.14 Optical phase plate modeled in ASAP. 81

Figure 4.15 Result from the full raytrace in ASAP ™ using an optical phase plate covering the upper left ¼ of the object (right) and the original picture (left). 81

Figure 5.1 General relationships describing a LSI optical system..... 85

Figure 5.2 Layout of an optical system consisting of an object illuminated with a spatially incoherent quasi-monochromatic light field of complex amplitude U_0, an aberration-free optics, and an arbitrary imaging plane. 88

Figure 5.3 Illustration of stigmatic imaging on a curve surface for an object located at optical infinity. 93

Figure 5.4 Calculation of the optical path difference in the most general case of a converging optical system..... 98

Figure 5.5 Generalized non-paraxial imaging framework with the transformation plane normal to the chief ray and tilted with respect to the paraxial transformation plane.... 100

Figure 5.6 Results of imaging a 40 degree FOV object in a 2f imaging configuration for plane-to-curve imaging: (a) paraxial/quasi-paraxial model given by Eq.(2), (b) Non-paraxial model given by Eq.(5) for in-focus imaging (c) same as (b) but with 3mm out-of -focus imaging. 104

Figure 5.7 Demonstration of the existence of low light levels at the edge of the FOV in the case of the paraxial model in the case of plane-to-curve imaging: (a) Object with one white square at the edge of the FOV (b) Image. 105

Figure 5.8 Demonstration of the existence of low light levels at the edge of the FOV in the case of the paraxial model and for plane-to-curve imaging: (a) Object with one white square in the middle, and one white square at the edge. (b) Image of (a) using the paraxial model; the square at the edge is extremely dim with respect to that in the center and thus cannot be seen within a limited 255 greylevels display (c) Image of (a) using the non-paraxial model. Such imaging scenario models accurately imaging with a 40 degree FOV. 106

Figure 5.9 Results of the non-paraxial theoretical framework for plane-to-curve imaging: (a) using no approximation for the optics transformation, except assuming an aberration-free optics. (b) using nevertheless the parabolic optics transformation approximation, which could be thought to be responsible for having the model provided by Eq.(5.25) fail. Results reveal that the parabolic approximation for the optics transformation leads to negligible effects on overall imaging even for non-paraxial imaging, thus such approximation could be employed even in some non-paraxial case (i.e. moderate F-number) if it was to reduce the complexity of the computations. 107

CHAPTER 1: INTRODUCTION

In the introductory part of this work, computer-simulated special effects will be first discussed with an emphasis on their application in the movie making and art, followed by discussion on how the field of Optics relates to Art. Furthermore, various approaches to the modeling of the imaging process will be outlined. We shall then motivate this research and present a summary and outline of the dissertation.

1.1 Computer-Simulated Special Effects

Computer simulated special effects are virtually everywhere in modern-day life, starting from the moviemaking and going through areas such as art, science, music, business and internet. One can find computer-simulated special effects in movies like “Star Wars”, “The Mummy” and “The Matrix”, and at the same time on popular web sites offering virtual 3-D tours before purchasing a new house or car, or in a computer-based training program for medical doctors. The field of computer-simulated special effects grew exponentially over the last few years due to the availability and cost-effectiveness of powerful new computers and software on the current market. For example, ten years ago a typical state-of-the art computer system would have been a Silicon Graphics running IRIX that would have cost of the order of $200,000. Nowadays a typical PC station running state-of-the-art software would cost less than $3,000.

In this research, we shall focus on computer-simulated special effects for the creation of painterly effects on images. One of the early steps towards creation of computer-based painterly effects was line drawing on grey-scale raster by using brush extrusion [Whitted, 1983]. In parallel, the problem of texture synthesis was investigated in various works [Lewis, 1984], [Gardner, 1984], [Gagalowicz and Ma, 1986], [Miyata, 1990], [Wijk, 1991].

The problem of appropriate texture synthesis turns out to be central to the area of the computer-based special effects. One cannot create realistic special effects using computers without using textures that approach the reality. That is why most of the work in the field of computer-simulated special effects is focused on identifying and generating textures based on real world entities – such as wood, stone, brick wall, skin, cloud, rough sea, breast tissue etc. [Heeger, Bergen, 1995], [De Bonet, 1997], [Rolland and Strickland 1997], [De Bonet and Viola, 1998]. An interesting part of that problem relates to studying human visual perception [Bergen and Andelson, 1988], [Bergen, 1991], [Bergen and Landy, 1993], developing computational models of visual masking based on psychophysical data, and studying how one visual pattern affects the perception of another [Ferweda at al., 1997].

In the domain of computer-generated painterly effects, a problem is the determination of the appropriate orientation of the brush strokes and painterly rendering of the obtained image. An image for example may be "painted" with a series of spline brush strokes chosen to match the color of the source image [Hertzman, 1998], or rendered in a way that simulates artistic effects of watercolors [Curtis et al, 1997]. Other approaches to this problem are to select sets of orientable textures that follow the extracted features of the source object [Salisbury et al,

1997], or to visualize two-dimensional vector fields [Cabral and Leedom, 1993] and energy function, which after optimizing guides the streamlines at a specified density [Turk and Banks, 1996].

An interesting application of computer-simulated special effects is the creation of painterly effects that transform ordinary video segments into animations that have a hand-painted look [Litwinoxicz, 1997]. Similar techniques may be used to create special effects on streaming video. An example of computer-generated special effects modifying video segment is the movie “What dreams may come”, directed by Vincent Ward in 1998.

The most common approach employed in computer graphics to render special effects is raytracing [Spencer and Murty, 1961]. In this approach, appropriate sources of light are considered that emit light propagating as rays. The light illuminates the objects of interest, which are then visualized in the computer. Various techniques exist allowing the simulation of appropriate lighting and rendering [Phong, 1975], [He at al, 1991], [Westin, 1992], [Pharr et al, 1997].

1.2 Optics and Art

Although the field of computer-simulated special effects is developing and dominant, it has a major disadvantage. It requires the user or the artist to first record the images and to later modify them using appropriate equipment. Thus, the user is unable to preview the effect before the image is actually taken. For example if the users want to create computer-

simulated painterly effects on a picture, they can only use pictures that are already taken. Another example is moviemaking where the scene is first filmed and then special effects are added using computers. This disadvantage disappears if the images can be modified optically at the aiming of a camera. In this work, we shall focus on optically created special effects in photography and moviemaking.

If users are able to create special effects optically, at the speed of light, then they can preview the effect before actually taking the picture or the picture sequence. However, it is much more difficult to create special effects optically since the whole process has to be done in hardware. Also, the equipment must be portable and cost effective. Finally, in order to design optimized and cost effective hardware we need to be able to accurately model the optical imaging process.

Optics has been used in Art as early as the 15-th century when some artists used combinations of convex and concave mirrors to project images onto canvas. For example as the researcher David Hockney points out in Van Eyck's painting "Arnolfini Wedding" dated 1434, the artist depicted a convex mirror in the background that illuminates the entire scene in detail from the back [Hockney, 2001]. Researchers speculate that at this time some artists were using primitive optical systems to capture the perspective and the relationship of objects in the real world on canvas and then were finishing the paintings in freehand. Hockney also claims to observe effects of optical aberrations and depth of field and focus in the 16th-century paintings of Hans Holben and Lorenzo Lotto. Then, David Hockney and Charles Falco built a camera obscura on the Panavision soundstage and replicated the mirror-lens

projection system that they believe the old masters used to make their paintings [Hockney and Falco, 2000], [Zone, 2001].

Often times, when the word "Optics" is mentioned people tend to think in terms of lenses and mirrors only. However, an interesting approach for the creation of optical special effects is to use luminescence. For example, technologies such as optical fiber, black light, infrared light, fluorescence and ultraviolet light can create a variety of effects when used to illuminate different textiles, such as taffeta, satin, damask, velvet, jersey and lace [Helmi, 2001]. Another example is the creation of light emitting woven fabrics, based on the combination of optical and woven fibers, which when illuminated appropriately create painterly effects within the fabric [Hoggard, 1997].

A different area for optically simulated special effects is photographic camera design. There are various ways special effects can be created using either conventional or custom designed cameras. For example in 1999, Chicago-based Schumacher Camera announced the creation of the Revolution, an innovative snorkel lens system allowing the user to shoot at infinite angles without special rigging equipment [A lens revolution, 1999]. Innovative research by Frazier lead to a lens with large depth of field for special effects as it relates to cinematography [Frazier, 1998]. An emerging technology is that of Hylen who proposed a camera that allows imaging through an optical texture phase plate, creating textured-like images. [Hylen, 1997]

Finally, an innovative approach to use optics in art is also using spectral imaging for mapping of pigments in work of art [Baronti et al, 1998] and using a holographic technique called moiré patterns, which when recorded with a horizontal parallax create fascinating artistic effect [Liu et all, 1995].

1.3 Modelling of the Imaging Process

As preciously mentioned, the most common approach to render objects in computer graphics is raytracing. Other approaches include scalar diffraction theory, Fourier transforms and convolution with point spread functions, and statistical optics.

In the raytracing approach, the light is considered to propagate in straight lines, called rays, until it encounters an optical surface. Upon encountering an optical surface, the normal to the surface at the point where the ray hits the surface is being calculated and the vectorial law of refraction is consecutively applied. Such computations allow calculating the new direction of propagation of the ray. By sequential raytracing the location where a ray hits the observation point can be calculated, which allows calculating the light distribution at any point of interest.

Even though raytracing is a powerful method, it can only solve a limited number of problems where effects due to the wave or quantum nature of the light are negligible. However, when those effects cannot be neglected a more rigorous approach is required. For example if the problem is to model the imaging process through a complex optical surface, where the local

normal to the surface can not always be calculated, or if the surface contains features that are of the same order of magnitude as the wavelength, the raytracing will fail. In such problems, it is appropriate to use an approach based on Scalar Diffraction Theory. The light in such approach may be considered as a distribution of amplitude and phase that propagate through the optical system. In the special case when the system is linear, the propagation of the light can be modeled by applying a space-variant transfer function on the initial field distribution. Finally, if the system is also shift-invariant, the transfer function is also space-invariant.

Under the scalar diffraction theory, for a linear and shift-invariant system, the modeling of the light propagation can also be expressed in terms of Fourier transforms. Alternatively, one can calculate the overall point spread function (PSF) of the optical system and then convolve the object with the PSF. Such approach, which is most commonly applied, is only valid if the overall behavior of the system is linear and shift invariant.

If the optical system contains an optical surface located outside the pupil of the optical system, such as close to the image plane, that exhibits different optical properties across its surface, the overall system may not exhibit linear shift-invariant properties and in this case the imaging can not be described in terms of a convolution of the object with a PSF. In such systems two approaches are possible – one can propagate the optical field surface by surface, or alternatively one can calculate a probability density scattering function at each zone of the unique optical surface, and the computed or measured associated statistics can be combined with raytracing for imaging through such optical system. In the latter approach if a ray encounters a given zone of the unique surface within the optical system of interest, it will be

refracted at an angle in accordance with the probability calculated from the surface probability density function. Each of these approaches will be discussed in detail later in this work.

1.4 Motivation

A main challenge in the field of special effects is to create special effects in real time in a way that the user can preview the effect before taking the actual picture.

There are many techniques currently used to create computer-simulated special effects, however current techniques in computer graphics do not provide the option for the creation of real-time texture synthesis. Thus, while computer graphics is a powerful tool in the field of special effects, it is neither portable nor does it provide work in real-time capabilities. Real-time special effects may however be created optically. Such approach will provide not only real-time image processing at the speed of light but also a preview option allowing the user or the artist to preview the effect on various parts of the object in order to optimize the outcome.

In order to create a system that can optically modify and encode special effects into scenes we need the capabilities to correctly model the imaging process through such system. The need for accurate modeling of the imaging process as well as the need for optically simulated special effects motivates our current work.

1.5 Research Summary

Traditionally computer-simulated special effects are used in both photography and cinematography. These methods have some major disadvantages that we aim to remove by using optically simulated special effects.

The purpose of this work is to present a theoretical and experimental framework for modeling of the imaging process through a non-shift invariant optical system.

The framework presented in this work provides the accuracy required by the task and furthermore extends beyond the domain of special effects. The methods implemented to model the imaging process can be used to quantify any optical system that can be described in terms of the Scalar Diffraction Theory. Establishing such methods allow us to develop an experimental framework to implement optically simulated special effects.

1.6 Dissertation Outline

The remaining part of the dissertation is organized in the following way:

Chapter 2 gives an overview of existing compact optical relay systems, describes related work in the field of compact relay lenses for special effects, and reviews existing models of the imaging process.

Chapter 3 provides an in-depth discussion of the design of compact relay lenses and their applications. Novel compact imagers based on microlenslet arrays are presented.

Chapter 4 discusses experimental methods including the fabrication of the optical texture plates and the experimental modeling of an optical relay system, which combined with optical texture plates, can be used for optically-simulated special effects. Results from the experiments completed are provided in this chapter as well. Furthermore, Chapter 4 discusses raytracing as an imaging process in the context of the vectorial law of refraction. In this chapter, results produced by our implementation of the raytracing approach are presented.

Chapter 5 details the physical optics modeling of the imaging process through a unique optical surface such as an optical texture plate. In this chapter, a rigorous mathematical framework is established, and software is implemented both for single PC and for a Beowulf cluster. Problems related to the implementation of the mathematical model are discussed in detail and results from the simulations conducted are provided.

Chapter 6 summarizes the results and the contribution of the research. In this chapter the implementation of the research conducted as well as future work are discussed.

CHAPTER 2: RELATED WORK

In this chapter, related work in compact relay lenses for various optical applications is first reviewed, followed by various approaches to modeling the imaging process.

2.1 Relay Lenses

Many optical imaging systems require an intermediary image of an object to be formed, which then need to be relayed to a final image plane. Relay lenses are found for example in copy machines [Kawazi and Ogura, 1980], scanning devices, telescopes, conventional photographic cameras, endoscopes [Zobel, 2001] etc. In relaying an intermediary image to a final image plane, compact relay systems are often desired.

For some imaging devices, such as copiers or scanners, one of the common approaches to relaying the object is to use a stack of two 1-D linear arrays of lenses, with an intermediary image in between, which is moved across the object plane forming a composite image of the object in the detector plane. The image itself is typically binary (either white or black) and is further processed in the software or hardware of the imaging device, eliminating the need for high image quality.

Relay systems based on arrays of lenses are found in photolithography [Volkel et al, 1996] where a stack of four microlens arrays are used for 1:1 imaging of extended object planes,

and in 3-D integral imaging where macro-lens arrays in conjunction with microlens focusing screens are used [Davies et al, 1994]. Also, gradient-index fiber array arranged in rows to produce an erect image with unit magnification are employed in copy machines [Kawazi and Ogura, 1980], and gradient-index lens arrays are used in the design of line scanning systems [Toyama and Takami, 1982].

2.2 Relay Lenses for Special Effects

One of the main efforts in the photographic and cinematographic community is to create lenses with sufficient depth of field or alternatively depth of focus in order to create special effects in the obtained photographs or photograph sequences. A major break-through in this effort was the wide angle, large field of view, close focusing optical system conceived by J. Frazier [Frazier, 1998] during his work as a cinematographer shooting wildlife films in the outback of Australia [Probst, 1999]. With this lens, based on the concept of creating an intermediary image, which is then relayed to the final image plane, an almost infinite depth of field might be achieved. Another effort is to create special effects by encoding optical phase plates in an intermediary image, which is then relayed to the final image plane [Hylen, 1997].

2.3 Modelling of the Imaging Process

There are various possible approaches that can be used to describe an imaging process. The simplest among these approaches is raytracing, which is extensively used in various optical modeling software such as ASAP, Light Tools and TracePro. In this approach light propagates in the optical system as rays and upon encountering an optical surface the normal to the surface is calculated, then the vectorial law of refraction is applied to establish the new direction of the ray [Mouroulis and Macdonald, 1997], [Rolland, Shaoulov and Gonzales, 2001]. However, the raytracing approach imposes certain limitations on the surface of the optical elements, such as continuous second derivatives. For surfaces that cannot be described in such a way, such as fine structure optical phase plates, this approach can lead to inconsistent results with the experimental results.

The limitations upon the model of the surface of the optical elements will disappear if the imaging process is modeled using the concepts of physical optics. In this approach, a certain field distribution in the object plane is considered and consequently propagated through free space and optical elements sequentially. The field distribution at the image plane is directly obtained after applying the respective propagation kernels.

In existing off-the-shelf software, the main approach to imaging is the use of the Gaussian beam decomposition method. In this method, a Slowly Varying Envelope (SVEP) approximation is inherited. An arbitrary smooth field distribution in the object plane is assumed, which is then decomposed into a set of Gaussian wavelets. The sum of the wavelets

must approximate the original field to a certain degree, which imposes certain restrictions upon the original field. One potential problem in this approach is the fact that if the borders of the object are sharp, they can never be correctly modeled. Once the initial field in the object plane is decomposed into Gaussian wavelets each of the wavelets is propagated through free space up to a given point of interest or just before an optical element. At this point, the field is calculated again as the sum of all wavelets and is either resampled and propagated again or the final result is calculated.

Another approach in existing software such as ASAP and Light Tools is the Beam Propagation Method (BPM), in which the initial field distribution is propagated by applying a time domain finite-difference method. In that method the propagation time is sampled with certain finite-difference step and then the new field distribution at the new moment of time is calculated.

CHAPTER 3: DESIGN AND ASSESSMENT OF COMPACT RELAY LENSES

3.1 Conceptual Design of an Imaging System for Optically Created Special Effects

The key idea of using optical phase plates, to optically encode special effects in images, is to insert an optical phase plate close to the plane of the image and optically alter the image to obtain the desired special effect. The most intuitive optical layout of such optical system is demonstrated in the Fig.3.1. Alternatively, one can modify the image in some intermediate image plane and record the modified image on a detector (film, CCD, etc.).

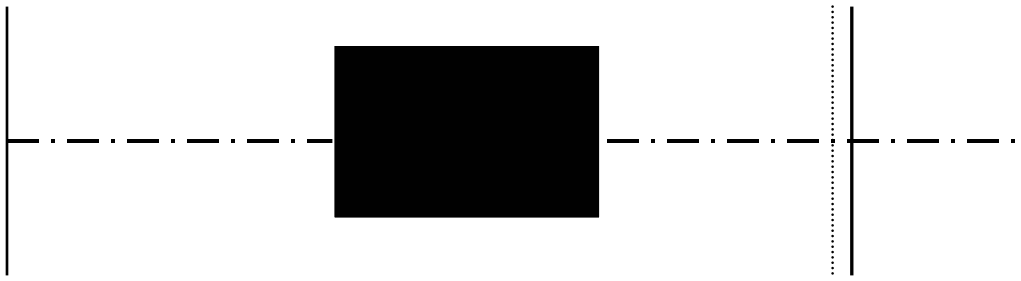

Figure 3.1 Optical layout of an imaging system, where an optical phase plate is inserted close to the final image location.

The initial experiments demonstrated that the configuration demonstrated in Fig. 3.1, while simple, is not the optimal in terms of controlling the optical special effects in the final image.

Severe shadows on the final image were observed. It was concluded from early experiments conducted by Steve Hylen, expert photographer, that the best configuration should allow the formation of an intermediary image in an intermediate image plane, where the intermediary aerial image can be modified by inserting an optical phase plate. Furthermore, the modified intermediary image should be relayed by some compact relay optics to the final image location where it would be recorded using a detector device, such as a photographic film or a CCD. The conceptual optical layout of such imaging system is demonstrated in Fig.3.2.

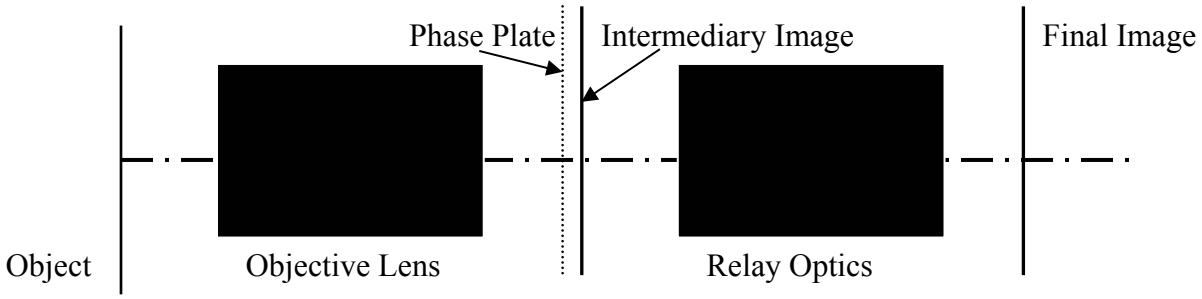

Figure 3.2 Optical layout of an imaging system, where an optical phase plate is inserted in an intermediate image plane where it is modified and is further relayed to the final image plane.

In the configuration shown in Fig. 3.2, an objective lens forms an aerial intermediary image of the object in some intermediate image plane. In, or close to this plane (i.e. ~5mm distance), an optical phase plate can be inserted to optically modify the image in a controlled fashion. Finally, the modified image is relayed by relay optics to the final image location, where it is recorded.

3.2 Design of Compact Macro-Optics Relay Lenses

Based on the conceptual design demonstrated in Fig.3.2, an experimental setup was built to assess the feasibility of the conceived system. Based on the preliminary results from the experimental setup, we concluded that the conceived conceptual design for optically created special effects was feasible. The experimental procedures are further detailed in Chapter 4. Furthermore, an optimized solution allowing the integration of the conceived conceptual design in both conventional off-the-shelf cameras and single-use cameras had to be proposed and assessed.

While the objective lens is a standard component of any commercially available camera, the key challenge in the conceived system was designing an ultra compact custom relay optics. One core issue in designing such relay optics is to match the exit pupil of the objective lens with the entrance pupil of the relay optics, which allows all of the light exiting the objective lens to be relayed to the final image plane with close to zero vignetting. To achieve this, several measurements of the size and location of the exit pupil of a standard 50mm Nikon objective lens were performed, using a collimated He-Ne laser beam as a source, as detailed in Chapter 4. The measurements yielded a pupil size of about 5mm located approximately 40mm behind the last optical surface of the objective lens. Thus, the main specifications in the relay optics design were determined and summarizes in Table 3.1

Table 3.1 Optical specification of a relay lens: Design of a Relay Lens to Interface a 50mm Nikon Objective

Design parameter	Design criterion/Goal
Camera objective lens	F/7
Nikon lens pupil position	15mm from last surface
Texture plate	0.7mm thick
Film image size	24mm by 36mm format
Spectral weights	From 430nm to 650nm
Compact	Less than 100mm length
Clearance to film	Greater than 40mm
Clearance to film	Greater than 5mm
Pupil matching	Must be achieved
Field curvature	Minimized
Modulation Transfer Function	Greater than 20% at 20 cycles/mm
Prototype cost including lens barrel	Less than $15,000 (achieved $7,500)

Based on the table of specifications, a final design was conceived as shown in Fig. 3.3. [Rolland, Hua and Shaoulov, 2002] First, a field lens (i.e. achromatic doublet) is used to demagnify the image produced by the standard 50mm Nikon objective lens by a factor of 2. Such imaging allows bringing the image closer to the objective lens as well as using smaller optical phase plates (i.e. ½ of the standard 35mm film size) to modify the intermediate image. The field lens is also used to correct for field aberrations in the system. Furthermore, a modified double Gauss is used to relay the modified intermediate aerial image to the final image plane, while magnifying it back to its original size (i.e. 24 by 36mm). The optical Lagrange invariant controls all the size-angle relationships. The dissymmetry in the double Gauss is dictated by the change in the F-number by a factor of 2 on each side of the relay lens (i.e. the magnification on each side of the double Gauss changes by a factor of 2).

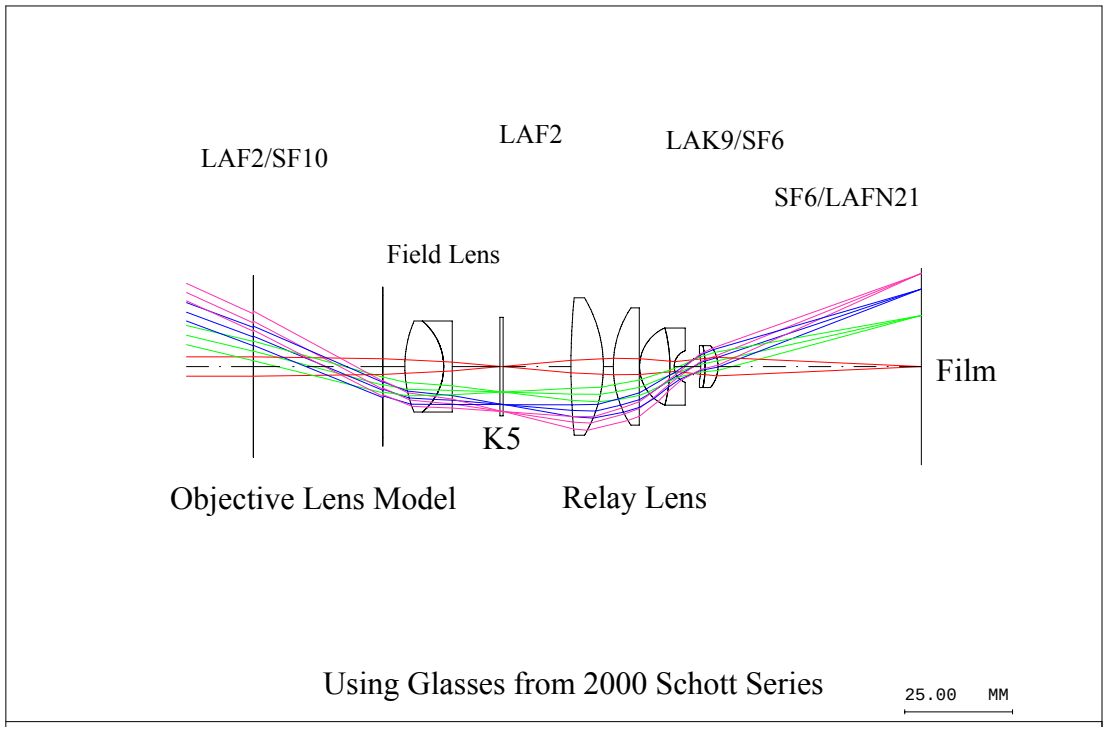

Figure 3.3 Optical layout of a compact relay 1:1 system.

The performance of the conceived relay lens is demonstrated in Fig. 3.4 (a) and (b) and it is thus seen that the desired criteria of MTF greater than 20% at 20lp/mm is satisfied. The MTF is well behaved over all fields and the astigmatism is negligible. Thus, the image quality of the system is controlled by spherical aberration and transverse chromatic aberrations. However, since the system is designed specifically to introduce special effects into aerial intermediary image some additional blur is desirable.

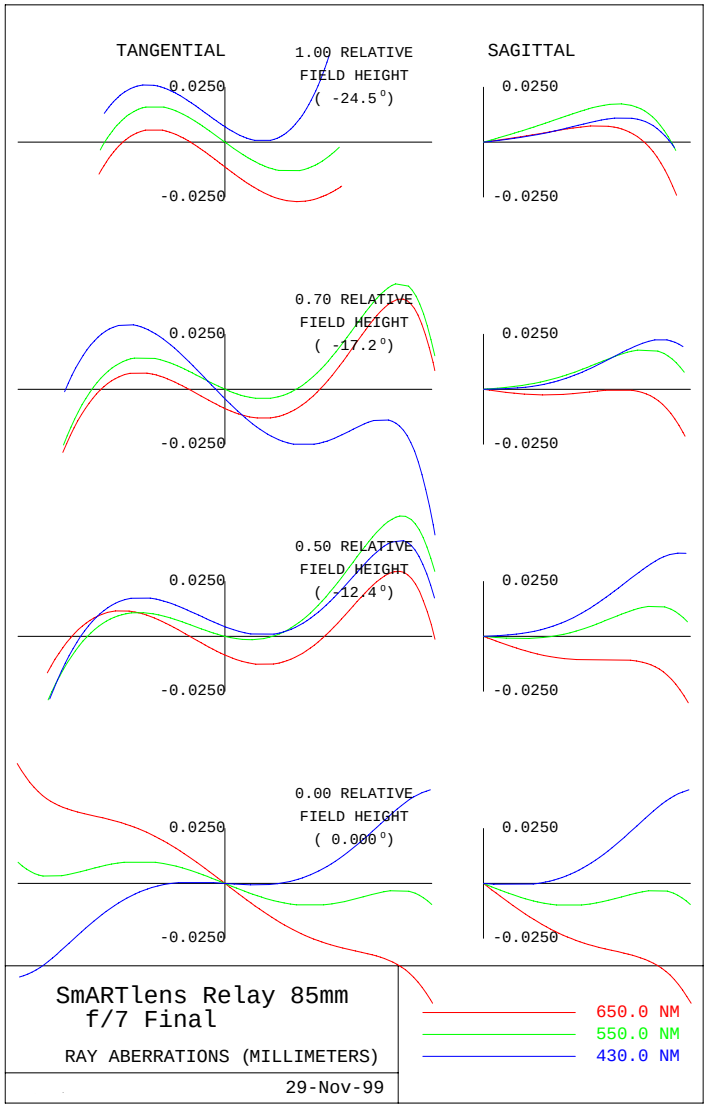
TANGENTIAL
SAGITTAL
1.00 RELATIVE
FIELD HEIGHT
(-24.5°)
0.70 RELATIVE
FIELD HEIGHT
(-17.2°)
0.50 RELATIVE
FIELD HEIGHT
(-12.4°)
0.00 RELATIVE
FIELD HEIGHT
(0.000°)
0.0250
-0.0250
SmARTlens Relay 85mm
f/7 Final
RAY ABERRATIONS (MILLIMETERS)
29-Nov-99
650.0 NM
550.0 NM
430.0 NM

(a)

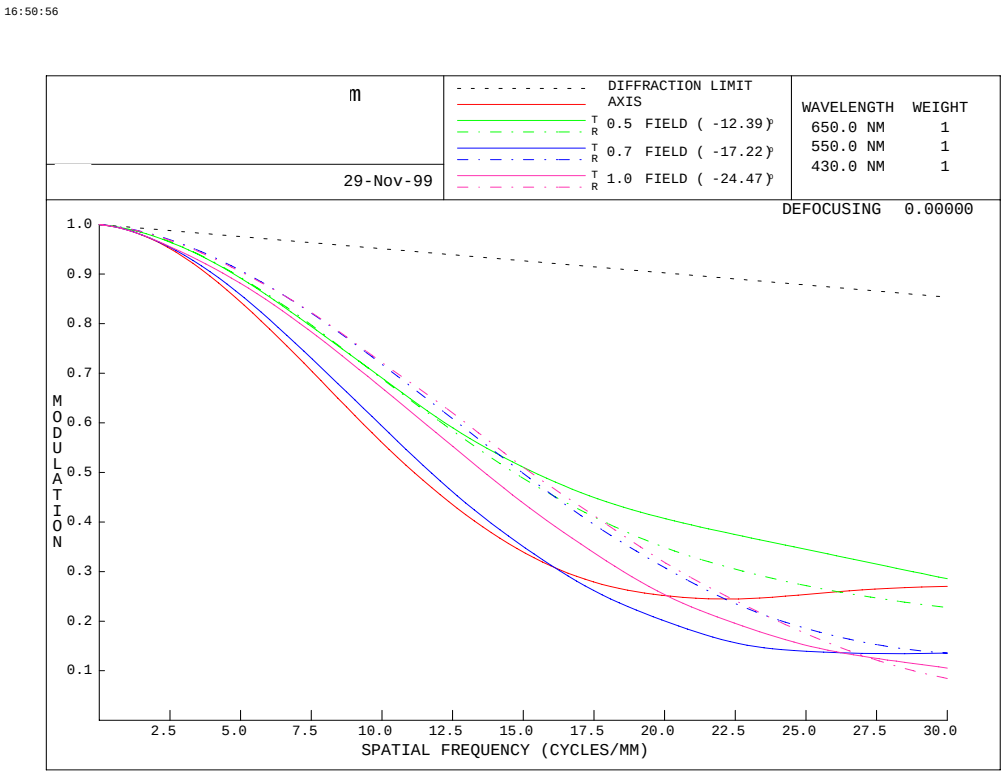

(b)

Figure 3.4 Optical design assessment (a) ray fan plots; (b) Modulation transfer functions.

Based on the conceived design, a prototype was build and tested as further detailed in Chapter 4. Such relay lens was conceived to interface to a 50 mm photographic camera. While compact and lightweight for its purpose, the conceived relay lens was still too bulky (i.e. ~120mm object to image distance, and ~800 grams of weight) to be integrated into a single use camera for example. Other alternatives for even more compact design were thus considered. The main goal was to achieve a more compact, robust, and low cost optical relay.

To satisfy such requirements, optical magnifying systems based on microlenslet arrays were investigated.

3.3 Imaging with Microlenslet Arrays

The imaging properties of microlenslet arrays and associated baffles for binary (i.e. black and white) imaging, such as the imaging needed in copiers and scanners, were first investigated by R.H. Anderson. [Anderson, 1979] In his work, Anderson demonstrated that arrays of simple lenses combined with appropriate baffles could be used in close-up imaging systems for black and white document copiers, oscilloscope cameras, as well as binary code scanners. Microlenslet-array based imaging systems were consequently further investigated for optical scanners and copiers, [Anderson, 1979], [Kawazi, Ogura, 1980], [Toyama, Takami, 1982], 3D integral photography, [Davies et. al, 1994] printers, [Mir, 1983] and photolithography. [Volkel et. al, 1996] Current state-of-the-art micro-optics fabrication facilities make possible the manufacturing of microlenslet arrays of extremely short focal length with apertures of various shapes and size comparable to the wavelength. Microlenslet arrays with refractive, diffractive, anamorphic, spherical and aspherical positive and negative optical surfaces are currently available.

First, we investigated various first-order paraxial layouts for 1:1 imaging and associated baffle placement to eliminate ghost images. Furthermore, we detailed the technical aspects of the software simulations with respect to how rays are precisely being traced to maximize efficiency and how many rays were necessary to obtain high signal-to-noise ratio images.

We then quantified the image quality in terms of *lensletization*, a tiling effect that may be observed in images formed with microlenslet arrays. Such tiling effect, which highly degrades image quality, is dominant in certain first-order layouts. First steps to image quality assessment in such systems is thus to establish conditions for minimized tiling, and in this context discuss the compactness, the resolution limit imposed by diffraction, and the optical aberrations of such systems. Finally, we generalized the theory of imaging with micro-optics to optical magnifying systems for imaging at various magnifications and we established the detailed relationships necessary to describe the most general case of imaging with two stacks of microlenslet arrays and the appropriate baffles. A key contribution of this work is the replacement of bulk macro-optical system by multi-aperture micro-optics.

3.3.1 Paraxial Layout of 1:1 Imaging with a Pair of Microlenses

Many possible configurations of two lenses satisfy 1:1 image relay conditions. [Shaoulov, Rolland, 2002, 2003] The difference among them lies in the overall length of the optical system and its field of view. The arrangements investigated in our work are shown in Fig. 3.5. We consider for all systems that each pair of lenses is of same focal length f and same diameter D. In this case, the overall length denoted as OAL of such system defined as the distance from the object to the final image plane is given by

$$OAL = \frac{2x^2}{|x| - |f|} \quad , \tag{3.1}$$

where x is the distance from the object to the first lens in each pair.

The minimum of the function given by Eq. (3.1) takes place at $|x|$ equal to $2|f|$, which yields the most compact configuration. Thus the most compact possible arrangement is the "2f-4f-2f", thereafter referred to as the *2f-system*, in which the object is located at a distance 2f in front of the first lens, an intermediary image is formed at a distance *2f* after the first lens with a magnification of -1, which is consequently imaged at a distance *2f* after the second lens with a magnification of -1. Thus, the total magnification of the system is +1. Provided the symmetry of the systems, the full field of view measured in the image plane, denoted as *FOV* in millimeters, and defined as 100% vignetting at its edge is most generally given by

$$FOV = (K-1)D \quad , \tag{3.2}$$

where K denotes the system type, e.g. for the 2f-system K equal 2 and the full *FOV* is equal to the diameter of the lens, D, in millimeters.

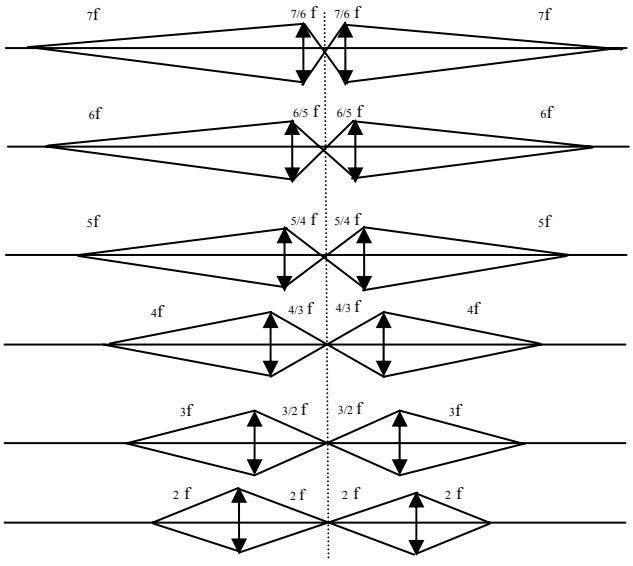

Figure 3.5 Paraxial layouts of 1:1 imaging with a single pair of microlenses.

3.3.2 Optical Layout of 1:1 Imaging with a Stack of Two Microlenslet Arrays

The concept shown in Fig. 3.5 is simple and compact, yet it cannot be simply extended to arrays of lenses because of the formation of ghost images. [Anderson, 1979] The formation of ghost images is illustrated in Fig. 3.6 with the most compact arrangement, which is the 2f-system, where five elements in each array are considered for illustration. The raytrace demonstrates 1:1 image formation as well as multiple ghost images.[Shaoulov, Rolland, 2002, 2003] Thus, appropriate baffle arrays must be used in combination with the arrays of lenses to prevent ghost images.[Anderson, 1979]

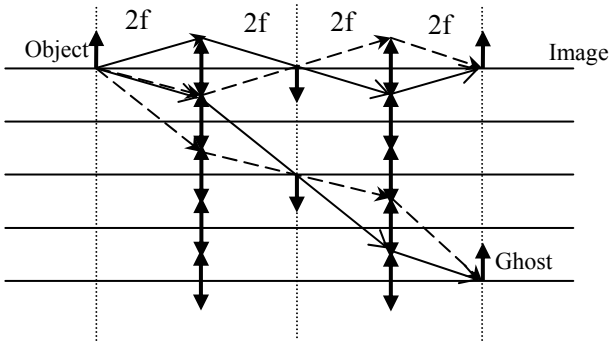

Figure 3.6 Ray sketching illustrating the presence of ghost images for a stack of two microlenslet arrays without any baffles.

In order to determine the location and size of the appropriate baffles needed to eliminate ghost image formation in the system, let's consider the 2f-system shown in Fig. 3.6. Let's denote the first and second lens L_1 and L_2, respectively. From the theory of pupils and stops, we observe that both L_1 and L_2 limit equally the amount of light entering the system from a considered point object on axis, thus any one of them can be chosen as the aperture stop, the

other one being automatically the window. [Mouroulis, Macdonald, 1997], [Rolland, Shaoulov, Gonzales, 2001] Let's assume without loss of generality that L_1 is the aperture stop (AS) of the system. We could as well assume L_2 to be the AS of the system, leading to identical results. The exit pupil of the optical system is by definition the image of the AS in image space. From the Descartes imaging equations, the location and size of the exit pupil for the 2f-system are calculated to be at 4/3 $|f|$ after the second lens and three times smaller than the diameter of L_1, respectively. Similarly, the location of the entrance window is computed as the image of L_2 through L_1. In the most general case, Eq. (3.1) can be expressed in terms of K as follows

$$OAL = \frac{2K^2}{K-1} f \,. \tag{3.3}$$

Thus, the location of the entrance pupil with respect to L_1 is given by

$$E.P.L. = -\frac{2K}{K+1} f \,. \tag{3.4}$$

Because of the symmetry of the system, the location of the exit pupil will be the same with respect to L_2. Furthermore, the image of the AS through L_1, and alternatively through L_2, is demagnified by a factor of

$$m_{L_{1,2}} = \frac{K-1}{K+1} \,. \tag{3.5}$$

Thus, the size of the entrance and the exit pupils is given by

$$D_{En.P.,Ex.P.} = \frac{K-1}{K+1} D \,, \tag{3.6}$$

where we again assumed $D_{L_1} = D_{L_2} = D$. Thus, we generalized all size and location relationships in the relay 1:1 systems.

The formation of ghost images may be prevented by placing baffles at the locations of the entrance window or the exit pupil, computed from Eqs. (3.4) and (3.6). In his investigation, Anderson had proposed baffles at both locations, however one set of baffle is sufficient given that they are optical conjugate of each other.[Anderson, 1979] Such simplification, validated in the simulations presented further in this Chapter, will bring significant benefits to the cost of fabrication and packaging. One of the two possible locations of the baffle for the 2f-system (i.e. a baffle located at the entrance window) is shown in Fig. 3.7. With the appropriate baffle, we predict a ghost-free image formation of each object point.

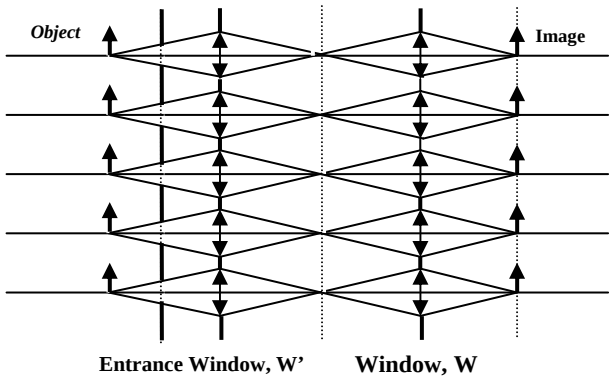

Figure 3.7 Microlenslet arrays 1:1 imaging 2f-sytem with appropriate baffle to minimize ghost images.

A property of a multi-aperture optical imaging system (i.e. an optical system with a stack of two microlenslet arrays) is the sampling of the object by each set of sub-apertures (i.e. pair of microlenslets in the stacks), where each set of sub-apertures operates over a limited field of view given by Eq. (3.2). Using paraxial layout, image formation with a stack of two arrays is shown in Fig. 3.8. (a) and (b) for the 2f- and the 5f-systems, respectively. It is only through

the entire stack that the entire field of view is imaged. Thus, another key contribution of our work is the conclusion that increasing the overall FOV, when using a multi-aperture micro-optics, requires simply adding more lenses to each array, while leaving the imaging properties of the system otherwise invariant (as opposed to the bulk macro-optical systems, where increasing the overall FOV of the system requires complete redesign of the system itself). Under the most compact configuration, it is shown in Fig. 3.8.(a) that the imaged sub-fields of view (sub-FOV) through each pair of microlenslets do not overlap, thus creating gaps in the irradiance distribution of the final image, while the effect is less pronounced if existent for the other systems. This new effect in optical imaging with multi-apertures (e.g. microlenslet arrays), first demonstrated here in images, is denoted as *lensletization*. To overcome this effect, an overlap of the sub-FOVs for each individual set of apertures (i.e. pair of microlenses) is required at the expense of compactness and the natural loss in resolution that accompanies the overlapping sub-FOVs. Further analysis will be presented in Section 3.3.3.2 to quantify the impact of lensletization on image quality for the investigated configurations. Given an extended small object seen by each lenslet, lensletization decreases with increased vignetting induced by the baffle and the amount of overlap of the sub-images formed by adjacent lenslets. For example in the 2f-system, the FOV of each individual pair of lenses measured in the object plane is equal to the aperture of the lens, and therefore pronounced lensletization occurs. As the overlap of the sub-FOVs, lensletization decreases at the expense of a loss in compactness. Such trade-off will be further investigated in Section 3.3.5. In the configurations with overlapping sub-FOVs (i.e. $K > 2$), the presence of varying vignetting across the sub-fields as well as the effect of optical aberrations on each point seen

by multiple lenslets do not allow for modeling and evaluation of the lensletization effect as a simple convolution.

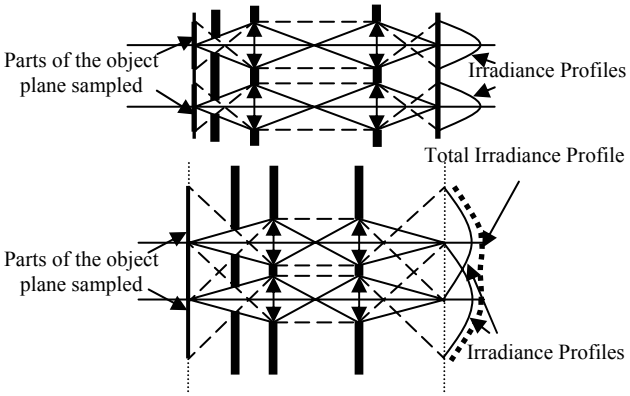

Figure 3.8 Illustration of the irradiance profiles of an extended object imaged through (a) a 2f-system microlenslet arrays relay lens; (b) A 5f-system.

3.3.3 Modeling the Imaging Properties of the System with Simple Light Sources

In order to analyze further the imaging properties of microlenslet arrays, a computer model for imaging was developed using custom-designed software based on the ASAP^{TM} kernel. The first aspect of modeling is to define the light source or equivalently an object to be imaged. In order to first gain insight into basic imaging properties, such as image resolution, noise, and lensletization, we selected as an initial light source a white ellipse on a black background, which allows simple metrics to be used to quantify image quality. Consequently, more complex grayscale light sources, such as bitmap portraits, will be presented to comprehensively assess the grayscale imaging capability of microlenslet arrays.

In the case of grayscale images, image quality may be assessed qualitatively, as well as quantitatively as the difference between the relayed image and the initial image (i.e. also referred as the object).

The optical layout of a 2f-system using two arrays of 11 by 11 microlenses in each array combined with an associated baffle, located without loss of generality before the lenslet arrays, is shown in Fig 3.9. Furthermore, each lens in the array is a square F/5 plano-convex lens, 0.15 mm thickness, and 5mm focal length. Because we use simple plano-convex singlets, which inherently have significant axial chromatic aberration, we only consider imaging one color grayscale image, which we selected without loss of generality to be λ equal to 656nm. Such parameters, combined with an elliptically shaped light source, are used in all the simulations presented in this Chapter.

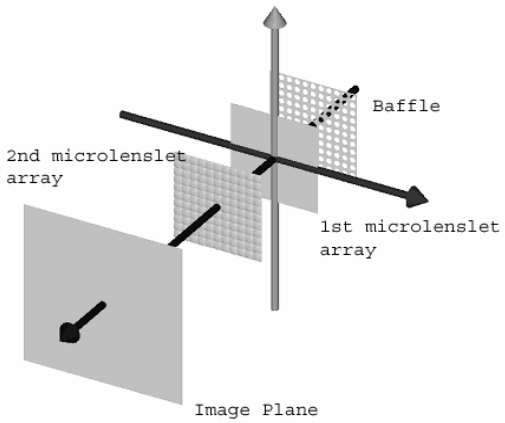

Figure 3.9 ASAP^{TM} layout of the 2f-system microlenslet array based relay system with two 11 by 11 arrays of microlenses and the appropriate baffle. The object to be imaged is not represented in the figure, however from right to left, the baffle, the two microlenslet arrays

made of plano-convex square lenses, and the detector upon which an image will be formed given an object in front of the baffle, are shown.

3.3.3.1 Establishing a minimum number of rays

In raytracing-based simulations, noise may be modeled per Bernoulli's trials, a probability law that statistically describes whether a ray reaches the detector or not. Let us consider the noise associated with each pixel in the detector. In this case, the probability of a ray reaching a pixel is small with respect to 1, and the probability density of noise associated with a pixel reduces to a Poisson distribution.[ASAP, 2002] Thus, the standard deviation of the noise is equal to the square root of the number of rays per pixel, n, in the image plane. Given the quantification of raytracing efficiency, the signal-to-noise ratio (SNR) in the imaging process, which varies as the square root of n, enables selecting a minimum number of rays emitted per pixel in object space.

Let's denote η the efficiency of raytracing defined as the ratio of the total number of rays reaching the detector plane over the total number of the rays x emitted from the object, and as N the total number of pixels in the object and thus in the image. The SNR as a function of x may then be expressed as

$$\text{SNR (dB)}(x) = 10 \log_{10} \left(\sqrt{\frac{x}{N}\eta} \right) \quad . \tag{3.7}$$

To further quantify the SNR as a function of the number of rays per pixel (i.e. $n = x/N$), we need to first quantify the efficiency η which varies with each configuration and the optical raytracing approach implemented, thereafter referred to as the approach. First, it can be shown that efficiency varies with the various configurations, and for the most optimum approach, the efficiency increases from about 5% in the *2f* configuration to 40% in the *7f* configuration, respectively. However, if it can be shown to vary in the most optimum approach, it necessarily varies in the other sub-optimum approaches. One sub-optimum approach is when no optimization is established in a bitmap raytrace. In this case, the efficiency of the process is extremely low. For example, for the 5f-system, 0.4% efficiency was established as detailed in next paragraph. Thus, in order to limit the simulations to 1% Poisson noise, or equivalently a SNR of 100 (20dB), approximately 2×10^{20} rays would need to be traced for a 91 by 91 pixels bitmap object! Using a standard 2.0 GHz processor, such calculation would take approximately 6 weeks.

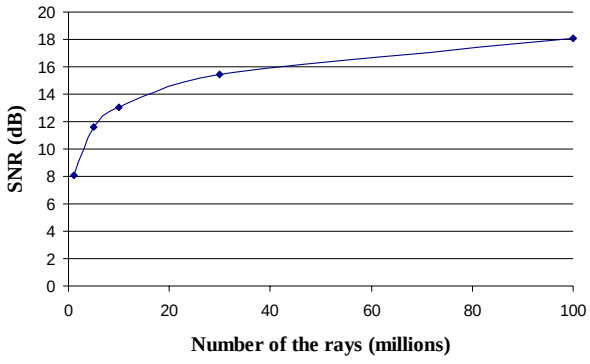

Figure 3.10 SNR for the 5f-system as a function of the number of rays emitted from the object, using Eq. (3.7). In this plot N equal 8281 pixels, and η equal 34%.

Losses in the system, and thus efficiency, were then evaluated by setting a test detector surface consecutively at different planes and evaluating the number of rays reaching that test surface. The raytrace started with a given number of rays emitted from the object. Then the loss per element was evaluated as a function of the difference between the number of rays just before and just after each optical element. Such raytracing allowed identifying the surfaces where the actual loss of rays occurred and determining the overall efficiency of the raytrace. The results produced showed that out of 100% light-rays on the test surface just before the first baffle, 0.4% reached their aimed destination, thus yielding an overall efficiency of the raytrace of 0.4% in this case.

One level of optimization in optical raytracing procedures is to direct the rays towards the entrance pupil of the optical system. While in the case of multi-aperture micro-optics, such as stacks of microlenslet arrays, no single pupil exists but instead many sub-pupils must be considered, a fictive pupil can be defined that encompasses all the sub-pupils. Rays are directed toward the fictive pupil, which is accomplished by placing a diffuser in front of the object. Such diffuser captures all rays emitted from the object before scattering and redirects them towards the entrance fictive pupil of the optical system. Such optimization increased the efficiency of the raytrace by a factor of about 45 (e.g. from 0.4% to 17.5% for the 5f-system), which still required tracing approximately 500 million rays for a 91 by 91 pixels object. A property of this scattering technique is that each ray reaching the diffuser splits into one "parent" ray, which propagates according to Snell's law of refraction, and at least one "child" ray, which is generated uniformly within the cone defined by the fictive pupil.

Building on this scattering technique, which is standard in ASAP^{TM} Software, the raytrace was further optimized by splitting the raytrace in two separate raytraces. The rays were first traced from the source to the diffuser, then only the "child", or scattered rays, (i.e. as opposed to both the "parent" and "child" rays) were raytraced from the diffuser towards the entrance fictive pupil of the system. This last optimization further increased the overall efficiency of the raytrace by a factor of about 2 (i.e. the efficiency was 34% for the 5f-system) from the last optimization or a factor of 90 from the original, non-optimized, raytracing. The SNR(x) for the most efficient raytracing approach is shown in Fig. 3.10 for the 5f-system. Results show that 100 million rays, which are feasible to trace within a day, yield a SNR of 18dB or equivalently 1.6% noise. To satisfy 1% of noise in the final raytrace, raytracing 250 million rays would still be required. However, no significant contribution to the accuracy of the results would be achieved. In the simulation presented, we traced 100 million rays, which produced results with less than 5% noise (e.g. 1.6% noise in the 5f-system). Such noise level allowed for the quantitative evaluation of the image quality of the system while keeping the duration of a single raytrace within the range of a few hours.

Results of simulations using an elliptical light source and 100 million rays are shown in Fig. 3.11 for the various imaging configurations reported in Fig. 3.5. Fig. 3.10 also reports additional analysis of the simulations as now discussed in Section 3.3.3.2.

3.3.3.2 Quantification of Lensletization

The lensletization effect defined in Section 3.3.2 was quantified by computing the normalized autocorrelation function of the image as well as the normalized autocorrelation function of the original object for a cross section through the center of both the object and image (i.e. the ellipse), as shown in Fig. 3.11 (a), and Fig. 3.11 (b) – (g). The computed normalized autocorrelation functions from the images obtained with the various configurations were subtracted from the normalized autocorrelation function of the object to assess the departure of the autocorrelation function of the image from its expected value. In Fig. 3.11 (a), we present the object, the irradiance distribution along the central cross-section, and the computed normalized autocorrelation function. In Fig. 3.11 (b), we presents the image obtained for the 2f-system, the irradiance distribution along the central cross-section, the computed normalized autocorrelation function, and the subtracted normalized autocorrelation function of the object and the image. Similar functions are shown for the other configurations in Figs. 3.11 (c) – (g).

The effect of lensletization due to the microlenses in the arrays is observed as an oscillating curve in the subtracted autocorrelation functions. The lensletization in the image of the 2f-system, as well as the 3f-sytem while less pronounced, is clearly observed. While the 2f-system is most compact, the lensletization makes this configuration unsuitable for imaging of grayscale images. Lensletization subjectively appears to be negligible for the 4f-system, and becomes even less pronounced as expected for the 5f, 6f, and 7f systems. Quantitatively, we computed both the peak-to-valley (P-V) error in the subtracted normalized autocorrelation

function, and the RMS error. The data obtained are presented in Table 1. Results show that both the P-V and RMS error are twice as large or higher for configurations below the 5f-system. We can establish in these simulations that a P-V < 2% in the subtracted autocorrelation or an RMS error of < than 0.6% in RMS leads to negligible lensletization. In the case of the simulations presented, the propagation of noise from the images to the autocorrelation function was found to be negligible, which is consistent with the results of both P-V and RMS error presented. In this case of low noise, both the P-V and RMS error may quantify the lensletization effect. In the case of noisiest images, further investigation would be required to quantify how noise in the images propagates to the autocorrelation function to establish whether the P-V would still be an acceptable measure of lensletization. The RMS error intrinsically includes both the lensletization effect and the standard deviation of the noise in the computed autocorrelation.

Table 3.2 Peak-to-valley error in the difference between the normalized autocorrelation of the object and the resulting image.

System Configurations	Peak-to-Valley	RMS Error
2f	0.675	0.182
3f	0.020	0.006
4f	0.020	0.006
5f	0.009	0.002
6f	0.009	0.003
7f	0.010	0.003

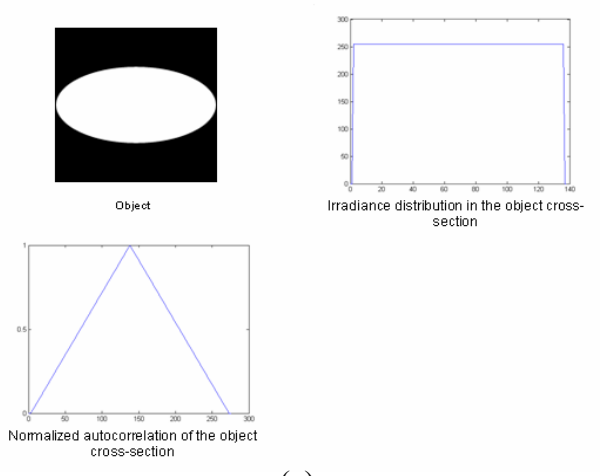

(a)

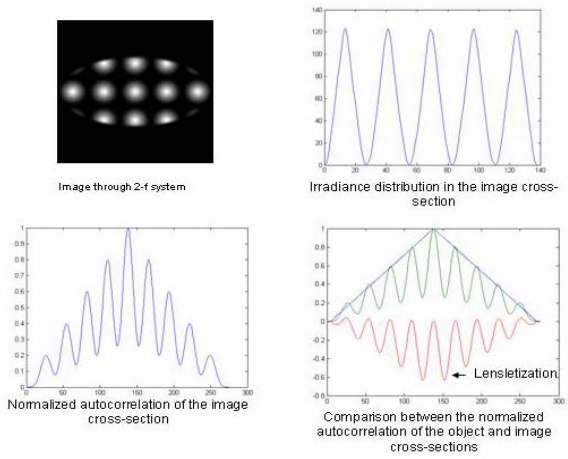

(b)

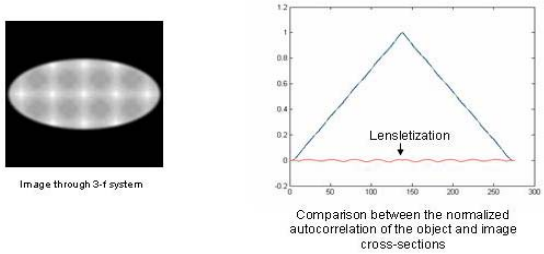

(c)

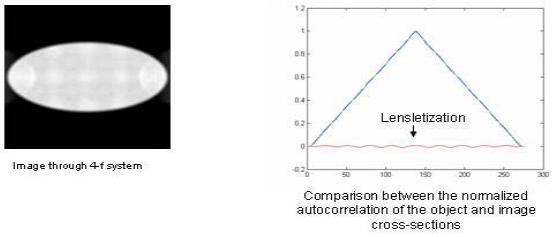

(d)

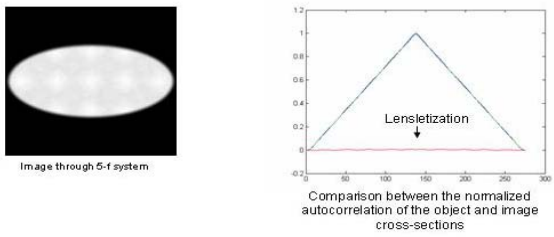

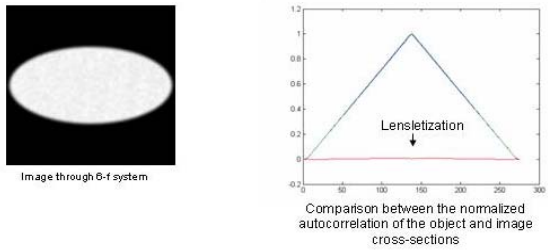

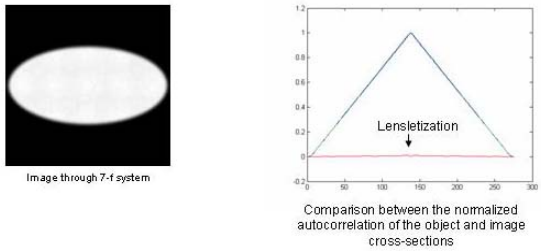

(e)

Figure 3.11 Imaging and irradiance distribution of an ellipse: (a) original image (b) image

through the 2f-system (c) image through the 3f- system (d) image through the 4f-system (e) image through the 5f-system (f) image through 6f-system (g) image through the 7f-system. For the irradiance distributions the grey level value vs. the number of pixels in the object is plotted. The autocorrelation functions of the image are plotted in arbitrary units.

3.3.4 Modelling of the Imaging Properties of the System for Greyscale Images

Imaging simulations with grayscale objects (i.e. bitmap images) were created using the various imaging configurations presented in Fig. 3.5. The number of rays used was 100 million rays as well. Results are shown in Fig. 3.12. To our knowledge, the modeling of imaging of grayscale bitmaps through stacks of microlenslet arrays is first demonstrated in this work. The challenge with imaging grayscale bitmap images is that no artifacts such as apparent lensletization are tolerable in the image. Therefore, the range of optical configurations yielding no apparent artifacts must be established. In the case of binary images (i.e. black and white patterns), simple post-processing operations on the images such as thresholding can be applied to recover necessary image quality for the task at hand (e.g. recognizing a letter). Such processing is not applicable to grayscale images and a fundamental question was whether a system may be designed to eliminate lensletization artifacts, while preserving sufficient image quality in terms of resolution, and the ability to represent sufficiently a range of grayscales. It has been only through this investigation of imaging grayscale images that the issue of intensity variations in the image, which we have further defined as lensletization, has become critical to the system optimization. Results indicate that artifacts of the microlenslet arrays are observed in the *2f, 3f, and 4f* systems,

which is consistent with the results obtained and quantified for the ellipse light source. No artifacts seem observable for the *5f, 6f, and 7f* systems (and naturally any system beyond *7f* as well).

An analysis of the image quality of the 5f-system shows that the diffraction limited point spread function (PSF) is 33µm, which in the simulation is less than the pixel size in the image (i.e. 55µm). Given that simple plano-convex singlets were considered in the simulations, the monochromatic (i.e. λ equal 656 nm) modulation transfer function (MTF) is found to hold reasonably well across the sub-fields of view of each pair of microlenses in the stack. The plano-convex lenses are oriented with their convex side towards the longer conjugate to minimize the aberrations. The MTF satisfies 20% modulation at 18 cycles/mm up to 80% of the full FOV. The equivalent PSFs shown in Fig. 3.13 for the 0%, 70%, 95%, and 100% vignetted FOVs, illustrate the broadening of the PSF with FOV. Furthermore, the system is not fully symmetrical around the aperture stop and the local distortion across each sub-fields of view is computed to be less than 10% up to 70% of the full sub-fields of view, and 25% at the edge of each sub-field of view. Finally, given that each lenslet is a singlet and the system is not symmetric around the pupil, the system currently suffers from both axial and transverse chromatic aberrations. A simulation of a red, green, and blue (i.e. λ equal 656nm, 587nm, 486nm, respectively) self-emitting image is shown in Fig. 3.14. Per the simulation, the overall chromatic aberrations are shown to contribute additional blur to the image in its present un-optimized stage.

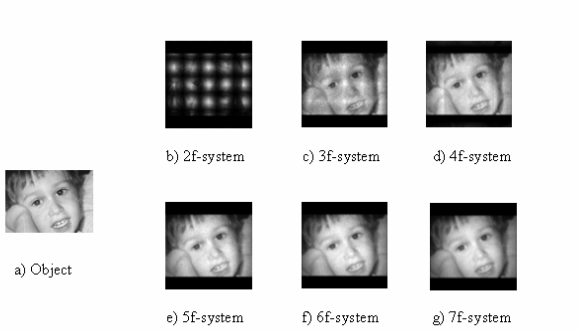

Figure 3.12 Imaging and irradiance distribution of a grayscale bitmap object: (a) original image; (b) image through "2f" system; (c) image through "3f" system; (d) image through "4f" system; (e) image through "5f" system; (f) image through "6f" system; and (g) image through "7f" system.

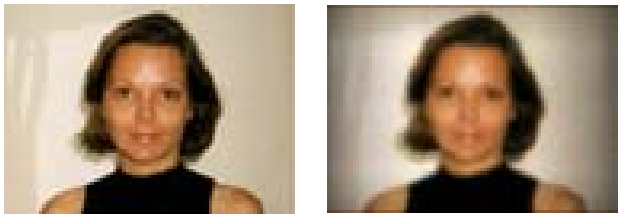

(a) (b)

Figure 3.13 Simulation of imaging of an RGB image through a stack of two microlenslet arrays to qualitatively assess the impact of chromatic aberrations on image formation.

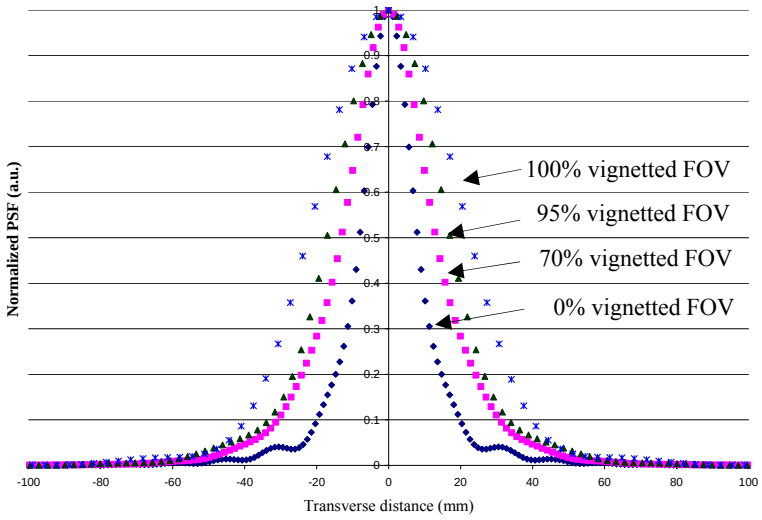

Figure 3.14 Normalized PSF plots for 0%, 70%, 95% and 100% vignetted sub-fields of view for a pair of plano-convex lenses.

3.3.5 Systems compactness

The compactness of each configuration, defined as the overall length (OAL) from the light source to the image plane, is given by

$$OAL = \frac{2K^2}{K-1} f \,, \tag{3.8}$$

where the OAL is shown to scale linearly with focal length If we set the focal length of each microlens to 0.5mm according to commercially available microlenslet arrays and we consider the 5f-system, which yields no lensletization, the OAL is only 6.25mm. Results of compactness computations as a function of the system configuration (i.e. the *M* parameter) are reported in Table 3.3.

Table 3.3 Overall compactness of the microlenslet arrays.

Type of system	OAL(mm) for f = 0.5mm
7f	8.2
6f	7.2
5f	6.25
4f	5.3
3f	4.5
2f	4.0

3.3.6 Paraxial Layout of 1:M Imaging with a Stack of Two Dissimilar Microlenslet Arrays.

Once the feasibility of replacing bulk macro-optics with multi-aperture micro-optics was established and detailed relationships describing the imaging process were obtained, the next step was to generalize our findings to the most general case of multi-aperture optical systems of various magnifications.

There are numerous possible configurations that can be used to create an optical 1:*M* magnifying system, as shown in Fig. 3.15 for a system with an overall magnification of *M* greater than 1, which can be further extended to imaging with a stack of two dissimilar

microlenslet arrays, as shown in Fig. 3.16.[Shaoulov, Martins, Rolland, 2003] The general case for a stack of two microlenslet arrays is illustrated in Fig. 3.15.

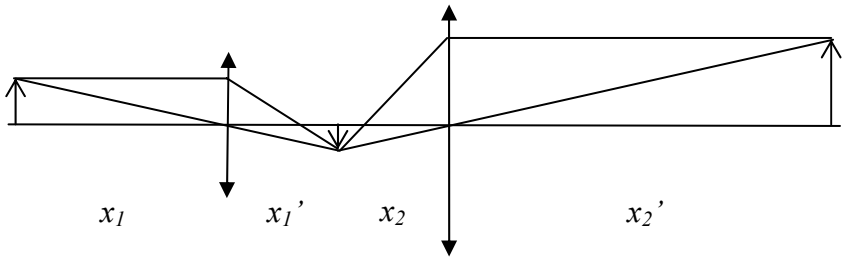

Figure 3.15 Paraxial optical layout of a generalized magnifying system with an overall magnification of $M > 1$.

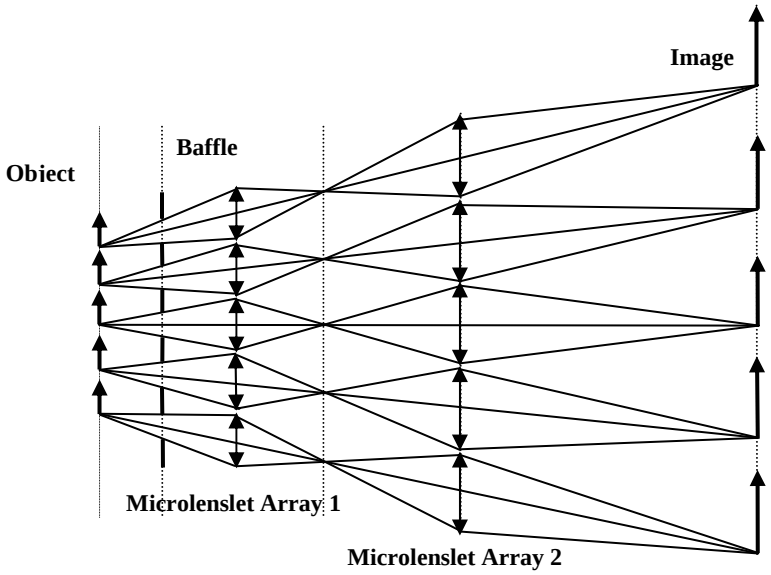

Figure 3.16 Optical layouts of 1:M imaging with a stack of two arrays of microlenses.

Provided that the microlenses in the first and the second arrays are of focal length f_1 and f_2 respectively, the object distance from the object to the first lens (L_1) is x_1, the image distance from L_1 to the intermediate real image is x_1', the object distance from the intermediate real image to the second lens (L_2) is x_2, and the image distance from L_2 is x_2', the overall length of such system defined as the distance from the object to the final image plane is given by

$$OAL = \left(x_1 + x_1' + x_2 + x_2'\right) . \tag{3.9}$$

For simplicity we assumed the absolute value of all quantities (i.e. x_1' denotes $\left|x_1'\right|$, etc.) Let's further assume that the first and the second microlenslet arrays operate at magnification of magnitudes m_1 and m_2, respectively. The magnitude of the overall magnification M of the system is defined as

$$M = m_1 m_2 , \tag{3.10}$$

where m_1 and m_2 are given by

$$m_1 = \frac{x_1'}{x_1} \quad \text{and} \quad m_2 = \frac{x_2'}{x_2}, \tag{3.11}$$

respectively. The relationships describing the optical relationships between x_1, x_1', x_2, x_2', f_1 and f_2 are given by Descartes equations

$$\frac{1}{x_1} + \frac{1}{x_1'} = \frac{1}{f_1'} \quad \text{and} \quad \frac{1}{x_2} + \frac{1}{x_2'} = \frac{1}{f_2'} , \tag{3.12}$$

where we assumed both microlenslet arrays are immersed in air (i.e. the index of refraction on both sides of each individual lenslet is equal to 1). Substituting Eq. (3.11) in Eq. (3.10) for the OAL we obtain

$$OAL = \left(x_1 + x_1' + x_2 + x_2'\right) = x_1 + m_1 x_1 + x_2 + m_2 x_2 = x_1\left(1 + m_1\right) + x_2\left(1 + m_2\right) \quad (3.13)$$

Furthermore, substituting Eq. (3.11) in Eq. (3.12) we obtain

$$\frac{m_1 + 1}{m_1 x_1} = \frac{1}{f_1'} \quad \text{and} \quad \frac{m_2 + 1}{m_2 x_2} = \frac{1}{f_2'} \quad (3.14)$$

which further solves for x_1 and x_2

$$x_1 = \frac{1 + m_1}{m_1} f_1' \quad \text{and} \quad x_2 = \frac{1 + m_2}{m_2} f_2' . \quad (3.15)$$

Substituting Eq. (3.15) in Eq. (3.13) we obtain for OAL

$$OAL = \frac{\left(1 + m_1\right)^2}{m_1} f_1' + \frac{\left(1 + m_2\right)^2}{m_2} f_2' . \quad (3.16)$$

Thus, the OAL of a magnifying optical system based on a stack of two dissimilar microlenslet arrays is described by a 4-dimensional function in the $\{m_1; m_2; f_1'; f_2'\}$ space. Various 3-dimensional slices of the 4-dimensional function describing the OAL may be considered, however since the magnification is the driving factor for our research, 3-dimensional slices with respect to m_1, or alternatively m_2, are of particular interest. Furthermore, the minimum of the function given by Eq. (3.16) after substituting without loss of generality for m_2 using Eq. (3.10) yields the most compact configuration of the two microlenslet arrays and is given by

$$\frac{\partial OAL}{\partial m_1} = 0 , \quad (3.17)$$

which yields

$$\frac{\partial OAL}{\partial m_1} = \frac{2m_1 f_1'(1+m_1) - f_1'(1+m_1)^2}{m_1^2} + \frac{2m_1 M f_2'(m_1+M) - M f_2'(m_1+M)^2}{m_1^2 M^2}$$

$$= f_1' \frac{(m_1^2 - 1)}{m_1^2} + f_2' \frac{(m_1^2 - M^2)}{m_1 M} = 0. \qquad (3.18)$$

Further simplification of Eq. (3.18) yields

$$m_1 f_2'(m_2 - 1)(m_2 + 1) = m_2 f_1'(m_1 - 1)(m_2 + 1). \qquad (3.19)$$

Thus, in the most general case the most compact arrangement (i.e. the minimum OAL) of a magnifying optical system based on a stack of two dissimilar microlenslet arrays is described by a 4-dimensional surface in the $\{m_1; m_2; f_1'; f_2'\}$ space. One of the solutions to Eq. (3.19) occurs at $m_1 = m_2 = M = 1$, which simplifies the system to the microlenslet-arrays based 1:1 relay system with an OAL

$$OAL = 4f_1' + 4f_2'. \qquad (3.20)$$

Given that for a 1:1 relay system $f_1' = f_2'$, Eq. (3.20) further simplifies to

$$OAL = 4f_1' + 4f_1' = 8f_1', \qquad (3.21)$$

which describes a *2f* configuration for 1:1 relay system. Previously in Section 3.3.1 we discussed that the most compact solution for a 1:1 optical relay system is the *2f* configuration, however it is seen from Eq. (3.21) that the 1:1 relay system with a 2f configuration is a global minimum of the generalized function describing the OAL of an optical system of any positive or negative magnification.

Furthermore, for a desired M (i.e. if M is given), Eq. (3.19) may be solved for m_1 to minimize OAL. In this case, it can be shown that

$$m_1 = \left[\frac{Mf_1 + M^2 f_2}{Mf_1 + f_2} \right]^{1/2} . \qquad (3.22)$$

Furthermore in all cases (i.e. $\forall$ M), to best eliminate ghost images in the final image plane, the intermediary sub-images after the first microlenslet array must not overlap in order to enable placement of a baffle at the entrance pupil of the system. Such condition naturally requires $m_1<1$. Without loss of generality, let $f_2 = \gamma f_1$. Then Eq. (3.22) that sets the minimum OAL, combined with the requirement of $m_1<1$, leads to a system with an overall demagnification (i.e. $M < 1$). Thus, for an $M >1$, a configuration can be established, but it will not correspond to the minimum OAL. It should be noted, however, that the most compact arrangement may not correspond to optimal first-order image quality, as previously also found in the 1:1 relay system. Specifically, first-order image quality is also highly dependent on image lensletization. Overcoming this effect was discussed in detail in Section 3.3.2 and requires overlapping the individual sub-fields of view of each individual pair of lenses at the expense of an increase in OAL and a natural decrease in resolution. [Shaoulov, Rolland, 2003]

3.3.7 Modelling the Imaging Properties of the Generalized Magnifying System with Greyscale Light Sources

To validate the feasibility of the conceived 1:2 imaging system, an F/5-500μm focal length microlenslet array was selected in the front location without loss of generality, and an F/8.3-1000μm was selected in the back location. Furthermore, the microlenses in each array were square plano-convex lenses with a thickness of 150μm. The microlenslet arrays operate at m_1 equal 0.5 and m_2 equal 4, respectively. In such configuration, it can be shown from basic principles that the second lenslet in each pair is the aperture stop of the system and therefore the baffle has to be placed in the location of the entrance pupil, which is conjugate of the aperture stop. Furthermore, the baffle must be established for the correct magnification of the pupils. In the case investigated, a set of micro-baffles with computed diameter of 40μm was placed at the appropriate location in the system.

A software model for imaging assessment was developed using custom developed software based on ASAP^{TM}. The optical layout of the system made of 11 by 11 microlenses in each array is shown in Fig.3.17. An analysis of the minimum amount of rays satisfying 99% accuracy of the raytraced image was performed using the same methodology as described in Section 3.3.3.1, and we found that the minimum number of rays needed was 2.5 billion. With the current state of the hardware and software technology such accuracy will require over 3 weeks of computational time. Based on the accuracy of the raytrace analysis shown in Fig. 3.18, an accuracy of 97% was selected for image quality feasibility because it satisfies the

criterion of about 48 hours computational time on a 2.8 GHz PC as well as the criteria of more than 95% accuracy commonly accepted as a threshold for assessing feasibility. [Cassarly, 2003]

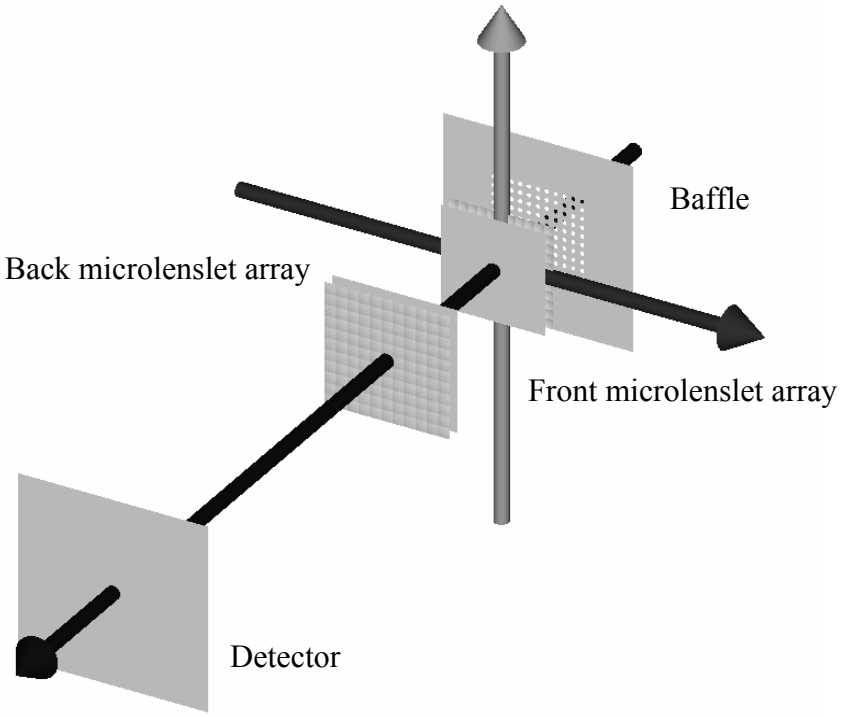

Figure 3.17 ASAP™ layout of 1:2 microlenslet arrays based magnifying system with two 11 by 11 arrays of microlenses and the appropriate baffle. From right to left, the baffle, the two dissimilar microlenslet arrays made of square plano-convex lenses, and the detector upon which an image will be formed given an object in front of the baffle, are shown.

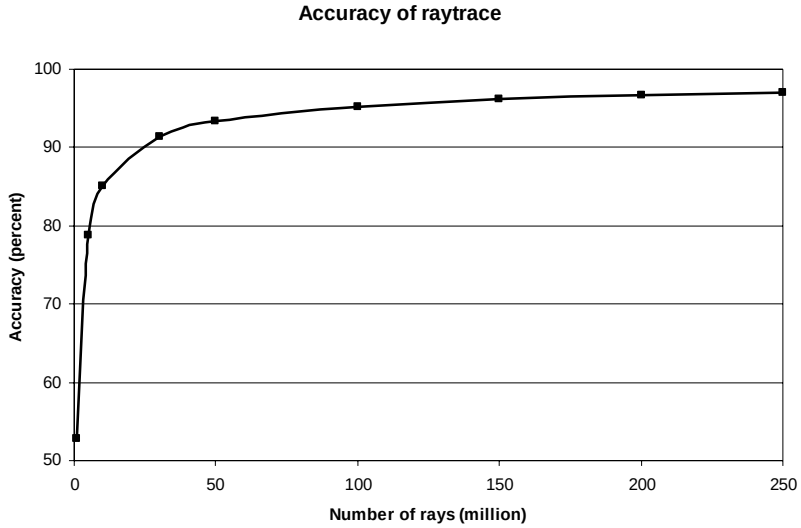

Figure 3.18 Accuracy of the raytrace in percents as a function of the number of rays emitted from the object.

Results of the simulation shown in Fig. 3.19 first demonstrate that a 1:2 relay lens based on a stack of two dissimilar microlenslet arrays can be achieved with no ghost images, yet a small residual lensletization of the image may be observed. Such lensletization would be overcome in a final, application-optimized configuration, by further overlapping the sub-FOVs. With commercially available microlenslet arrays, such system would have an overall length of 8.7 mm and weight of about 1 gram. An analysis of the image quality of the system shows that the diffraction limited point spread function is 41.67μm. Such spot size is large compared to the 10μm pixel size found in most commonly available CCD cameras. A smaller pixel size of 10μm may be achieved by increasing the apertures of the microlenslets in both arrays to 410μm in the front and 500μm in the back, respectively. However, increasing the apertures of microlenslets while keeping their focal length invariant naturally occurs at the expense of decreasing the working F-number. Such decrease leads to a more complex performance-

optimization task, yet it does not compromise the feasibility of the design. In this case, the OAL is still compact and about 9.5mm. Such resolution requires simulations with more pixels to cover an equivalent FOV, thus less rays per pixel leading to a raytrace accuracy of about 85% based on the same criterion of about 48 hours computational time on a 2.8 GHz PC . The results obtained for that system were consistent with the results obtained with the 97% accuracy, confirming the feasibility of the system. This simple analysis however points to the reason we originally chose microlenslets of smaller diameter so we can run simulations at higher accuracy with the intrinsic understanding that diffraction is limiting and can be reduced with larger size microlenslets.

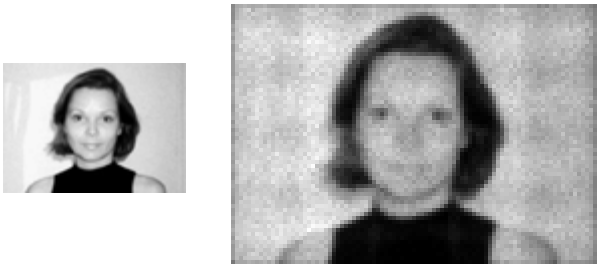

(a) (b)

Figure 3.19 Imaging of grayscale object through 1:2 microlenslet array based magnifying system: (a) object and (b) magnified image.

If the system is made of simple plano-convex lenses, as considered for the feasibility investigation, both monochromatic and chromatic aberrations will be limiting the image quality. However, because the sine condition is quasi-satisfied (i.e. <0.02% discrepancy), if the lenslets located in the sub-pupils are aspherized so there is no spherical aberration, then coma will also be negligible. Furthermore, per MTF analysis, astigmatism is currently

limiting the image quality and may be corrected by aspherization of the lenslets in the first array, which is the entrance window. Distortion for any pair of lenslet is non-negligible and requires further investigation in how it practically affects image quality. Finally, given that simple plano-convex lenslets were used, the system will suffer both axial and transverse chromatic aberrations. An analysis shows that axial chromatism is significant and will need to be corrected using a lenslet doublet in the pupil. Lateral color, however, is less than 5μm at the edge of the field of view, thus will most likely not require any further minimization. However, if an application required no lateral color, another lenslet doublet located in the entrance window could be used.

3.4 Discussion and Future Work

While relaying and magnifying images using compact multi-aperture based optical systems can only be done at the expense of resolution, such technology offers new solutions for applications where resolution is not a stringent requirement. Such relay and magnifying systems may find further application in the improved design of head-mounted displays.[Shaoulov, Martins, Rolland, 2004], [Martins, Shaoulov, Rolland, 2004] Specifically, in the case of relaying and magnifying images in head-mounted displays, slight loss in resolution can help depixelization of the micro-display generating the images. Thus, this is a case where a slight loss in the resolution actually benefits the system. In the case of optically created special effects, the images created are highly distorted and blurred by optical phase plates inserted out of focus within the relay optics in order to generate images modified with special effects as demonstrated in Fig. 3.2. [Shaoulov, Rolland, 2001] In such

imaging framework, resolution is not a key qualifier of image quality, but artifacts such as lensletization must be avoided.

Future work on the relay systems will further expand the research to investigate how stacks of microlenslet arrays may be optimized to satisfy various image quality criteria from the *5f* to the *7f* configurations, in which lensletization was shown to be negligible. Aspherization of the singlets may be used in a more advanced configuration to minimize spherical and astigmatic aberrations, two main limiting monochromatic Seidel aberrations. Also, whether it is possible to design better systems by stacking more than two microlenslet arrays is a question of investigation. Trade-offs of image quality and cost of alignment must be evaluated across specific application requirements. Axial color can be corrected by using doublet-lenslets within each stack. Such improvement requires a new fabrication process, which is under investigation in our laboratory. In this investigation, we will need to draw a sufficient number of rays to ensure that the simulations are not limited by the Poisson noise imposed by raytracing a finite number of rays. Under low noise conditions, the impact of optical aberrations and diffraction are clearly quantifiable.

Furthermore, a comprehensive modeling of the rigorous theoretical framework set by Eqs. (3.9) to (3.18) may be used to design the most compact task-driven optical solution for various problems, which will allow the replacement of bulk macro-optical systems with ultra compact multi-aperture micro-optical systems, wherever possible. That could lead to significant gain in compactness, weight and cost-effectiveness in many areas currently utilizing bulk macro-optics.

Finally, working prototypes will be fabricated in future application driven cases to further demonstrate the imaging capabilities of multi-aperture micro-optics.

CHAPTER 4: EXPERIMENTAL METHODS AND RAYTRACING AS AN IMAGING PROCESS

Based on the methods discussed in Chapters 1, 2 and 3, images with optically encoded special effects, such as effects resembling art forms, can be formed using optical phase plates. The experimental foundation of this work is discussed in this Chapter, as well as custom developed optics and software to assess and quantify the proposed methods. Results captured with custom-designed cameras as well as software simulations are presented to demonstrate and verify the feasibility of the proposed approach.

4.1 Experimental Assessment of Optically Creating Special Effects

4.1.1 Experimental Setup

Conceptually the experimental setup uses a standard objective lens to form an aerial image in some intermediate image plane, then modifies the aerial image in this plane by using an optical phase plate inserted in, or around this intermediate plane, and finally optically relays the modified image on an image-capturing device (e.g. film or CCD) where the final image is recorded. A conceptual design of the experimental setup utilized to assess the feasibility of the concept is demonstrated in Fig. 4.1.

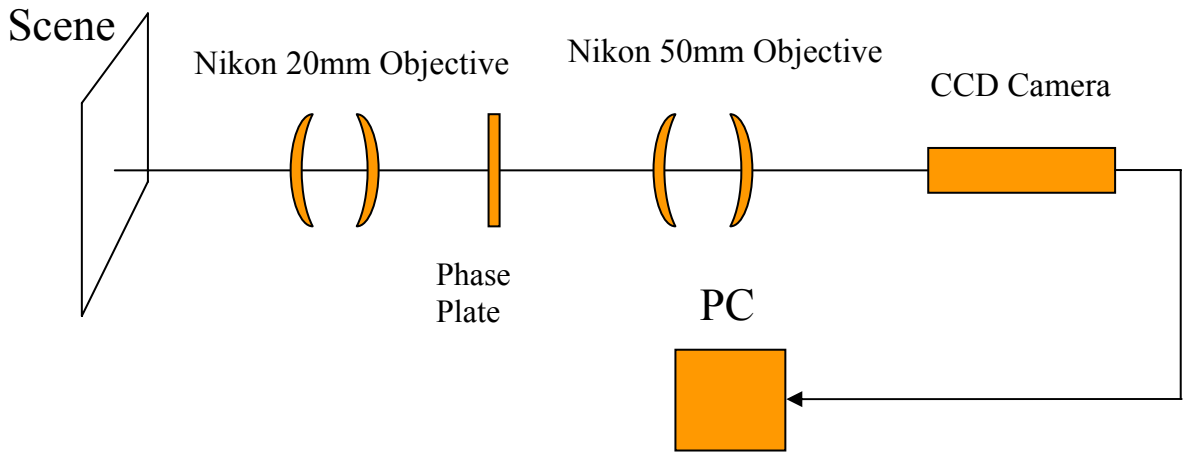

Figure 4.1 Layout of the bench optical system used to assess imaging through optical phase plates.

Following the conceived conceptual design, an actual experimental setup was built consisting of a standard 20mm focal length Nikon objective mounted on a translational stage, used to form the intermediate image from a 3D scene (e.g. a still life, a portrait, etc.) located in front of the objective. The location of the image produced by this objective (i.e. the intermediate image of the conceived system) was first measured experimentally for the selected scene location. The distance from the scene to the objective (i.e. approximately the object distance of the objective, the exact object distance being measured from the principal plane object of the lens to the object location) was selected such that the scene itself remained within the depth of field of the objective lens for the desired F/# (i.e. ~F/7 for example). Thus, in the final setup the effects of defocus would be only caused by the controlled defocus of either the objective lens or the relay optics. The optical phase plates, which may be mathematically synthesized, [Rolland, Strickland, 1997] [Rolland, et.al., 1998] are micro fabricated using

laser etching technology, which will be briefly discussed in Section 4.1.3. In our experiments, the optical phase plates were located on a separate translation stage allowing for defocusing the optical phase plate with respect to the aerial intermediate image produced by the objective, as well as allowing moving the phase plate in the lateral plane (i.e. along the axis perpendicular to the optical axis). The intermediate image itself could be defocused as well, using the controls of the objective. A second 50mm Nikon objective (AF Nikkor 50mm f/1.8) was set as a 1:1 imaging system allowing relaying the intermediary image to the final image plane where a color CCD camera connected to a PC controlling the experiment was located. A He-Ne laser was used to identify the optical axis of the front objective and to align the relay objective to the same optical axis. [Shaoulov, Rolland, et. al., 2001] A photograph demonstrating the actual setup built is shown in Fig. 4.2.

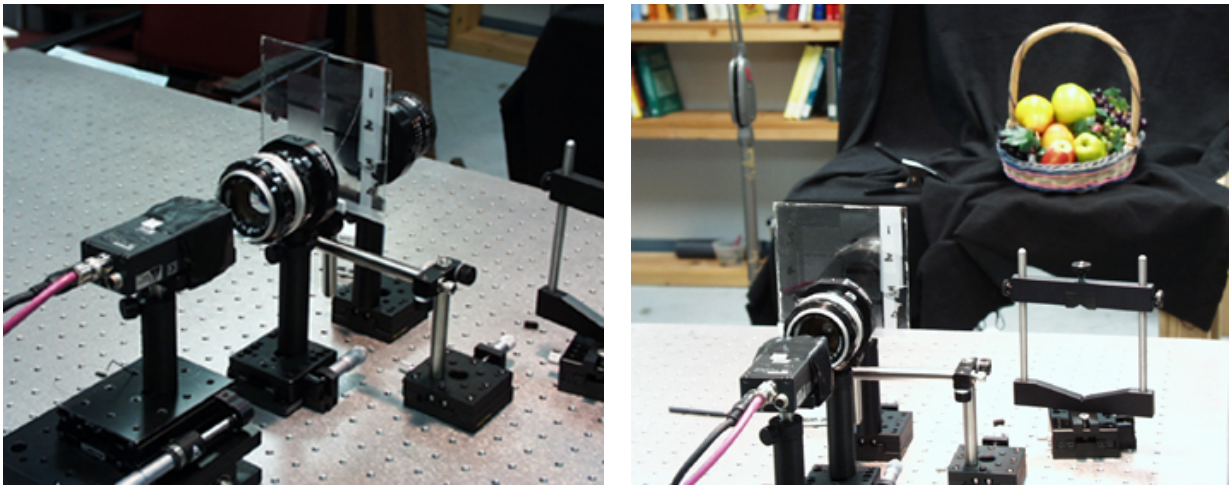

Figure 4.2 Bench optical setup in the testing of imaging though optical phase plates.

Utilizing the experimental setup, various final images as a function of the location of the optical phase plate and the defocus of the intermediary image were observed and recorded.

One set of such images, as a function of various defocus of the intermediate image plane and the optical phase plate used is demonstrated in Fig. 4.3. Since there is no figure of merit suitable to evaluate the degree to which the modified images resembled actual art forms, the selection was based on subjective perception. It was qualitatively established that the best results were obtained when the optical phase plate and the intermediary image were both about 5mm out of focus. However, the experimental setup was rather inconvenient to work with because it was bulky and was fixed to the optical table. Furthermore the image was not directly seen by the human eye (i.e. as in an actual camera, where the image is previewed in the viewfinder). Consequently the fixed setup led to difficulties in illuminating the scene and manipulating dynamically the defocus of the optical phase plate and the objective, while not allowing enough flexibility for the experimental measurements. Thus, a new design for the relay optics compatible with a standard Nikon objective and standard Nikon camera body was sought and conceived as a next step, as detailed in section 4.1.2.

Figure 4.3 Images obtained on the bench setup with: (a) 5mm defocus of the optical phase plate with respect to the intermediate image plane; (b) same as in (a) with some additional defocus introduced by the front objective; (c) closeup view of the scene with the same amount of defocus as in (b); (d) another closeup view of the scene with the same amount of defocus as in (b).

4.1.2 Relay Lens Prototype

After achieving the conceptual design of the relay optics, the actual design was finalized in collaboration with Optical Research Associates Corporation. There were two important conceptual ideas that determined the final design.

First, in order to make the design as compact as possible, a field lens was set close to the last optical element of the standard 20mm Nikon objective. Consequently the size of the intermediate image decreased by a factor of 2. Therefore, a modified 1:2 double Gauss lens was used to relay the intermediate image to the final image location, as discussed previously in Chapter 3. The final image was relayed with a clearance of 40mm from the last optical surface in order to account for the required clearance imposed by the standard body of the Nikon camera. To ensure the compatibility between the designed compact relay optics and the standard camera body, we performed measurements of the back focal length (BFL) of three standard Nikon objectives, a 50mm standard Nikon Lens used as the relay optics in the experimental setup, a 20mm standard Nikon Lens used as the objective lens in the experimental setup, and a 35mm standard Nikon Lens used as a control point in our measurements (i.e. since all standard Nikon Lens must be compatible with the standard Nikon camera body, all the measured BFLs must be the same within the measurements' error). To perform the necessary measurements of the BFL of the three standard Nikon objectives, the Nodal Slide Method was used. [Malacara, 1978] [Harvey, 2004]

The Nodal Slide Method, which gives accurate experimental results, involves a few steps as further detailed. The experimental setup is demonstrated in Fig. 4.4. [Harvey, 2004] First, we set the front nodal point of the objective under investigation on the axis of rotation of the rotational stage used to mount the objective to the bench. Then we moved the microscope carrier to focus the vertex of the test lens on the image plane. Then the Nodal Slide was rotated and the fine scale of the test lens carrier was adjusted until the image was stationary, which indicated that the lens was set to operate at its Nodal points.. Then the Nodal Slide was refocused and reading *A*, locating the back focal point of the test lens, was recorded. Further, the Nodal Slide carriage was moved until the rear surface of the test lens came in focus. Reading *B* was recorded as the new position of the Nodal Slide carriage. The difference between *A* and *B* determined the back focal length of the lens under investigation, as measured from the vertex of the lens to the focal point of the lens. Furthermore, to determine the location of the back principal plane the readings from the fine scale of the test lens carriage were recorded in positions *A* and *B*, denoted as *a* and *b*, respectively. The difference between *a* and *b* determined the location of the principal plane with respect to the measured vertex of the investigated lens. Thus, the effective focal length of the lens was measured and compared with the manufacturer specification, allowing assessing the experimental error. Results of the experimental measurements are summarized in Table 4.1. The experimental results demonstrated that a clearance of ~40mm for the relay optics would be sufficient to ensure compatibility with any standard Nikon objective, and thus with any standard Nikon camera body as well.

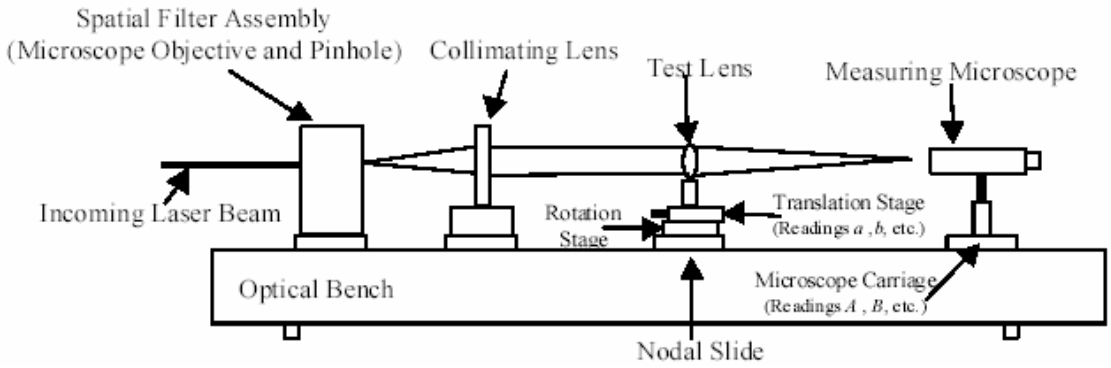

Figure 4.4 Nodal slide method used to measure the BFL of the lens under test. (Courtesy of J. Harvey and A. Krywonos)

Table 4.1. Measurements of three Nikon photographic lenses

	50mm standard Nikon lens	20mm standard Nikon lens	35mm standard Nikon lens
A(average), cm	21.35	21.61	22.58
σ_A, cm	0.04	0.05	0.05
B(average), cm	25.12	25.47	26.41
σ_B, cm	0.05	0.06	0.06
a(average), mm	6.12	16.92	3.71
σ_a, mm	0.1	0.3	0.1
b(average), mm	19.61	-0.5	1.63
σ_b, mm	0.3	0.05	0.1
BFL(average), mm	37.70	38.60	38.30
δ' (average), mm	13.49	-17.42	-2.08
f'(average), mm	51.19	21.18	36.22
Error, %	2.38	5.9	3.49

The second important conceptual idea was to relay the exit pupil of the standard objective through the relay system, thus minimizing vignetting. Various measurements of the exact location of the exit pupil for a standard AF Nikkor 50mm f/1.8 objective were thus performed. For the exit pupil experimental measurements we used similar experimental setup to the one used to measure the BFL of the Nikon objective. Results for the exit pupil

measurements demonstrated that it is located at a distance of 15mm away from the last surface of the lens.

Finally, the field curvature of the standard AF Nikkor 50mm f/1.8 was measured, allowing us to constraint the field curvature of the objective-relay assembly optics to be equal or less than the measured value for the objective lens. For the field curvature experimental measurements, we used a setup similar to the one presented in Fig. 4.4 consisting of a collimated He-Ne Laser beam, a polarizer to reduce the intensity of the beam, a test Nikon f50/1.8 AF Nikkor Lens operating at a low F/# (i.e. F/22), and a measuring microscope, placed on a transnational stage. First we cleaned and collimated the laser beam using a pinhole and a microscope objective assembly to obtain a collimated beam.. Furthermore, we set the test Nikon f50/1.8 AF Nikkor Lens to work at its nodal points. Thus, the focal point of the Nikon lens was always along the optical axis and we were able to directly measure the field curvature as the departure of the measured best focus from the paraxial focal plane. We expected the field curvature, denoted as W_{220} to be parabolic, according to the theory. [Slyusarev, 1984] Then we performed our measurements by scanning the location of the focal point and looking for the minimum of the so-formed curve as a function of the lens tilt with respect to the optical axis. By scanning with a step of 1 degree, we found the desired minimum. Thus, the orientation normal to the laser beam (i.e. the location defining the paraxial focal point) was provided for the Nikon f50/1.8 AF Nikkor Lens under investigation. Furthermore, we re-calibrated our setup by setting the measured location defining the orientation of the test lens normal to the optical axis to correspond to 0 degrees tilt on the rotational stage, and then we scanned trough the working FOV, calculated to be 25 degrees

for a standard 35mm film (i.e. 24 by 36mm film format). The results of the experimental measurements are presented in Table 4.2 and a quadratic fit for the field curvature, measured as the departure of the best focal point from the paraxial focal plane, in mm, against the normalized field angle, is demonstrated in Fig. 4.5. The bars at each point represent the standard deviation of each measurement.

Table 4.2. Measurements of field curvature for standard 50mm Nikon objective.

Field Angle θ, degrees	*Cosine of the Field Angle θ*	*Measured Value of the Best Focus Departure from the Paraxial Focal Plane, mm*	*Standard deviation, mm*
26	0.899	5.391	0.018
21	0.934	3.378	0.014
16	0.961	1.878	0.011
11	0.982	0.895	0.013
6	0.995	0.329	0.004
5	0.996	0.319	0.306
4	0.998	0.132	0.019
3	0.999	0.096	0.015
2	0.999	0.049	0.039
1	0.1000	-0.016	0.027
0	1	0	0.022
-1	0.1000	0.006	0.024
-2	0.999	-0.012	0.006
-3	0.999	0.054	0.036
-4	0.998	0.093	0.01
-5	0.996	0.119	0.009
-6	0.995	0.167	0.016
-9	0.988	0.541	0.066
-14	0.970	1.285	0.011
-19	0.946	2.632	0.019
-24	0.914	4.780	0.068
-26	0.899	5.321	0.052

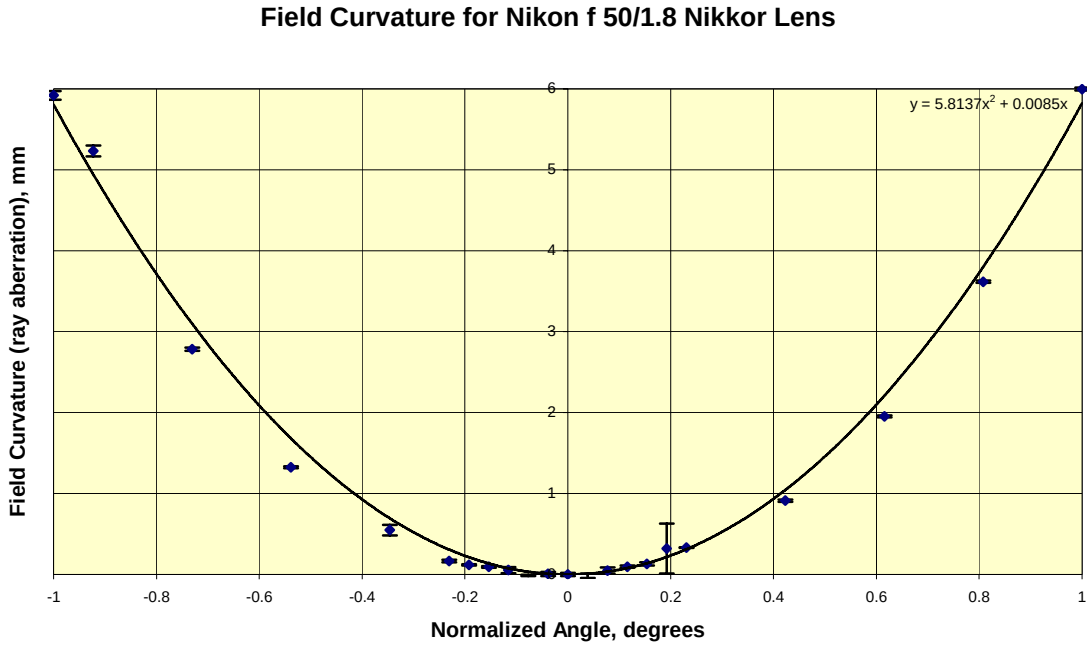

Figure 4.5 Measurement of the field curvature of a standard Nikon 50mm Nikon lens and a quadratic fit of the data, representing the field curvature.

Thus, the specifications for the relay system were fully determined and summarized in Table 4.3. The MTF performance of the optimized relay system was previously presented in Chapter 3, Fig. 3.4 and showed that it holds well over the entire field of view. [Shaoulov, Rolland, et. al., 2001] In addition, the field curvature of the achieved relay system is within the constraint imposed by the measured field curvature for the standard Nikon objective. Thus, we achieved a final design satisfying all the constraints imposed by our application and ensuring maximum compactness within the paradigm of bulk macro-optical systems. However, much more compact solutions can be provided with the novel paradigm of imaging with multi-aperture micro-optics, as discussed in Chapters 3 and 6.

Table 4.3. Specification for the design of a compact relay lens to create optical special effects by utilizing optical phase plates.

Parameter	Specification	Achieved
Detector	Standard 35mm film	Compatible
Field of view	Determined by the film size	52 degrees
F/number	From F/1.8 to F/22	F/1.8-F/22
Magnification	2	2
Effective focal length	Determined by the clearance to the film	40mm
Spectral range	From 400nm to 750nm	400nm-750m
Image quality	MTF greater than 20% at 20lp/mm	20%
Vignetting	Pupil matching that minimizes vignetting	0% vignetting
Overall length	Less than 100mm	85mm
Prototype cost	Less than $15,000	$7,500

Based on the final design of the relay system a prototype was built by Coastal Optics Co., which is shown in Fig. 4.6. Using the prototype of the relay system together with a standard Nikon f50/1.8 AF Nikkor Lens and a standard Nikon camera body, results with various previously fabricated optical phase plates and amount of defocus were obtained. One such set of results, courtesy of Steve Hylen, is demonstrated in Fig. 4.7. However, the selection of optical phase plates creating various special effects at this point was based on a trial-and-error method. Thus, the need of software predicting the visual appearance of an image modified with a given optical phase plate used within the designed hardware became apparent in order to design and fabricate optimized plates targeted at specific special effects.

Figure 4.6 Compact relay lens prototype.

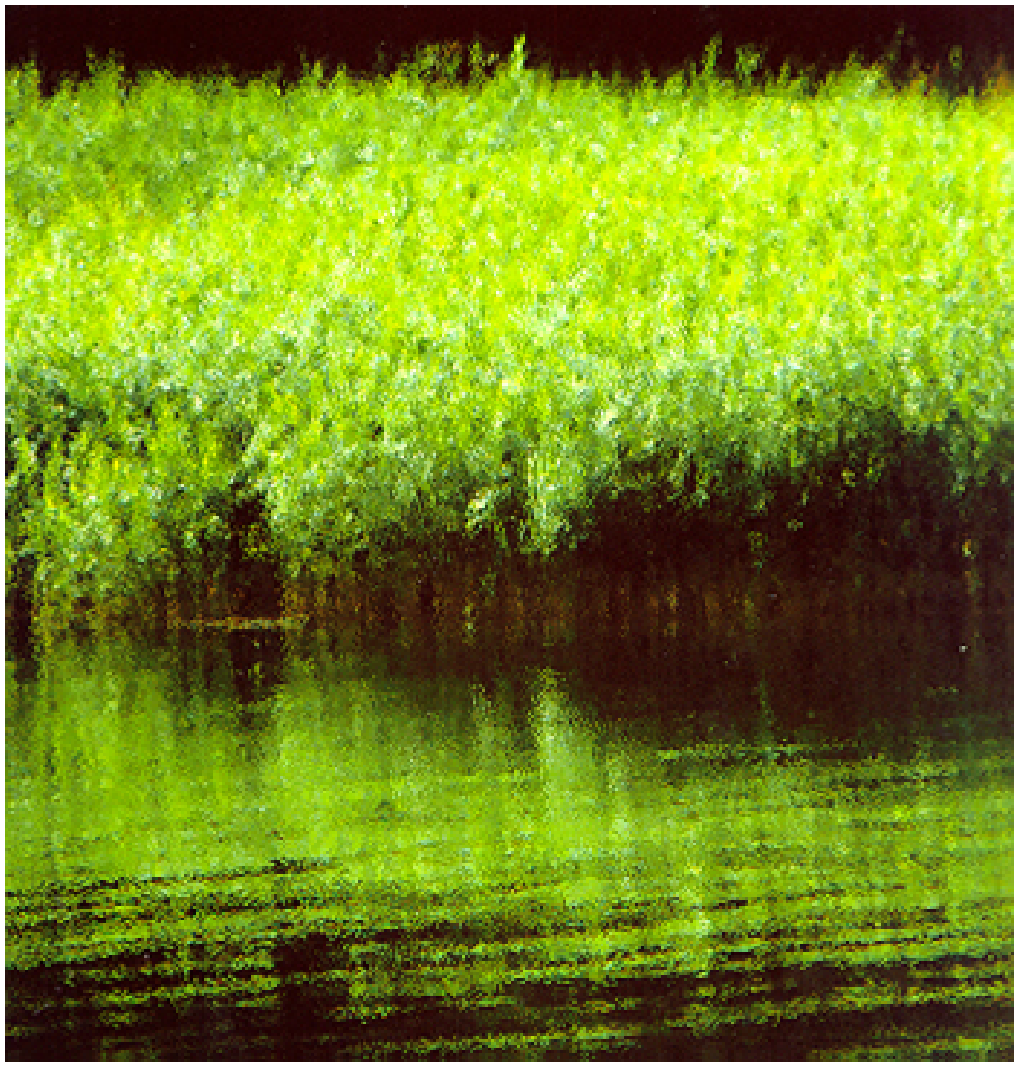

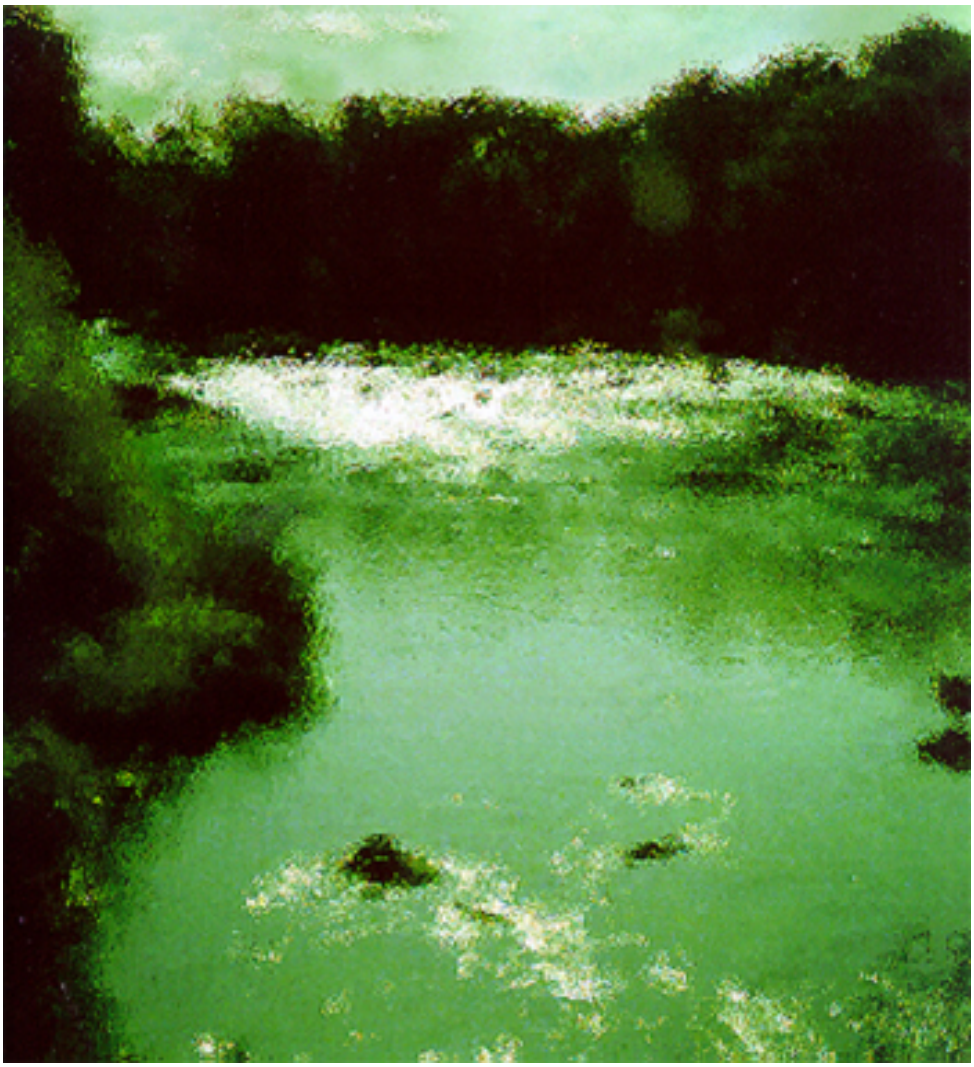

Figure 4.7 Images of special effects obtained with the prototype relay lens shown in Fig. 4.6 and proprietary phase plates. (Courtesy of Steve Hylen).

4.1.3 Fabrication of the Optical Phase Plates.

The optical phase plates discussed in this research are optical surfaces created out of a bitmap, each gray level of which corresponds to certain height etched in an optically transparent material (e.g. epoxy), placed on top of a glass substrate. A typical bitmap used to

generate an optical phase plate consists of 6000 by 4000 pixels, which are mapped on a glass plate of 0.5mm substrate thickness with an 18 by 12 millimeters transversal size of and optical surface height distribution of 25 micrometers. The desired size of the optical phase plate is determined by the intermediate image size in the designed relay optics (i.e. ½ the standard 35mm film format). The size of the bitmap, in pixels, was selected to maintain the desired aspect ratio of 1.5, determined again by the standard 35mm film format. Thus, each bitmap pixel is mapped onto a 4.8 by 4.8 micrometers area on the glass plate while the optical surface height distribution varies anywhere between 0 and 25 micrometers. The features on the glass surface are etched using a proprietary dry laser etching technology implemented by Rochester Photonics (currently subdivision of the Corning Inc.), as conceptually demonstrated in Fig. 4.8, courtesy of Joe Burkenburg. Four of our typical optical phase plates are shown in Fig 4.9. The properties of the fabricated optical phase plates were further verified utilizing a Zygo interferometric microscope and found to be within the fabrication specifications, as demonstrated in Fig. 4.10.

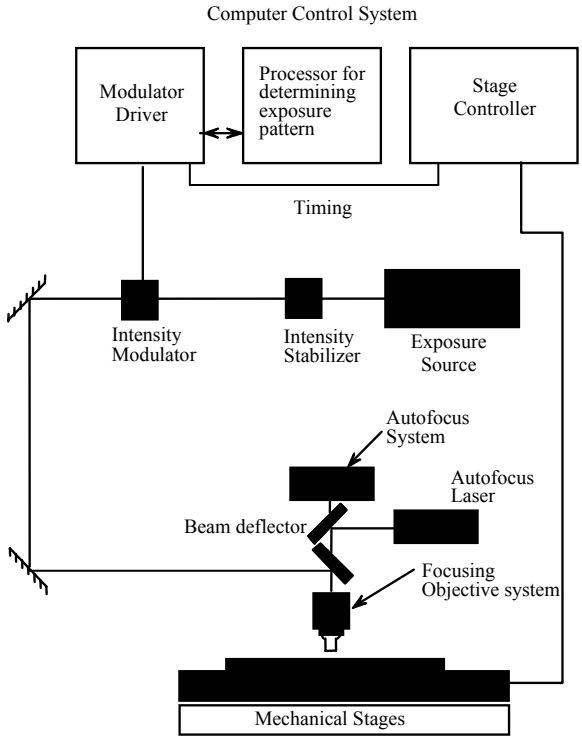

Figure 4.8 Dry laser etching instrument utilized in the fabrication of optical phase plates.

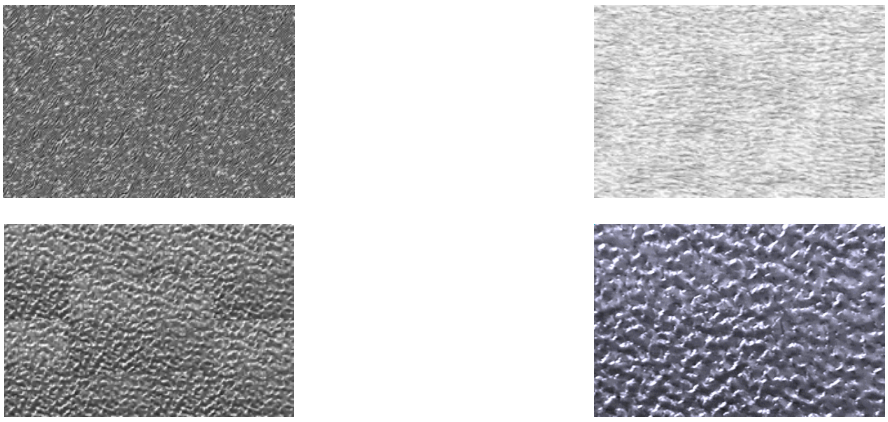

Figure 4.9 Four optical phase plates fabricated through the dry laser etching process.

The major problem of this fabrication technology is the cost effectiveness (i.e. 4K for one master plate). Making the master optical phase plate is an expensive process, which rules out the trial-and-error method of creating optical phase plates for each desired special effect, further justifying the need of software enabling the correct modeling of the imaging process through such complex optical systems.

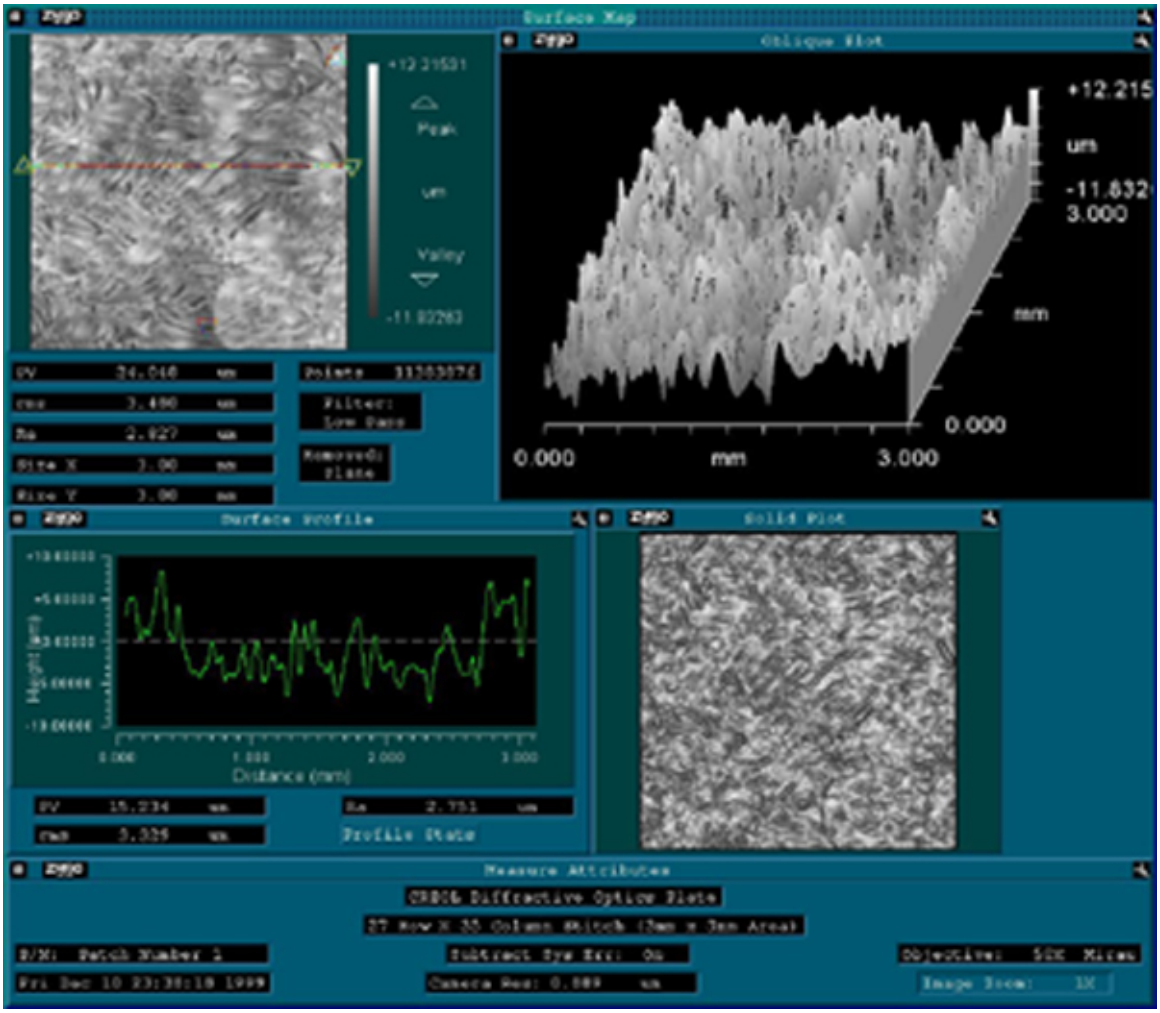

Figure 4.10 Interferometric measurements of the optical phase plates.

4.2 Software Modelling of the Imaging Process within the Raytracing Paradigm

4.2.1 Raytracing in the Theoretical Framework of the Vectorial Law of Refraction

Geometrical optics is a part of optics involving phenomena that can be discussed within the framework of Fermat's principle, from which laws of reflection, refraction and propagation can be derived. [e.g. Marechal, 1952] Let's define the optical length of the light path as the integral

$$OPL = \int_S n ds \,, \tag{4.1}$$

where *ds* is an element of the arc length of the light path and *n* is the index of refraction along the ray. Assuming two points in an isotropic medium, Fermat principle states that the optical path that the light actually takes is the extremum of all possible optical paths between these two points. It reduces to a minimum for points in the regular neighborhood, which is the region in space where one, and only one, light path passes through each point. This region is limited by the envelope of the light paths, known as the caustic. For light paths beyond the caustic, the optical path length is actually stationary.[Born, Wolf, 1999] Further, solely propagation in homogenous and isotropic medium where the light can be shown to propagate along paths of infinite radii of curvature (i.e. straight lines) will be assumed. Such paths provide a model for light propagation referred to as light rays. [Forbes, Alonso, 1998]

The laws of reflection and refraction are illustrated in Fig. 4.11, assuming that light is incident on the surface between two media. The point where the light intersects the surface is called the point of incidence. Typically, at any point of incidence, the normal $\vec{N}$ to the surface can be established. If a ray propagates along the direction of the normal (i.e. the case of normal incidence), a component is reflected on itself, while the other is transmitted undeviated. In the most general case, the angle subtended by the surface normal and the incident ray, known as the angle of incidence *i*, is non-zero and yields deviated reflected and refracted rays. The angle subtended by the surface normal and the reflected or refracted ray shall be denoted *i'*. Starting with Fermat's principle, a vectorial law applicable to either reflection or refraction can be derived, [Marechal, 1952] that is given by:

$$n'\vec{\mathrm{u}}' - n\,\vec{\mathrm{u}} = (n'\cos i' - n\cos i)\,\vec{\mathrm{N}}\,. \qquad (4.2)$$

The scalar law of reflection, obtained by taking *n'* = -*n*, states that the angle of reflection is numerically equal to the angle of incidence (i.e. *i'* = -*i* upon reflection). Such a convention for changing the sign of the index of refraction upon reflection allows unification of the laws of refraction and reflection. In this respect, such convention is advantageous over other possible conventions.

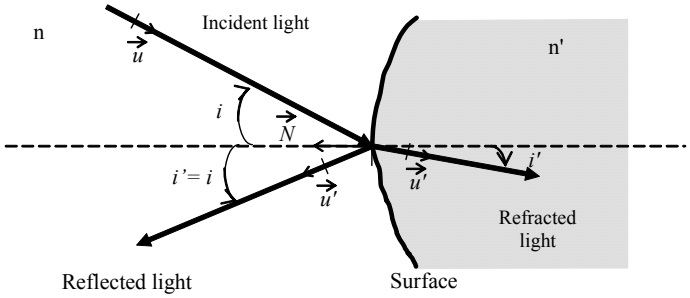

Figure 4.11 Reflection and refraction of light at the surface between two media.

A large class of optical systems consists of a series of refracting and/or reflecting surfaces providing the desired deviation of the rays of light, together with appropriate stops and apertures to limit the angular and spatial extent of the rays. An optical designer must trace the path of selected rays through the system, which is done by repeated application of the vectorial reflection and refraction laws through the system. Such process is known as real raytracing.

In the current treatment, optical systems with a common axis of revolution, referred to as the optical axis, are assumed. In the approximation of small angles of incidence on surfaces and with respect to the optical axis, the optical system is said to work in the Gauss or paraxial approximation, and raytracing under these assumptions is referred to as paraxial raytracing.

4.2.2. Modelling of the Imaging Process by Utilizing a Custom Developed Raytracing Software

The first approach that we explored to model the imaging process through an optical phase plate consisted in tracing rays from each point in object space through the entire system. Computationally, the object was considered self-luminous and a discrete version of the object was considered (i.e. the object was considered as being made of pixels). Each pixel emits rays in blue, green, and red colors (i.e. blue, green and red wavelengths) in the amount respective to the gray level value that each pixel has in the respective color. Furthermore, the rays that are emitted from each pixel of the considered object propagate in air towards the

entrance pupil of the optical system and are further transferred through it, thus forming the final image.

Upon encountering the first optical surface, the rays are refracted according to the Descartes' vectorial law of refraction as specified in Eq.4.2.[Mouroulis, Macdonald, 1997] For the imaging part through conventional optics, simple paraxial raytracing was used in the approach,[Rolland, Shaoulov, Gonzales, 2001] in order to first study the effect of the random phase plate alone.[Shaoulov, Rolland, et. al., 2001] However, as part of the future work, real raytracing through a real lens could be implemented to fully predict the imaging through a designed lens with its own optical aberrations, as further discussed in Chapter 6.

Naturally, the most challenging task is to trace rays through optical phase plates, as the ones shown in Fig. 4.9, because they are fine in structure and rapidly varying, but also deep compared to the wavelength (i.e. up to 25μm). In the raytracing approach to modeling of the imaging process, the local normal to any optical surface at the point where the ray intersects that surface is computed in the case of the lenses in the system, or estimated in the case of the optical phase plate. For the optical phase plate, it represents a challenge because the surface is not smooth compared to the wavelength and contains potential discontinuities of the normal to the surface. Therefore, notions of smooth variations of the normal orientation and computation come in play. Moreover, to model mathematically the surface, a function that approximates the surface (such that the second derivative of this function is continuous across the optical surface) is needed to be able to apply the vectorial law of refraction. This imposes some severe restrictions over the way the optical phase plates are modeled,

significantly departing from the actual optical phase plates' structure, demonstrated in Fig. 4.11. [Shaoulov, Rolland, et. al., 2001] Physical optics modeling discussed in Chapter 5, and the potential application of statistical optics combined with real raytracing discussed in Chapter 6, will further aim at removing this restrictions.

After raytracing through the optics and the plate, the final image must look like a typical image we obtained in the experimental setup. Because of the finite apertures of the lenses and the optical phase plate, the Point Spread Function (PSF) of the optical system must be considered as well. Although in the case of lenses the definition of a PSF is well established, a component of the future work lies in defining mathematically PSFs for shift-variant optical systems including those utilizing optical phase plates, and in comparing the obtained results to the measured data. The PSF accounts for the finite size of the aperture of the optical system for in-focus imaging, given that for out-of-focus imaging it can be modeled as the in-focused PSF convolved with a cylinder function, corresponding to the actual amount of defocus. Raytracing modeling in conjunction with a simple filtering final operation to account for the optical phase plate PSF led to encouraging results, yet the methods did not lead to accurate physical modeling of the optical imaging process under all imaging conditions. We achieved some good agreements between the raytracing results and the experimental results for large-scale optical phase plates. Also, we achieved a speed of computation within seconds. In addition, the raytracing approach led to the development of in-house made raytracing software. Some typical results are presented in Fig. 4.12.

Figure 4.12 Simulation of optically created special effects using raytracing combined with an optical phase plate-based filter operation.

4.2.3. Exploration of Raytracing through Texture Phase Plates using Commercially Available Software

Another part of the theoretical model and the software application developed is verifying the obtained results using benchmark software, such as ASAP^{TM}. Currently ASAP is one of the most sophisticated commercial off-the-shelf (COTS) optical modeling software available for

raytracing, and as such was a logical choice as a dependent verification tool. The software was used in conjunction with Rhinoceros, which is a stand-alone CAD modeling software.

The main limitation of ASAP ™ is the number of the optical surfaces the software is able to handle, which could not exceed 9,999. For order-of-magnitude comparison, a typical mathematically synthesized optical phase plate created of a 6000 by 4000 pixels might consist of as many as 96,000,000 surfaces. A way to work around that limitation was to create the optical phase plate surface in a CAD program using another in-house developed software, and then export the surface into ASAP ™, where a real raytrace was further performed. To utilize this method the bitmap was first imported as a cloud of points into the custom made plug-in. Furthermore, the custom developed software performed triangulation among each set of adjacent points in the cloud, thus creating a surface, as shown in Fig. 4.13. Finally, the custom designed software exported the surface either directly into an ASAP library code, or into a CAD-compatible format. A typical ASAP library exported from our custom designed software may consist of as many as 100,000 lines of code for a simple surface created out of a 100 by 100 pixel bitmap. If instead, the CAD-compatible format is selected, then the output of the custom designed software needs to be further imported in Rhinoceros, where a b-spline approximation of the surface is performed by using the adjacent points in the triangulation as control points (a proprietary procedure called “drape” in Rhinoceros). Both procedures are extremely computationally intensive, and optical phase plates generated out of a bitmap with more than a 1000 by 1000 pixels would be impossible to model on the current state of the art computer hardware.

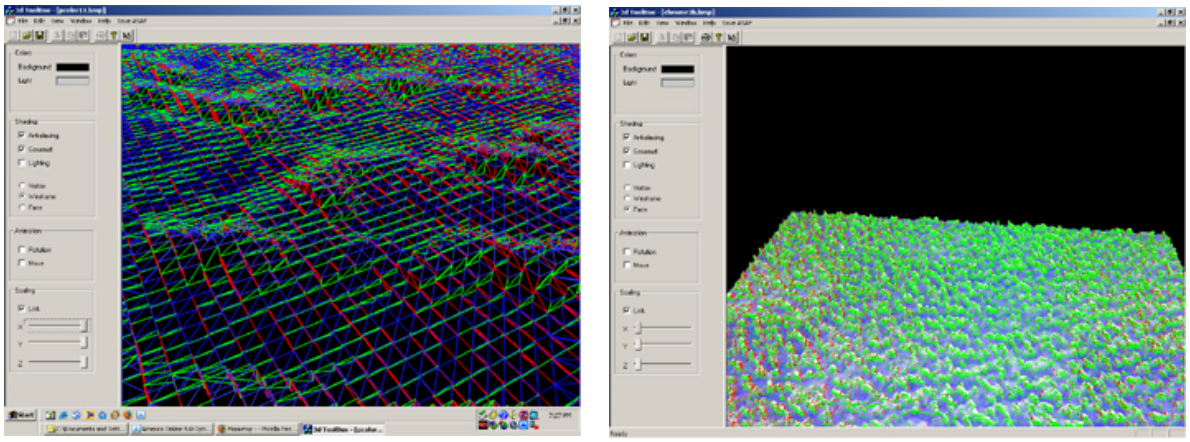

Figure 4.13 Optical texture plate created as a surface using a custom developed software module.

A typical optical phase plate made of a mathematically synthesized bitmap source of 400 by 400 pixels and rendered in ASAP^{TM} is shown in Fig. 4.14. To the authors' knowledge, a real raytrace and analysis of such complicated optical systems have never been utilized before using ASAP ^{TM}. One of our achieved results is presented in Fig. 4.15, where ¼ of the self-emitting image used as an object is covered with the optical phase plate shown in Fig. 4.14. Although this approach requires more work on the scale of the optical phase plates used, it provides a tool to verify the results previously obtained in the custom-developed raytracing model. However, the amount of time needed to model and raytrace one single optical phase plate made this approach non viable for further investigation, which led us to abandon further exploration of this approach to raytracing through phase plates.

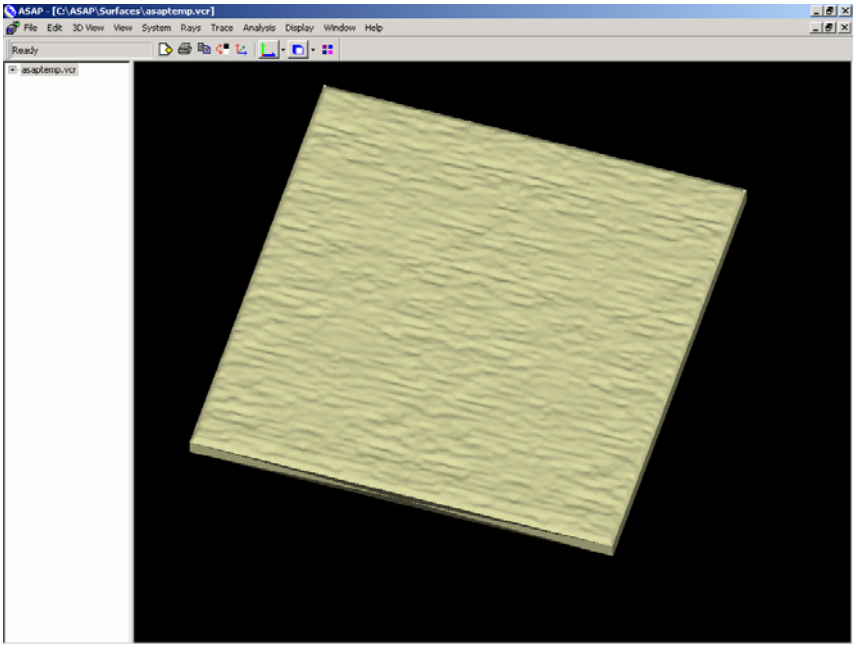

Figure 4.14 Optical phase plate modeled in ASAP.

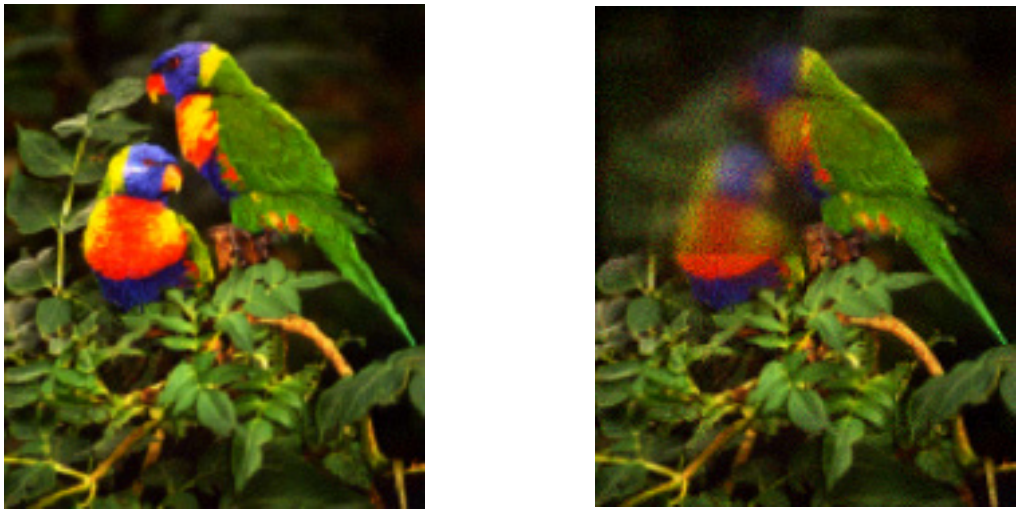

Figure 4.15 Result from the full raytrace in ASAP ™ using an optical phase plate covering the upper left ¼ of the object (right) and the original picture (left).

4.3. Discussion and Future Work

The research presented in this Chapter led to the design and the development of a novel optical system consisting of a standard 50mm Nikon objective and custom designed relay optics, allowing the photographer to create pictures resembling art forms such as painting at the speed of light. This unique application of photography allows the photographers to perform real time image processing by changing the scene and the optical wave plate used as a function of their own artistic perception. We showed how custom-developed raytracing software combined with a texture-based filtering process led to the generation of new art forms. Because of the satisfying effects and the high speed of computing we achieved, such art forms were commercialized by SmARTlens^{TM} Corporation. However, because raytracing, without the texture-based filter process, did not predict images obtained with the newly developed hardware and we had a need to be able to predict such imaging process in order to design appropriate phase plates, the research led into the development of a theoretical model and custom designed software discussed in Chapter 5.

CHAPTER 5: PHYSICAL OPTICS MODELLING OF THE IMAGING PROCESS THROUGH OPTICAL PHASE PLATES

The application of the Scalar Diffraction Theory to imaging with quasi-monochromatic incoherent light fields presented in this work was motivated by the domain of optically created special effects, specifically as it applies to propagating an optical field through non-shift-invariant optical phase plates strategically positioned within the optics utilized to create the desired special effects. A key contribution of this work is the presentation of a generalized non-paraxial theoretical framework based on the Rayleigh-Sommerfeld diffraction formulation allowing for the application of the scalar diffraction theory to imaging with quasi-monochromatic incoherent illumination across large fields of view (FOVs). This generalized framework extends the paraxial-imaging framework reviewed in Section 5.2 to the non-paraxial case. [Shaoulov, Rolland, et. al, 2004]

5.1 Introduction

Many imaging situations, from microscopy to space optics, can be well-modeled using raytracing theory, as previously discussed in Chapter 4. Some exceptions to that rule include modeling propagation of optical waves in nonlinear media, or accounting for coherent or partially coherent light propagation occurring in optical fibers, medium with microscopic refractive index variations, and integrated optical components and systems, for example. A

good model to describe propagation of light in such systems is the finite-element beam propagation method.[Vincetti, et al,, 2000] Another approach to modeling the propagation of optical waves in an optical system, the Gaussian beam decomposition method, is generally applicable in the case where the slowly varying envelop approximation (SVEA) holds. Such approach is often used to model laser beams or optical field propagation through bulk optics. [Montoya-Hernandez, et al., 1999] Finally, for linear shift-invariant systems (LSI), imaging may be modeled using Fourier transform methods, where the final image is obtained as a convolution of the object with a transfer function.[Goodman, 2000] The linearity of an optical system in the most general case implies that the superposition principle holds

$$g_2(x_2, y_2) = \iint g_1(\xi, \eta) h(x_2, y_2; \xi, \eta) d\xi d\eta \qquad (5.1)$$

where g_1 is the input function of a scene's points whose coordinates may be denoted as ξ and η, g_2 is the output function of the image points of coordinates x_2 and y_2 in the case of Eq. (5.1), and h represents the system's point response that is a function, generally speaking, of ξ, η, x_2 and y_2. The linearity of an optical system further implies that the performance of the system is independent of the magnitude of the input function.

Furthermore, the shift invariance property of an optical system implies that the system can be described by a transfer function h, independent of the input and the output (i.e. the output of the system is equal to the input to the system convolved with a transfer function intrinsic to the system itself, while independent of the input and the output). It should be noted that Eq. 5.1. can describe either linear, or LSI systems, depending on the specified properties of the

transfer function. The relationships describing an LSI are summarized in Fig. 5.1. in the spatial and the Fourier domain, respectively. [Gaskill, 1978]

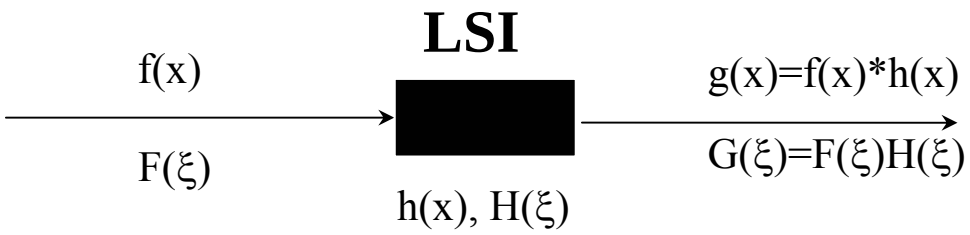

Figure 5.1 General relationships describing a LSI optical system.

Furthermore, some imaging system may have a large field of view (FOV) as in live image capture.[Rolland, Hylen, 1999], [Shaoulov, Rolland, 2001] It is beyond the scope of this Chapter to detail such an imaging system for special effects or to demonstrate the creation of special effects, which also requires an optimization of optical texture plates. In this Chapter, we present a non-paraxial imaging approach that will be essential in future work related to modeling image formation through such phase plates. The modeling approach will also be broadly applicable to non-shift invariant imaging systems, beyond that of creating special effects.

It is important to note that a system may be non-shift invariant and optical aberration free. Such case may be encountered in the creation of optical special effects, where the non-shift invariance is created by the texture plates and not the optical aberrations of the imaging optics. However, optical aberrations may contribute to non-shift invariant optical imaging if not fully balanced across the entire FOV. For the live image capture application, the imaging optics should be designed to be distortion free and well corrected to the extent possible for

optical aberrations, given that the optics may be utilized with or without the phase plates. Also, if a phase plate is utilized, the imaging optics will be used slightly out of focus as previously discussed throughout this work, therefore the main challenge to this problem is not to model imaging through an aberrated optics, but rather to correctly model 1st order wide FOV imaging, in or out of focus, and to have a modeling approach that will naturally allow in the future the insertion of an optical phase plate anywhere within the optics. If a non-shift invariant texture phase plate is located along the optical path, a non-shift invariant imaging model is required regardless of the fact that the imaging optics may be diffraction limited (i.e. "perfect optics").

The raytracing approach was first implemented in early stages of our investigation as discussed in Chapter 4, however the application of this approach was limited by the assumption of spatial incoherence everywhere along the optical path and failed to provide a theoretical model describing the behavior of an optical phase plate. [Shaoulov, Rolland, 2001] Furthermore, because phase plates are in general non-shift-invariant, the final image cannot be obtained as a simple convolution. Thus, the use of Fourier Transforms based algorithms is not applicable to describe correctly the imaging process. Specifically, there is no advantage to use the Fresnel Approximation in the scalar diffraction theory, and the associated approximations and simplifications that are conventionally used to introduce Fourier transforms, as part of the imaging process. [Goodman, 2000] In practice, for very specific image formation problems, it would be interesting to compare various modeling approaches with their associated approximations. Moreover, because the structure of the texture plates is rough, neither Gaussian Beam Decomposition algorithms, nor stationary

scattering techniques such as the Harvey-Shack technique, are applicable. Thus, in order to model the imaging process through a structure imposing such restrictions, a different approach had to be investigated, and custom software implementation had to be developed.

5.2 Review of the Theoretical Framework for Quasi-Monochromatic Incoherent Illumination

Scalar Diffraction Theory has been previously proposed to model quasi-monochromatic incoherent imaging for describing light propagation through a linear optical system. [Goodman, 2000] Such modeling is based on the classical Rayleigh-Sommerfeld diffraction representation.

Let's consider a linear optical system consisting of an object, an aberration-free optics, and an imaging surface (e.g. a plane is a special case) as shown in Fig. 5.2. If we denote the local coordinate systems in the object, the exit pupil, and the image as [$\xi;\eta$], [$x;y$] and [$u;v$], respectively, and the optical field in the object plane by its complex amplitude $U_o(\xi;\eta)$, then the complex amplitude in the imaging plane $U_i(u;v)$ will be expressed as

$$U_i(u,v) = \int_{-\infty}^{\infty}\int_{-\infty}^{\infty} d\xi d\eta U_0(\xi,\eta) h(u,v;\xi,\eta) \tag{5.2}$$

where $h(u,v;\xi,\eta)$ is the transfer function of the investigated system for a point $[u,v]$ given $[\xi,\eta]$. [Goodman, 2000]

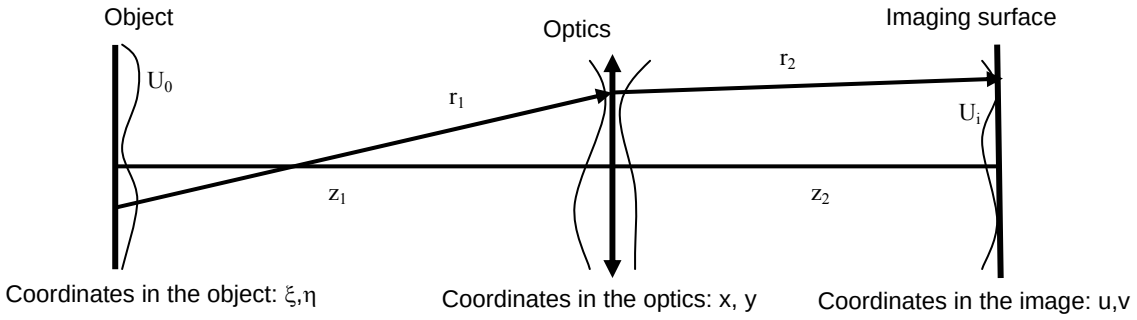

Figure 5.2 Layout of an optical system consisting of an object illuminated with a spatially incoherent quasi-monochromatic light field of complex amplitude U_0, an aberration-free optics, and an arbitrary imaging plane.

To derive a closed form expression for the transfer function of the investigated system, let's first consider the light propagation from the object to the lens, denoted by $U_l(x,y)$. Furthermore, we will assume the object to be a self-emitting amplitude mask, i.e. each point of the object will be considered as a source of a spherical wave of the type

$$\frac{e^{jkr_i}}{j\lambda r_i} \tag{5.3}$$

Therefore, the propagation from the object to the lens is described by the Rayleigh-Sommerfeld integral

$$U_l(x,y) = \int_{-\infty}^{\infty}\int h(x,y;\xi,\eta)U_0(\xi,\eta)P(x,y)\,d\xi d\eta\,, \tag{5.4}$$

where $P(x,y)$ is a pupil function defined as

$$P(x,y) = \begin{cases} 1, \text{ within the pupil} \\ 0, \text{ outside the pupil} \end{cases}. \tag{5.5}$$

Also, the optical field immediately after the lens is described by

$$U'_l(x,y) = U_l(x,y)\, e^{-j\frac{k}{2f}\left(x^2+y^2\right)} \tag{5.6}$$

where $e^{-j\frac{k}{2f}\left(x^2+y^2\right)}$ is the paraxial lens propagator in the paraxial approximation. Combining Eqs. (5.2) – (5.6) the optical field distribution at the final image plane can be written as

$$\begin{aligned} U_i(u,v) &= \int_{-\infty}^{\infty}\int h(u,v;x,y)\,U'_l(x,y)\,dxdy = \\ &= \int_{-\infty}^{\infty}\int dxdy\,U_l(x,y)\,e^{-j\frac{k}{2f}\left(x^2+y^2\right)} h(u,v;x,y) = \\ &= \int_{-\infty}^{\infty}\int dxdy\,U_l(x,y)\,e^{-j\frac{k}{2f}\left(x^2+y^2\right)} \frac{1}{j\lambda}\frac{e^{jkr_2}}{r_2}\cos\theta_2 = \\ &= \frac{1}{j\lambda}\int_{-\infty}^{\infty}\int dxdy\,\frac{e^{jkr_2}}{r_2}\,e^{-j\frac{k}{2f}\left(x^2+y^2\right)}\cos\theta_2 \int_{-\infty}^{\infty}\int d\xi d\eta U_0(\xi,\eta)\,h(x,y;\xi,\eta) = \\ &= -\frac{1}{\lambda^2}\int_{-\infty}^{\infty}\int dxdy\,\frac{e^{jkr_2}}{r_2}\,e^{-j\frac{k}{2f}\left(x^2+y^2\right)}\cos\theta_2 \int_{-\infty}^{\infty}\int d\xi d\eta U_0(\xi,\eta)\,\frac{e^{jkr_1}}{r_1}\cos\theta_1 \end{aligned} \tag{5.7}$$

where $cos\theta_{1,2}$ are the obliquity factors. Thus, if we consider the pupil function we can further write

$$U_i(u,v) = -\frac{1}{\lambda^2}\int_{-\infty}^{\infty}\int dxdy\left[P(x,y)\,\frac{e^{jkr_2}}{r_2}\,e^{-j\frac{k}{2f}\left(x^2+y^2\right)}\cos\theta_2 \int_{-\infty}^{\infty}\int d\xi d\eta U_0(\xi,\eta)\,\frac{e^{jkr_1}}{r_1}\cos\theta_1\right]. \tag{5.8}$$

The irradiance in the final image plane is given from

$$I_i(u,v) = U_i(u,v)\,U_i^*(u',v'). \tag{5.9}$$

Considering the general expression for $U_i(u,v)$

$$U_i(u,v) = \int_{-\infty}^{\infty}\int_{-\infty}^{\infty} d\xi d\eta U_0(\xi,\eta)\,h(u,v;\xi,\eta) \tag{5.10}$$

we can rewrite Eq.(5.10) as

$$I_i(u,v)=\left[\int_{-\infty}^{\infty}\int_{-\infty}^{\infty}d\xi d\eta U_0(\xi,\eta)h(u,v;\xi,\eta)\right]\left[\int_{-\infty}^{\infty}\int_{-\infty}^{\infty}d\xi' d\eta' U_0(\xi',\eta')h(u,v;\xi',\eta')\right]^* \quad (5.11)$$

where

$$\{\xi,\xi',\eta,\eta'\}\in\mathbb{R} \quad (5.12)$$

Thus, Eq.(5.11) can be further simplified to

$$I_i(u,v)=\int_{-\infty}^{\infty}\int_{-\infty}^{\infty}d\xi d\eta U_0(\xi,\eta)h(u,v;\xi,\eta)\int_{-\infty}^{\infty}\int_{-\infty}^{\infty}d\xi' d\eta' U_0^*(\xi',\eta')h^*(u,v;\xi',\eta') \quad (5.13)$$

Furthermore, to express the irradiance distribution in the image, we must consider the statistical properties of the light. By assuming ergodicity of the statistical imaging process and applying Fubini's theorem,[Royden, 1968] the irradiance distribution in the image may be further written as

$$\langle I_i\rangle(u,v)=\int_{-\infty}^{\infty}\iiint\left\langle U_0(\xi,\eta)U_0^*(\xi',\eta')\right\rangle h(u,v;\xi,\eta)h^*(u,v;\xi',\eta')d\xi d\eta d\xi' d\eta' \quad (5.14)$$

where the brackets in the left hand side term denote the mean over time and the brackets in the right-hand side denote ensemble average.[Goodman, Statistical Optics, 2000] Finally, assuming spatially incoherent illumination we obtain

$$\left\langle U_0(\xi,\eta)U_0^*(\xi',\eta')\right\rangle=\left\langle\left|U_0(\xi,\eta)\right|^2\right\rangle\delta(\xi-\xi')\delta(\eta-\eta')\equiv\left\langle I_0(\xi,\eta)\delta(\xi-\xi')\delta(\eta-\eta')\right\rangle \quad (5.15)$$

and thus Eq. (5.14) yields

$$\left\langle I_i(u,v)\right\rangle=\int_{-\infty}^{\infty}\int\left\langle I_0(\xi,\eta)\right\rangle\left|h(u,v;\xi,\eta)\right|^2 d\xi d\eta \quad (5.16)$$

Thus, Eq.(5.16) provides the relationship between the irradiance distribution in the image and the irradiance distribution in the object illuminated with quasi-monochromatic and spatially incoherent light under the assumption of ergodicity of the imaging process. Furthermore, the expression for the transfer function must be formally established to apply this framework to different imaging configurations (e.g. paraxial; non-paraxial aberration free; non-paraxial combined with optical aberrations; any of the above with defocus, given that defocus is best considered as a 1st-order imaging property).

5.3 Application of the Paraxial Framework to Plane-to-Plane and Plane-to-Curve Imaging Configurations

In the special case of interest for this work, a system is consisting of free space propagation, followed by propagation through an aberration-free optics of focal length *f*, and consequent propagation through free space, the paraxial transfer function based on applying Rayleigh-Sommerfeld formula and Eqs. (5.8) and (5.14) is given by

$$\begin{aligned} h(u,v;\xi,\eta;x,y) &= \left(-\frac{1}{j\lambda}\right)\frac{e^{jkr_1}}{r_1}e^{-j\frac{k}{2f}\left(x^2+y^2\right)}\left(-\frac{1}{j\lambda}\right)\frac{e^{jkr_2}}{r_2}\cos\theta_1\cos\theta_2 = \\ &= -\frac{1}{\lambda^2 r_1 r_2}e^{jkr_1}e^{-j\frac{k}{2f}\left(x^2+y^2\right)}e^{jkr_2}\cos\theta_1\cos\theta_2 \end{aligned} \tag{5.17}$$

Integrating over *(x,y)* we obtain

$$h(u,v;\xi,\eta) = -\int_{-\infty}^{\infty}\int dxdyP(x,y)\,h(u,v;\xi,\eta;x,y) = \\ = \int_{-\infty}^{\infty}\int dxdyP(x,y)\frac{1}{\lambda^2 r_1 r_2}e^{jkr_1}e^{-j\frac{k}{2f}\left(x^2+y^2\right)}e^{jkr_2}\cos\theta_1\cos\theta_2 \tag{5.18}$$

or after rearranging the terms

$$h(u,v;\xi,\eta) = \int_{-\infty}^{\infty}\int_{-\infty}^{\infty} dxdyP(x,y)\left[\frac{e^{jkr_1}}{j\lambda r_1}\cos\theta_1\right]\left[e^{-j\frac{k}{2f}\left(x^2+y^2\right)}\right]\left[\frac{e^{jkr_2}}{j\lambda r_2}\cos\theta_2\right] \tag{5.19}$$

where k is the wave number, λ is the central wavelength, $\cos\theta_1$ and $\cos\theta_2$ are the obliquity factors, and $P(x,y)$ is a pupil function equal to one inside the pupil and zero everywhere else. In Eq.(5.19) r_1 and r_2 are defined as

$$r_1 = \left[(x-\xi)^2 + (y-\eta)^2 + z_1^2\right]^{1/2} \\ r_2 = \left[(u-x)^2 + (v-y)^2 + z_2^2\right]^{1/2} \tag{5.20}.$$

The obliquity factors occur by considering the geometry of parallel object-to-pupil and pupil-to-image plane-to-plane imaging. Thus, one may infer that this expression would hold some validity in the non-paraxial region once the parabolic approximation to the optics transfer function is replaced by the exact expression. We shall demonstrate in Section 5.4. that such inference fails. Eq.(5.19) is quite similar to the framework presented in Section 10-6 in Gaskill, [Gaskill, 1978] however, it has been made formally a function of all four variables, thus allowing to model non-shift invariant systems.

Furthermore, from the theory of first order imaging properties, it is known that even for perfectly stigmatic imaging (i.e. aberration-free, or point-to-point, imaging), the image is not

distributed on a plane surface but rather on a curved surface, called the Petzval surface, as shown in Fig. 5.3. Without loss of generality in illustrating the Petzval surface, Fig. 5.3 depicts the case of an object at optical infinity.[Slyusarev, 1984], [Malacara, 1994] In this case, the surface can be shown to describe a portion of a sphere with radius *f*.

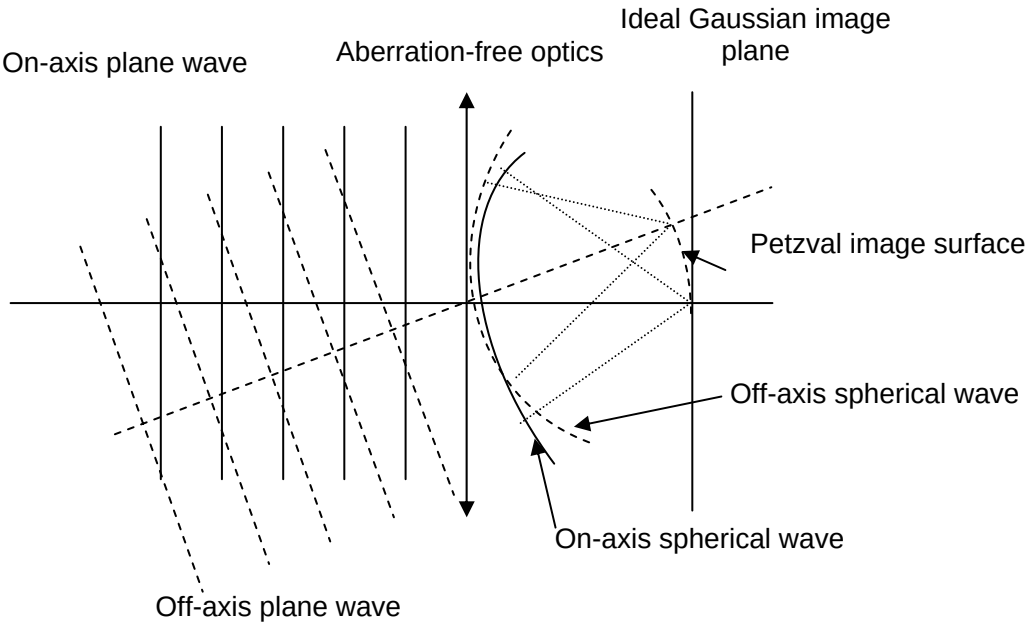

Figure 5.3 Illustration of stigmatic imaging on a curve surface for an object located at optical infinity.

If the object is located at finite distance from the optics, the surface shape may be computed using first order imaging equations.[Mouroulis, Macdonald, 1996], [Rolland, Shaoulov, Gonzales, 2001] Thus, a next step in the formal representation of the basic framework set in Eq.(5.19) is to consider a plane-to-Petzval-surface imaging process in order to fully validate that sharp imaging occurs on the predicted curved surface. If field curvature imposed by

Petzval curvature is severe, as occurring if the optics is not specifically designed with multiple elements to flatten the field and is imaging large FOVs, the image formed on a plane will be extremely blurred in intensity as one goes up in the FOV along the detection plane. Also in a simulation with a limited dynamic range (i.e. 0-255 greylevels) to represent intensity variations, most of the image will appear to fall within the lowest level of the greyscale, thus making it difficult to assess the validity of the imaging process, even simply according to its first order imaging properties. We will demonstrate such limitations in Section 5.4 and 5.5. Imaging on a curved surface as opposed to a plane, does not signifies that we ignore the Petzval curvature. To the opposite, it signifies that we take it into account in the validation of first-order imaging properties. Such a choice is a necessary step in the validation procedure. Thus, the expression for r_2 in Eq.(5.20) was modified to

$$r'_2 = \left[(u-x)^2 + (v-y)^2 + z'^2_2 \right]^{1/2} \tag{5.21}$$

where z'_2 is calculated from the Descartes' first order imaging equation,[Mouroulis, Macdonald, 1996], [Rolland, Shaoulov, Gonzales, 2001] given z'_1 separately for each set of points $[\xi;\eta]$ and $[u;v]$.

5.4 Generalized Non-Paraxial Theoretical Framework Based on the Rayleigh-Sommerfeld Scalar Diffraction Theory

Paraxial imaging is generally rigorously defined for infinitely small object size and small angles of incidence on optical elements. Thus, any real imaging scenario, unless on axis only, usually violates the paraxial approximation. In imaging, one then often distinguishes between

paraxial, quasi-paraxial imaging (i.e. which applies for FOVs < 10 degrees and an optics of an F-number (F#) of 10 or more), and non-paraxial (i.e. FOV > 10 degrees or an optics of F# less than 10). Non-paraxial imaging comprises two components in imaging: first-order properties, and higher-order imaging properties. First-order properties assume an aberration-free optics and the ability to model in focus imaging on the Petzval surface, as well as imaging with defocus. Higher-order properties include optical aberrations. This work focuses on the first-order non-paraxial imaging properties for an aberration-free system. The introduction of optical aberrations is a straightforward step as further described thereafter. First, let's remove the paraxial parabolic approximation in the lens function given in Eq. (5.6). Starting with the Descartes' equation

$$\upsilon' = \upsilon + C \tag{5.22}$$

or

$$\frac{n'}{z'} = \frac{n}{z} + \frac{n'}{f'} \tag{5.23}$$

in the case of propagation through air we can write

$$n' = n = 1 \quad \therefore \frac{1}{z'} = \frac{1}{z} + \frac{1}{f'} \qquad \therefore \frac{1}{z_2} = \frac{1}{z_1} + \frac{1}{f'} \tag{5.24}$$

Considering the case of finite conjugates as shown in Fig. 5.4 we can apply the Pythagorean Theorem and express the optical path difference with no approximation as

$$\left(z_{1,2} - \delta_{1,2}\right)^2 + \rho^2 = z_{1,2}^2 \tag{5.25}$$

we can rewrite Eq. (5.25) as

$$\begin{aligned} z_1^2 - 2z_1\delta_1 + \delta_1^2 + \rho^2 &= z_1^2 \\ z_2^2 - 2z_2\delta_1 + \delta_2^2 + \rho^2 &= z_2^2 \end{aligned} \tag{5.26}$$

The solutions to the Eqs. (5.26) are given as

$$\begin{aligned}\delta_{1_{1,2}} &= -z_1 \pm \left[z_1^2 - \rho^2 \right]^{1/2} \\ \delta_{2_{1,2}} &= -z_2 \pm \left[z_2^2 - \rho^2 \right]^{1/2}\end{aligned} \tag{5.27}$$

Furthermore, to identify the correct sign in the Eqs. (5.27), let's pick the extreme cases. First, let's consider an object at infinity (i.e. a plane wave)

$$\begin{gathered}z_1 \to \infty; \quad \delta_1 = 0 \quad \therefore \frac{1}{z_2} = \frac{1}{\underbrace{z_1}_{0}} + \frac{1}{f} \quad \therefore z_2 = f \\ \delta_{1_{1,2}} = -z_1 \pm \left[z_1^2 - \rho^2 \right]^{1/2} = -z_1 \pm z_1 \left[1 - \frac{\rho^2}{\underbrace{z_1^2}_{0}} \right]^{1/2} = -z_1 \pm z_1 \\ \therefore \delta_{1_{1,2}} = \begin{cases} \lim_{z_1 \to \infty} \left(-2z_1 \right) = -\infty \\ 0 \end{cases}\end{gathered} \tag{5.28}$$

Thus, it is seen that only the "+" sign describes correctly the imaging scenario for δ_1. Furthermore, if we consider an object at infinity (i.e. a plane wave), then the image must be formed in the focal point image in the case of a converging lens, thus

$$\begin{gathered}z_1 \to \infty; \quad \delta_1 = 0; \quad \Delta W = \delta_2; \quad x_1 \equiv x; \quad y_2 \equiv y; \quad z \equiv f; \quad \frac{x^2 + y^2}{f^2} \ll 1 \\ \therefore \left[1 - \frac{x_2^2 + y_2^2}{z_2^2} \right]^{1/2} = \left[1 - \frac{x^2 + y^2}{f^2} \right]^{1/2} \approx 1 - \frac{x^2 + y^2}{2f^2} \\ \therefore \delta_{2_{1,2}} = -f \pm f \left[1 - \frac{x^2 + y^2}{2f^2} \right] = -f \pm f \mp \frac{x^2 + y^2}{2f} \\ \therefore \delta_{2_{1,2}} = \begin{cases} -2f + \dfrac{x^2 + y^2}{2f} \\ -\dfrac{x^2 + y^2}{2f} \end{cases}\end{gathered} \tag{5.29}$$

Therefore, it is seen that only the "+" sign describes correctly the imaging scenario for δ_2 as well. Thus, we established the correct solutions of Eqs. under the considered imaging scenario, which will allow us to further remove the parabolic approximation from the lens transfer function. Let's consider the overall optical path difference (OPD) as shown in Fig. 5.4.

$$\begin{aligned}\delta_1+\delta_2 &= -\left(z_1+z_2\right)+\left[z_1^2-\rho^2\right]^{1/2}+\left[z_2^2-\rho^2\right]^{1/2}= \\ &= -\left(z_1+z_2\right)+z_1\left[1-\frac{\delta_1^2}{z_1^2}\right]^{1/2}+z_2\left[1-\frac{\delta_2^2}{z_2^2}\right]^{1/2}\end{aligned} \tag{5.30}$$

In the lens coordinate system *(x,y)* the OPDs can be written as

$$\delta_{1,2}^2 = x_{1,2}^2+y_{1,2}^2 \tag{5.31}$$

Thus, the OPD can be expressed as

$$OPD=\Delta W=\delta_1+\delta_2=-\left(z_1+z_2\right)+z_1\left[1-\frac{x_1^2+y_1^2}{z_1^2}\right]^{1/2}+z_2\left[1-\frac{x_2^2+y_2^2}{z_2^2}\right]^{1/2} \tag{5.32}$$

and the lens transformation function in the most general case can be written as

$$e^{jk\Delta W}=e^{-jk\left[\left(z_1+z_2\right)-z_1\left[1-\frac{x_1^2+y_1^2}{z_1^2}\right]^{1/2}-z_2\left[1-\frac{x_2^2+y_2^2}{z_2^2}\right]^{1/2}\right]} \tag{5.33}$$

To check the validity of Eq.(5.49) let's consider again an object at infinity and demonstrate that the solution converges to the well known parabolic approximation

$$z_1 \to \infty; \quad \delta_1 = 0; \quad \Delta W = \delta_2; \quad x_1 \equiv x; \quad y_2 \equiv y; \quad z \equiv f; \quad \frac{x^2+y^2}{f^2} \ll 1$$

$$\therefore \left[1 - \frac{x_2^2 + y_2^2}{z_2^2}\right]^{1/2} = \left[1 - \frac{x^2+y^2}{f^2}\right]^{1/2} \approx 1 - \frac{x^2+y^2}{2f^2} \tag{5.34}$$

$$\therefore e^{jk\Delta W} = e^{-jk\left(f - f\left[1 - \frac{x^2+y^2}{2f^2}\right]\right)} = e^{-j\frac{k}{2f}\left(x^2+y^2\right)}$$

Thus, Eq.(5.50) demonstrates that the parabolic approximation for the lens transfer function follows naturally from the most general expression given by Eq.(5.49). There is no need to make the parabolic approximation and thus such approximation will not be made.

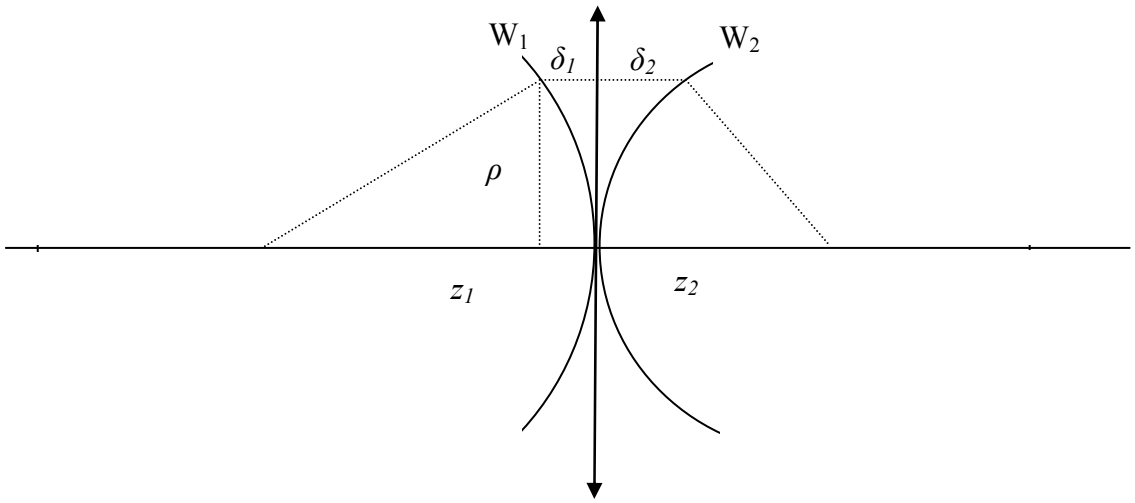

Figure 5.4 Calculation of the optical path difference in the most general case of a converging optical system.

A key to generalize the basic framework for non-paraxial imaging was the realization that the phase transformation performed by the optics, whether it is the parabolic approximation or the exact form, has to be applied on a transformation plane tilted with respect to the optical

axis. Equivalently, the transformation must be applied in such a way that it remains normal to the chief ray for each point [$\xi;\eta$] in the object, as illustrated in Fig. 5.5. The physical meaning of the tilted summation plane may be best understood by considering the special case of an extended object at infinity. The wavefront reaching the optics from a point in the FOV is tilted with respect to the optical axis and perpendicular to the chief ray. The lens function is to transform such plane wavefront into a spherical wavefront whose center of curvature lays off-axis on the Petzval surface. Such an imaging property may be accomplished by an optics transformation function that is rotationally symmetric, while not strictly speaking quadratic, with respect to the chief ray. The concept of the tilted plane for summation applies equally well for an object at finite distance from the optics, given that the tilted summation plane is perpendicular to the chief ray in all cases and tangent to the incident wavefront emanating from any object point in the FOV. Therefore, the expressions for r_1 and r_2 in Eq.(5.30) were modified to

$$\begin{aligned} r'_1 &= \left[\left(x'-\xi\right)^2 + \left(y'-\eta\right)^2 + z'^2_1 \right]^{1/2} \\ r'_2 &= \left[\left(u-x'\right)^2 + \left(v-y'\right)^2 + z'^2_2 \right]^{1/2} \end{aligned} \tag{5.35}$$

where [$x';y'$] are the coordinates in the tilted lens transformation plane. Thus, the transfer function introduced in Eq.(5.28) can be written as

$$h\left(u,v;\xi,\eta\right) = -\int_{-\infty}^{\infty}\int_{-\infty}^{\infty} dx'dy' P\left(x',y'\right) \frac{e^{jkr'_1} e^{-jk\left((z'_1+z'_2) - z'_1\left[1-\frac{x'^2+y'^2}{z'^2_1}\right]^{1/2} - z'_2\left[1-\frac{x'^2+y'^2}{z'^2_2}\right]^{1/2} \right)} e^{jkr'_2}}{\lambda^2 r'_1 r'_2} \tag{5.36}$$

where the projected pupil function $P(x',y')$ is again equal to 1 inside the projection of the aperture on the tilted plane and equal to zero outside. Also, z'_1 and z'_2 are related through the

Descartes' equation given in Eq. (5.24), and the function describing the optics as a focusing element with no aberrations is an exact expression, instead of the parabolic approximation. The lens term in Eq.(5.36) was derived by considering the dephasing needed to be introduced by a converging lens to map a diverging spherical wavefront to a converging spherical wavefront. With this mathematical formulation, there is no need for the obliquity factors given that the summation planes are always perpendicular to the chief rays.

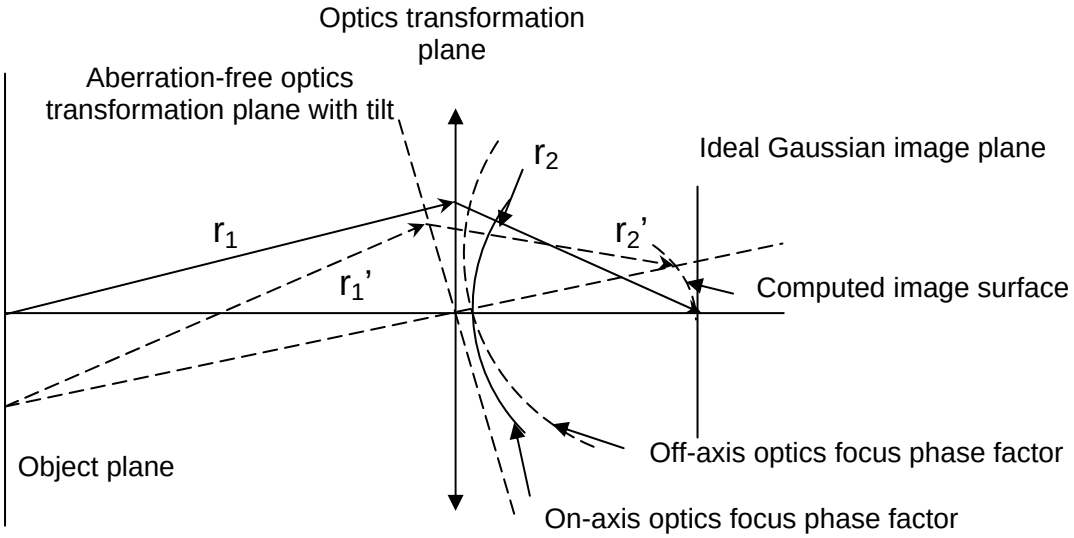

Figure 5.5 Generalized non-paraxial imaging framework with the transformation plane normal to the chief ray and tilted with respect to the paraxial transformation plane.

5.5 Results

In order to fully demonstrate the capability of the model described in Section 5.4, we must first choose reasonable values for the parameters of the optical system not only within the quasi-paraxial region, but preferably within the non-paraxial region. Thus, the object was

considered located at a distance of *2f* away from an F/5 aberration-free optics of 20mm focal length, allowing testing of both the paraxial and the non-paraxial frameworks for various FOVs.

The mathematical framework was implemented using conventional numerical quadrature techniques.[Burden, Fairies, 2000] Given the high number of computations involved, the computation time for the simulation of one imaging condition was over three weeks on a single processor platform. Thus, an alternative computational approach had to be established. The next generation implementation was developed on a Beowulf cluster utilizing 96 dual 1.3Ghz Athlon processor nodes.[Spector, 2000] The computation to generate the simulated images was easily spatially partitioned to handle sub sections of the object to be imaged. This distribution resulted in implicit load balancing. The time complexity and accuracy in terms of the size of the matrix elements, as well as the scalability on a parallel platform are a subject of the future work because they require an in-depth investigation on various parallel architectures including 32-bit versus 64-bit processors, as well as on SMP (Symmetric Multi Processing) and NUMA (Non Uniform Memory Access) based computing platforms.[Donagarra, 2002] With the Beowulf cluster implementation the computation time was reduced to minutes which allowed us to further investigate the modeling approach.

The generalized non-paraxial theoretical framework for plane-to-curve imaging was compared to the paraxial or more precisely the quasi-paraxial framework for plane-to curve imaging reviewed in Section 5.3, by using a 256 greylevel bitmap object filling 40 degrees FOV. Eq.(5.19), which defines the paraxial and quasi-paraxial framework, may be thought

to be paraxial or quasi-paraxial because of the parabolic approximation to the optics transformation function. However, the main reason for this equation to be limited to the quasi-paraxial region is the application of the optics transformation function on a plane perpendicular to the optical axis, as we shall show in the simulations. Eq.(5.36) addresses both limitations of Eq.(5.19) by using an exact optics transformation function and applying it in a plane perpendicular to the chief ray for each point in the FOV.

All results presented correspond to plane-to-curve imaging, where the Petzval surface was computed for the geometry provided, to ensure that a lack of a good image or even an image across the full FOV is not a consequence of Petzval curvature. Under realistic imaging conditions with an optimized optics, the Petzval curvature will be moderate, and in the case of plane-to-plane imaging it will only cause slight blur as the image extends further in the FOV. However, because we do not use a field flattener within the optics or other ways (i.e. combination of positive and negative separated optical elements) to reduce the Petzval curvature, the Petzval surface curves severely in the case we considered, and must be accounted for by imaging on its curved surface. In the case where optimized optics with their flattened Petzval curvature and associated optical aberrations is considered, the optics transformation can be built accordingly. The optics transformation is always applied in the exit pupil to model the entire optics via one phase transformation. Furthermore, under all imaging conditions, the images of the face where presented upright for easier comparison, accounting for the optics providing inverted images.

Results shown in Fig. 5.6.(a) demonstrate that the paraxial framework fails for large FOVs as expected. Only a portion of the face imaged within the quasi-paraxial region is seen sharply. Past the quasi-paraxial region, the image dims so quickly, that when displayed on a 0-255 greylevel scale, it is non-perceivable. To further yield insight into the issue of dynamic range (i.e. relative brightness for various points in the FOV), an object with a small square at the edge was selected as the object to be imaged as shown in Fig. 5.7(a). The result from the paraxial framework is demonstrated in Fig. 5.7.(b), where the white square appears at expected but somewhat dimmer. Also, the intensity within the square is non-uniform. In this simple stimulus case, because there is not light intensity anywhere else in the object and the non-uniformities within the square are relatively small, no other part of the object competes for the dynamic range, thus when the image output is scaled from 0-255 graylevels, no matter how dim in average the square at the edge is, it will be displayed at graylevels close to 255.

Object

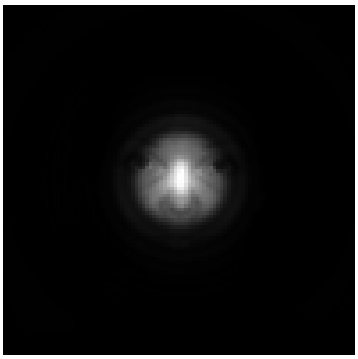

(a)

(b)

(c)

Figure 5.6 Results of imaging a 40 degree FOV object in a 2f imaging configuration for plane-to-curve imaging: (a) paraxial/quasi-paraxial model given by Eq.(2), (b) Non-paraxial model given by Eq.(5) for in-focus imaging (c) same as (b) but with 3mm out-of-focus imaging.

(a) (b)

Figure 5.7 Demonstration of the existence of low light levels at the edge of the FOV in the case of the paraxial model in the case of plane-to-curve imaging: (a) Object with one white square at the edge of the FOV (b) Image.

If we now consider an object with two squares, one in the center and one at the edge, as shown in Fig. 5.8(a), results from both the paraxial and the non-paraxial framework are shown in Figs. 5.8.(b) and 5.8.(c), respectively. Results indicate that using the paraxial framework, the square at the edge now disappears, indicating that it is a lot dimmer than the one in the center. The non-paraxial framework yields imaging of both squares with equal brightness on the curved surface as one expects from an appropriate 1st-order non-paraxial imaging framework.

Results shown in Fig. 5.6.(b) demonstrate that the expanded non-paraxial framework works for large FOVs. Finally, to verify the first-order defocusing imaging properties with the non-paraxial framework, the imaging surface was placed 3mm out of focus toward the optics.

Results presented in Fig. 5.6.(c) demonstrate that the generalized non-paraxial theoretical framework works for out-of-focus imaging as well.

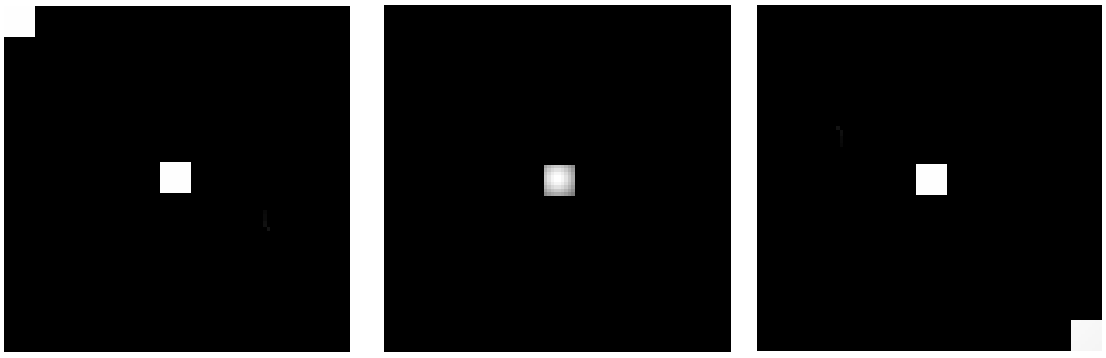

Figure 5.8 Demonstration of the existence of low light levels at the edge of the FOV in the case of the paraxial model and for plane-to-curve imaging: (a) Object with one white square in the middle, and one white square at the edge. (b) Image of (a) using the paraxial model; the square at the edge is extremely dim with respect to that in the center and thus cannot be seen within a limited 255 greylevels display (c) Image of (a) using the non-paraxial model. Such imaging scenario models accurately imaging with a 40 degree FOV.

Finally, we intend for this work to bring forth the fact that within the paraxial framework, the parabolic approximation to the optics transformation function can be insignificant compared to the fact that, in that regime, the optics transformation is applied in a plane perpendicular to the optical axis. Furthermore, if we are correct, the non-paraxial framework would work equally well with or without the parabolic approximation to the optics transformation for moderate F-number, as long as the summation occurs in a plane perpendicular to the chief ray. Thus, we ran a simulation with the non-paraxial equation under both cases of the optics

transformation. Results presented in Fig. 5.9. indicate that the non-paraxial framework works equally well with the parabolic approximation to the optics transformation function and with the exact expression, while results presented in Fig. 5.6.(a) and (b) indicated that even when the exact expression to the optics transformation function was used, imaging failed if the optics transformation was not applied in a plane perpendicular to the chief ray.

(a) (b)

Figure 5.9 Results of the non-paraxial theoretical framework for plane-to-curve imaging: (a) using no approximation for the optics transformation, except assuming an aberration-free optics. (b) using nevertheless the parabolic optics transformation approximation, which could be thought to be responsible for having the model provided by Eq.(5.25) fail. Results reveal that the parabolic approximation for the optics transformation leads to negligible effects on overall imaging even for non-paraxial imaging, thus such approximation could be employed even in some non-paraxial case (i.e. moderate F-number) if it was to reduce the complexity of the computations.

5.6 Discussion and future work

In conclusion, the formulation of the Rayleigh-Sommerfeld scalar diffraction theory was applied to optical imaging of extended objects under quasi-monochromatic incoherent illumination. The existing theoretical framework was generalized to non-paraxial in- and out-of-focus imaging and results were obtained to verify the generalized framework. In that framework, the optical system was considered linear. In the generalized non-paraxial framework even the most complex linear systems, without any assumptions for shift invariance, can be modeled and analyzed. Finally, this work will be extended in the near future to include higher order aberrations in the optics transformation equation and special effects imaging, by including a propagation stage through optical phase plates.

CHAPTER 6: CONCLUSIONS AND FUTURE WORK

The work presented in this dissertation was inspired by the idea of optically created special effects, [Hylen, 1997] [Rolland, Hylen, 1999] such as painterly effects, encoded in images captured by photographic cameras at the speed of light. We shall summarize our contribution in Section 6.1, and discuss future work in Section 6.2.

6.1 Summary of Contribution

As part of the work presented, compact relay optics was assessed and developed, as discussed in Chapters 3 and 4. It was concluded that even though compact relay optics can be achieved, further push for compactness and cost-effectiveness was impossible in the paradigm of bulk macro-optics systems. Thus, a new paradigm for imaging with multi-aperture micro-optics was presented and demonstrated for the first time, which constitutes one of the key contributions of this work. This new paradigm was further extended to the most general case of magnifying multi-aperture micro-optics systems. Such new paradigm allows extreme reduction of the size of imaging optics by a factor of ~10 and reduction of the weight by a factor of ~500, while the cost reduction is by a factor of ~100 after the initial cost is accumulated (e.g. after the master is made in the case of multi-aperture micro-optics based on imaging with stacks of microlenslet arrays). The application of such multi-aperture micro-optics extends beyond the domain of optically created special effects, and includes potential applications such as magnifying miniature displays within head-mounted displays

(HMDs) and 3D integral imaging. An astonishing property of multi-aperture micro-optics is that the increase of the desired field of view for a given optical system can simply be achieved by adding more micro-optical elements to the arrays, instead of redesigning the entire optical system as required in the case of bulk macro-optical systems. In terms of image quality, we established that trade-offs exist between resolution, lensletization, and the compactness of the multi-aperture micro-optical systems, e.g. in the case of 1:1 relay systems, the most compact configuration is also the worst in terms of lensletization, and we established that less compact arrangements yield less artifactual images. The compactness, simplicity, robustness and cost-effectiveness of the multi-aperture micro-optical systems demonstrated in this work hold a tremendous potential for commercialization and gradual replacement of expensive bulk-macro-optical systems in many applications. This part of our work led us to a US Patent [Shaoulov, Martins, Rolland, 2003], two peer-reviewed journal publications [Shaoulov, Rolland, 2003] [Shaoulov, Martins, Rolland, 2004] and four conference proceedings [Shaoulov, Martins, Rolland, 2004] [Martins, Shaoulov, Rolland, 2004], [Shaoulov, Martins, Rolland, 2003] [Shaoulov, Rolland, 2002].

Another key contribution of this work was the experimental quantification of the feasibility of optically created special effects proposed by Hylen [Hylen, 1997] and the consequent development of a raytracing based software, which was commercialized by SmARTLens^{TM}. This unique application of photography allows the photographers to perform real time image processing by changing the scene and the optical wave plate used as a function of their own artistic perception. Furthermore, the unmatched potential of this approach is in the art of movie-making, where entire sequences in a movie may be shot with the special effects

directly included in the movie, instead of performing post-shot computer processing, as currently utilized in the moviemaking industry. This work puts the foundation of the development of a commercially available high-end camera for photographic special effects and led to a conference proceeding [Shaoulov, Rolland, et. al., 2001] and a commercial product. [SmARTLens^{TM}, 2004]

Finally, as key contribution of this work, the principles of scalar diffraction theory were applied to optical imaging of extended objects under quasi-monochromatic incoherent illumination as discussed in Chapter 5. The existing theoretical framework was generalized to non-paraxial in- and out-of-focus imaging and results were obtained to verify the generalized framework. In that framework, the optical system was considered linear. In the generalized non-paraxial framework even the most complex linear systems, without any assumptions for shift invariance, can be modeled and analyzed. This work led us to one peer-reviewed journal publication [Shaoulov, Satya, Schiavone, Clarkson and Rolland, 2004] and one peer-reviewed conference abstract [Shaoulov, Satya, Schiavone, Clarkson and Rolland, 2003].

6.2 Future Work

As part of the future work, the image quality of multi-aperture micro-optics can be further quantified for specific driving applications. The work will further expand the research to investigate how stacks of microlenslet arrays may be optimized to satisfy various image quality criteria for various arrangements, in which lensletization was shown in Chapter 3 to

be negligible. Aspherization of the singlets demonstrated in Chapter 3 may be used in a more advanced configuration to minimize spherical and astigmatic aberrations, two main limiting monochromatic Seidel aberrations. Also, whether it is possible to design better systems by stacking more than two microlenslet arrays can be investigated. The design of task-driven optical solutions for various potential applications will allow the replacement of bulk macro-optical systems with ultra compact multi-aperture micro-optical systems, wherever possible. Such designs could lead to significant gain in compactness, weight and cost-effectiveness in many areas currently utilizing bulk macro-optics. Finally, fully working prototypes may be fabricated and tested in various application driven cases.

As part of the future work related to the raytracing approach presented in Chapter 4, a modified approach utilizing the raytracing approach in conjunction with a shift-variant point-spread function based on the Bidirectional Transmission Distribution Function (BTDF) of the optical phase plates can be developed and explored. [Goodman, Statistical Optics, 2000]

Finally, the generalized non-paraxial quasi-monochromatic theoretical framework presented in Chapter 5 can be extended to include higher order aberrations in the optics transformation equation and special effects imaging, by including a propagation stage through optical phase plates.

LIST OF REFERENCES

[A lens revolution, 1999] "A lens revolution", American Cinematography, Vol 80, No.5 137-138, May 1999.

[Anderson, 1979] R.H. Anderson, "Close-up imaging of documents and displays with lens arrays", Applied Optics 18(4), 477-484, (1979).

[ASAP, 2002] ASAPTM Technical Guide Radiometric Analysis, pp. 43-45, Breault Research Organization, Tucson, AZ, (2002).

[Baronti et al, 1998] S. Baronti, A. Cassini, F. Lotti and S. Porcinai, "Multispectral imaging system for the mapping of pigments in works of art by use of principal-component analysis", Applied Optics, Vol. 37, No. 8 [1299-1309], March 1998.

[Bergen and Andelson, 1988] J. R. Bergen and E.H. Adelson, "Early vision and texture perception, Nature, 333(6171) 363-364, 1988.

[Bergen and Landy, 1993] J. R. Bergen and M. S. Landy, "Computational modeling of visual texture segregation", Computational Models of Visual Perception, 253-271, MIT Press, Cambridge MA, 1991.

[Bergen, 1991] J. R. Bergen, "Theories of visual texture perception", Vision and Visual Dysfunction, Vol. 10B 114-134, New York, 1991.

[Born, Wolf, 1999] M. Born and E. Wolf, Principles of Optics. Cambridge University Press. Seventh Edition (1999).

[Burden, Fairies, 2000] R. L. Burden, J. Faires, "Numerical analysis", Brooks Cole (7th edition), 2000

[Cabral and Leith, 1993] B. Cabral, L. Leedon, “Imaging vector fields using line integral convolution, Computer Graphics Proceedings, Annual Conference Series 263-270, 1993.

[Cassarly, 2003] W. Cassarly, “Art of making efficient illuminator design fun”, Proceedings of SPIE Annual Meeting 2003, Editors: J.M. Sassian, P.K. Manhart and R. John Koshel. (to be published)

[Davies et al, 1994] N. Davies, M. McCormick, M. Brewin, “Design and analysis of an image transfer system using microlens arrays”, Opt. Eng. Vol. 33(11) 3624-3633, November 1994.

[De Bonet and Viola, 1998] J. S. De Bonet and P. Viola, “Texture Recognition Using a Non-parametric Multi-Scale Statistical Model”, Proceedings IEEE Conf. on Computer Vision and Pattern Recognition, 1998.

[De Bonet, 1997] J. de Bonet, “Multiresolution Sampling Procedure for Analysis and Synthesis of Texture Images", Computer Graphics, 361-368, 1997

[Donagarra, 2002] J. Dongarra, “The Sourcebook of Parallel Computing”, Morgan Kaufmann, 2002

[Ferweda at al., 1997] J. Ferweda, S. Pattanaik, P. Shirley, D. Greenberg, “A Model of Visual Masking for Computer Graphics”, Computer Graphics, 1997.

[Forbes, Alonso, 1998] G.W. Forbes and M.A. Alonso, “What on earth is a ray and how can we use them best?” Proceeding of the International Lens Design Conference, Hawaii, 22-31 (1998).

[Frazier, US Patent 5,727,236] James A. Frazier, “Wide angle, deep field, close focusing optical system”, US Patent 5,727,236, March 1998

[Gagalowicz and Ma, 1986] A. Gagalowicz and S. D. Ma, “Model driven synthesis of natural textures for 3-D scenes, Computers and Graphics, Vol. 10 161-170, 1986.

[Gardner, 1984] G. Gardner, “Simulation of Natural Scenes Using Texture Quadric Surfaces”, Computer Graphics Vol. 18, No.3 11-20, July 1984.

[Gaskill, 1978] J. Gaskill, “Linear Systems, Fourier Transforms and Optics”, John Willey & Sons, New York, 1978.

[Goodman, 2000] J. W. Goodman, "Introduction to Fourier optics", McGraw-Hill physical and quantum electronics series, New York, (3rd edition) 2000

[Goodman, Statistical Optics, 2000] J. W. Goodman, “Statistical Optics”, John Wiley & Sons, 2000

[Harvey, 2004], J. Harvey, “Applied Optics Laboratory” course notes, http://imaging.creol.ucf.edu/OSE5234/08Lab1-ParaxialOptics(Procedure).pdf, 2004.

[He at al, 1991] X. D. He, K. E. Torrance, F. X. Sillion and D. P. Greenberg, “A comprehensive physical model for light reflection”, Computer Graphics Vol. 18, No. 3 175-186, July 1991.

[Heeger, Bergen, 1995] D. Heeger, J. Bergen, “Pyramid-Based Texture Analysis/Synthesis”, Computer Graphics Proceedings, Annual Conference Series 229-233, 1995.

[Helmi, 2001] K. Helmi, “Playing with light”, Fiberarts Vol. 28, No.2 58-59, Sept./Oct. 2001.

[Hockney and Falco, 2000] D. Hockney and C. Falco (2000) Optical insights into Renaissance art. Optics and Photonics News, 11(7), 52-59.

[Hockney, 2001] D. Hockney, “Secret Knowledge: Rediscovering the lost techniques of the old masters”,

[Hoggard, 1997] L. Hoggard, “Light waves ahead”, Crafts, No. 147, 34-39, Jul./Aug. 1997.

[Hylen, 1997] Hylen, Steven H. L., “Image modifiers for use in photography”. US Patent 5,649,259, 1997.

[Kawazi and Ogura, 1980] M. Kawazi and Y. Ogura, “Application of gradient index fiber arrays to copying machines”, Applied Optics Vol. 19, No.7 1105-1112, April 1980

[Lewis, 1984] J. Lewis, “Texture Synthesis for Digital Painting”, Computer Graphics Vol. 18, No. 3, 245-251, July 1984.

[Lewis, 1984] T. Whitted, “Anti-Aliased Line Drawing Using Brush Extrusion”, Computer Graphics Vol. 17, No. 3 151-156, July 1983.

[Litwinowicz, 1997] P. Litwinowicz, “Processing images and video for an impressionist effect”, Computer Graphics Proceedings, Annual Conference Series 407-414, 1997.

[Liu et al, 1995] S. Liu, X. Zhang and H. Lai, “Artistic effect and application of moiré patterns in security holograms”, Applied Optics, Vol. 34, No. 22, 4700-4702, August 1995.

[Malacara, 1978] D. Malacara, “Optical Shop Testing”, John Miley and Sons, New York, 1978

[Malacara, 1994] D. Malacara and Z. Malacara, “Handbook of Lens Design”, Marcel Dekker Inc., New York, 1994

[Marechal, 1952] A. Marechal, Imagerie Geometrique: Aberrations. "Editions de la revue d’Optique Theorique et Instrumentale (1952).

[Martins, Shaoulov, Rolland, 2004] R. Martins, V. Shaoulov and J. Rolland, “Projection-based head-mounted displays for wearable computers”, Helmet- and head-mounted displays IX: Technologies and applications, SPIE Defense and Security Symposium 2004 (in press).

[Mir, 1983] J. Mir, “High resolution optical-addressing device and electronic scanner and/or printer apparatus employing such device”, US Patent 4,377,753, 22 March 1983.

[Miyata, 1990] K. Miyata, “A Method of Generating Stone Wall Patterns”, Computer Graphics Vol. 24, No. 4 387-394, August 1990.

[Montoya-Hernandez, et al., 1999] M. Montoya-Hernandez, M. Servin, D. Malacara-Hernandez, G. Paez, “Wavefront fitting using Gaussian functions”, Optics Communications 163, 1999

[Mouroulis and Macdonald, 1997] P. Mouroulis, J. Macdonald, “Geometrical Optics and Optical Design”, Oxford University Press, 1997

[Mouroulis, Macdonald, 1996] P. Mouroulis, P., and J. Macdonald, Geometrical Optics and Optical Design, Oxford Press, 1996

[Pharr et al, 1997] M. Pharr, C. Kolb, R. Gershbein, P. Hanrahan, “Rendering complex scenes with memory-coherent ray tracing”, Computer Graphics, 1997.

[Phong, 1975] B-T Phong, “Illumination for computer generated pictures”, Communications of the ACM 18, 6, 311-317, June 1975.

[Probst, 1999] C. Probst, “Seeing is believing”, American Cinematographer, February 1999

[Rolland and Strickland, 1997] J.P. Rolland , and R. Strickland, "An approach to the synthesis of biological tissue," Optics Express, 1(13), 414-423, 1997.

[Rolland, et.al., 1998] J. P. Rolland, A. Goon, and L. Yu, "Synthesis of textured complex backgrounds," Optical Engineering, 37(7), 2055-2063 (1998).

[Rolland, Hua and Shaoulov, 2002] Rolland, J.P., H. Hua, and V. Shaoulov, “Design of a compact relay lens” Technical Report TR02-05, University of Central Florida 2002. (Also in press).

[Rolland, Hylen, 1999] J.P. Rolland, and S. L. Hylen, "Painting cameras," Optics and Photonics News - Special Issue on Art and Science, 10(7), 33-35, (1999).

[Rolland, Shaoulov and Gonzales, 2001] J. Rolland, V. Shaoulov and J. Gonzales, "The Art of Back-of-the-Envelope Paraxial Raytracing", IEEE Transactions on Education, Vol. 44, No.4, 365-372, November 2001.

[Royden, 1968] H. L. Royden, Real Analysis, MacMillan Publishing Company, New York, 1968, page 269

[Shaoulov, Martins, Rolland, 2003] V. Shaoulov, R. Martins and J. Rolland, "Compact Microlenslet Arrays Imager", US patent pending, 2003.

[Shaoulov, Martins, Rolland, 2004] V. Shaoulov, R. Martins and J. Rolland, "Magnifying miniature displays with microlenslet arrays", Helmet- and head-mounted displays IX: Technologies and applications, SPIE Defense and Security Symposium 2004 (in press).

[Shaoulov, Rolland, 2001] V. Shaoulov, and J. Rolland, "Optical Phase Plates as a Creative Media for Special Effects in Images", Annual Meeting of the SPIE 2001, SPIE Proceedings Vol. 4442, pp. 112-118, Novel Optical Systems Design and Optimization IV, Eds. Jose M. Sasian, Paul K. Manhart, Dec. 2001.

[Shaoulov, Rolland, 2002] V. Shaoulov and J. Rolland, "Compact Relay Lenses Using Microlenslet Arrays", Proceedings of the SPIE: International Optical Design Conference 2002, Editors P.K. Manhart and J.M. Sasian, pp 74-79.

[Shaoulov, Rolland, 2003] V. Shaoulov and J. Rolland, "Design and Assessment of Microlenslet-Array Relay Optics", Applied Optics 42(34), December 2003.

[Shaoulov, Rolland, et. al., 2001] V. Shaoulov, C. Meyer, Y. Argotti, and J. Rolland, "Optical Phase Plates as a Creative Media for Special Effects in Images", Annual Meeting of

the SPIE 2001, SPIE Proceedings Vol. 4442, pp. 112-118, Novel Optical Systems Design and Optimization IV, Eds. Jose M. Sasian, Paul K. Manhart, Dec. 2001.

[Shaoulov, Rolland, et. al., 2004] V. Shaoulov, R. Satya, G. Schiavone, E. Clarkson and J. Rolland, "Model of Wide-angle Optical Field Propagation using Scalar Diffraction Theory", Special Issue of Optical Engineering on Illumination Engineering 43(7) pp. 1561-1567, July 2004.

[Slyusarev, 1984] G. Slyusarev, "Aberration and Optical Design Theory", Adam Hilger Ltd, Bristol, 1984.

[SmARTLens™, 2004] SmARTLens™, http://www.smartlens.com, 2004.

[Spector, 2000] D. Spector. Building Linux Cluster, O'Reilly, Sebastopol July 2000; http://www.beowulf-underground.org/

[Spencer and Murty, 1961] G. H. Spencer and M. V. R. K. Murty, "General ray-tracing procedure", JOSA Vol. 52, No.6 672-678, 1961.

[Toyama and Takami, 1982] M. Toyama and M. Takami, "Luminous intensity of a gradient-index lens array", Applied Optics Vol. 21 No.6 1013-1016, March 1982

[Toyama, Takami, 1982] M. Toyama and M. Takami, "Luminous intensity of a gradient-index lens array", Applied Optics 21(6) 1013-1016, (1982).

[Vincetti, et al,, 2000] L. Vincetti, A. Cucinotta, S. Selleri, M. Zoboli, "Three-dimensional finite-element beam propagation method: assessments and developments", JOSA A, 17[6], 2000.

[Volkel et al, 1996] R. Volkel, H.P. Herzig, P. Nussebaum, R. Dandliker, W. Hugle, "Microlens array imaging system for photolithography", Opt. Eng. 35(11) 3323-3330, November 1996.

[Westin, 1992] S. Westin, J. Arvo, K. Torrance, “Predicting reflectance functions from complex surfaces”, Computer Graphics, Vol. 26 255-264, June 1992.

[Wijk, 1991] J. Wijk, “Spot Noise: Texture Synthesis for Data Visualization”, Computer Graphics Vol. 25, No. 4 309-318, July 1991.

[Zobel, 2001] J. Zobel, “Symmetric anastigmatic endoscope relay system”, US Patent 6,490,085, 2001.

[Zone, 2001] R. Zone, “Through the looking glass”, American Cinematographer Vol. 82, No. 12 96-102, Dec. 2001.